

Influence of Active Antennas on EMF Restrictions in 5G Base Stations Deployment

Sofia Fazenda dos Santos Duarte Patrício

Thesis to obtain the Master of Science Degree in
Electrical and Computer Engineering

Supervisor: Prof. Luís Manuel de Jesus Sousa Correia

Examination Committee

Chairperson: Prof. José Eduardo Charters Ribeiro da Cunha Sanguino

Supervisor: Prof. Luís Manuel de Jesus Sousa Correia

Members of Committee: Prof. Custódio José de Oliveira Peixeiro

: Eng. Mónica Alexandra de Matos Gomes

November 2021

I declare that this document is an original work of my own authorship and that it fulfils
all the requirements of the Code of Conduct and Good Practices of the
Universidade de Lisboa.

To my loved ones

Acknowledgements

First and foremost, I would like to express my deepest gratitude to Professor Luís Correia for believing in my knowledge and willingness to work and learn, allowing me to develop this thesis under his supervision. I am extremely grateful for all the support, leadership, criticism and positivity that I have received from him throughout a year of constant learning.

To all the GROW members, Afonso Carvalho, Marco Failache, Maria Ferreira, and especially to Beatriz Ferreira, who has accompanied me throughout this year of work, exchanging points of view, challenges, and laughs when needed.

To Huawei, for allowing me to develop a thesis with such a relevant topic in collaboration with a company as remarkable in the area of telecommunications. My deepest gratitude to Eng. Mónica Gomes, for all the time, effort and willingness to help.

To my friends who have been with me throughout all these years, colouring my life and watching me grow up while giving me words of support and affection.

To my family, for always believing in me and pushing me to accomplish better. I wouldn't be as loved and fulfilled as I am today if it weren't for them. To my mother, who inspired me to be creative and cultured from a young age, and to my father, who unwittingly made me fall in love with engineering because of his manner of using knowledge to improve our daily lives. To my brother and sister, who have always been my best company and inspiration, and to my nephews, whom I hope to set a good example for. They all enrich my life with wisdom and love.

To my loved ones that have become stars in the sky, enlightening me during my long nights of work, I hope you are proud.

“Those who pass by us, do not go alone, and do not leave us alone; they leave a bit of themselves, and take a little of us.” - Antoine de Saint-Exupéry.

Abstract

This thesis aims to develop a model to analyse the influence of active antennas on electromagnetic field restrictions in 5G base stations deployment. The model allows for the computation of electromagnetic field exposure in the vicinity of base station antennas with 3.6 GHz in order to compute the respective exclusion zone that guarantees the safety of the population. The electric field is estimated as a function of distance for a Huawei antenna, using the CST Studio Suite simulation software. In order to avoid overestimated results, the active behaviour of the antennas is taken into account, considering realistic maximum power levels. Later, multi-band exposure is determined in order to define appropriate exclusion zones and analyse the impact of 5G installation on the increase of the existing exclusion zones, created by the legacy systems. This analysis allows for the evaluation of whether and under what conditions the increase in the exclusion zone requires the definition of physical barriers. Representative scenarios with co-location of antennas are analysed. First, the compliance distance considering only the exposure from the 3.6 GHz is determined, then, the exclusion zone distance before and after the installation of both 5G bands (700 MHz and 3.6 GHz) is computed. The highest increase in the exclusion zone distance is 170.4%, 78% and 104.1%, for urban, suburban and rural scenarios, respectively. The obtained results support that, in some scenarios, operators may need to reduce the total transmitted power in order to ensure the safety of the population.

Keywords

Electromagnetic Field, 5G, Exclusion Zone, Averaging Time, Near-field.

Resumo

Esta tese tem como principal objetivo o desenvolvimento de um modelo para analisar a influência das antenas ativas nas restrições de exposição a campos eletromagnéticos para implementação de estações base de 5G. O modelo permite a determinação da exposição aos campos eletromagnéticos nas proximidades de estações base com 3.6 GHz instalado, de forma a determinar a respetiva zona de exclusão que garante a segurança da população. O campo elétrico é estimado em função da distância para uma antena da Huawei, usando como ferramenta o programa de simulação CST Studio Suite. De forma a evitar a sobrestimação dos resultados, é tido em consideração o comportamento ativo das antenas, considerando valores realistas de potência máxima transmitida. Posteriormente, é estudada a exposição multi-banda de forma a definir zonas de exclusão adequadas e analisar o impacto da instalação no aumento das zonas de exclusão existentes, criadas pelos sistemas anteriormente presentes na estação base. Este estudo permite determinar se, e em que circunstâncias, o aumento da zona de exclusão requer a definição de barreiras físicas. Cenários representativos de estações base com co-localização de antenas são analisados. Primeiramente, é determinada a distância de conformidade tendo apenas em conta a exposição com 3.6 GHz, calculando de seguida a distância de zona de exclusão antes e depois da instalação de ambas as bandas de 5G (700 MHz e 3.6 GHz). O maior aumento na distância de zona de exclusão é de 170.4%, 78% e 104.1%, para cenários urbanos, suburbanos e rurais, respetivamente. Os resultados obtidos suportam que, para alguns cenários, os operadores poderão ter necessidade de reduzir a potência total transmitida de forma a garantir a segurança do público.

Palavras-chave

Campo Eletromagnético, 5G, Zona de Exclusão, Tempo Médio, Campo Próximo.

Table of Contents

Acknowledgements	vii
Abstract.....	ix
Resumo	x
Table of Contents.....	xi
List of Figures	xiii
List of Tables.....	xvi
List of Abbreviations.....	xviii
List of Symbols.....	xxii
List of Software	xxvii
1 Introduction	1
1.1 Overview and Motivation	2
1.2 Contents	4
2 Fundamental Concepts and State of the Art.....	7
2.1 Radio Interface	8
2.2 Base Station Deployments	12
2.3 Antennas in 5G.....	14
2.3.1 Arrays and Beamforming.....	15
2.3.2 Radiating Field Regions	18
2.4 Services and Applications.....	19
2.5 EMF Radiation Exposure.....	21
2.5.1 EMF Radiation	21
2.5.2 Exclusion Zones	23
2.6 State of the Art.....	26
3 Model Development and Simulator Description	29
3.1 Model Overview.....	30

3.2	Temporal Variation Contribution	31
3.2.1	Temporal Variation	31
3.2.2	Temporal Variation of the Reference Level	35
3.2.3	Beamforming Behaviour	36
3.3	CST Simulation Software	39
3.3.1	Software Features and Operation	39
3.3.2	Antenna Unit Simulation	41
3.3.3	Antenna Full Array Simulation	44
3.3.4	Near-field Results	49
3.4	Exclusion Zone Evaluation Model.....	54
3.5	Model Assessment	57
4	Results Analysis	61
4.1	Scenarios Description.....	62
4.2	Exclusion Zone for Broadside Beam Direction	66
4.3	Exclusion Zone for Other Directions	75
5	Conclusions.....	77
Annexe A.	Antennas Description	83
Annexe B.	Measurements Description and BS Characteristics	86
B.1	Measurements Description	87
B.1.1	General Description	87
B.1.2	BS1	87
B.1.3	BS2	91
Annexe C.	Multi-band Exposure Computation	96
References.....		99

List of Figures

Figure 2.1.	Representation of the dependency between the number of slots and numerology (extracted from [Camp17]).	12
Figure 2.2.	Multi-user beamforming accurate coverage (extracted from [HUAW19a]).	15
Figure 2.3.	Radiating field regions (adapted from [Bala16]).	18
Figure 2.4.	Typical changes of antenna amplitude pattern shape from reactive near-field toward the far-field (extracted from [Bala16]).	19
Figure 2.5.	Key capabilities in different application scenarios (extracted from [HUAW19a]).	20
Figure 2.6.	Reference levels for E , H and S , for time-averaged general public exposures higher than 6 min from 100 kHz to 300 GHz (unperturbed RMS values) (extracted from [INCI20]).	23
Figure 2.7.	The validity range of several surveyed propagation models (extracted from [OFRC05]).	25
Figure 2.8.	Representation of an antenna exclusion zone (extracted from [OFRC05]).	25
Figure 3.1.	Model configuration (based on [Mour20]).	30
Figure 3.2.	Incident Power Density, S_{inc} , reference level for exposure, integrated over time intervals between 0.5 min and 6 min, from 2 GHz to 6 GHz (unperturbed RMS values).	35
Figure 3.3.	Representation of a planar array with crossed-dipole elements.	36
Figure 3.4.	Half-wavelength dipole with a rotation angle equal to 0° and 45° (extracted from [ZhTC15]).	38
Figure 3.5.	AAUxxxxw radiation patterns in a macro coverage scenario (adapted from [HUAW21b]).	38
Figure 3.6.	Representation of a FDTD cell (adapted from [Laak15]).	40
Figure 3.7.	Representation of a half-wavelength dipole antenna and its dimensions.	42
Figure 3.8.	Design of the slanted half-wavelength dipole antenna in CST, placed in the xOy plane.	43
Figure 3.9.	Mesh representation of the 45° slanted half-wavelength dipole antenna, in xOy plane.	43
Figure 3.10.	S_{11} parameter, as a function of frequency, of the half-wavelength dipole.	44
Figure 3.11.	3D E-pattern pattern of the 45° slanted dipole operating at 3.6 GHz.	44
Figure 3.12.	2D far-field cut ($\phi = 0^\circ$) of the E- and gain patterns for the 45° slanted dipole.	44
Figure 3.13.	2D far-field cut ($\theta = 90^\circ$) of the E- and gain patterns for the 45° slanted dipole.	45
Figure 3.14.	2D far-field cut ($\phi = 0^\circ$) of the E- and gain patterns for the -45° slanted dipole.	45
Figure 3.15.	2D far-field cut ($\theta = 90^\circ$) of the E- and gain patterns for the 45° slanted dipole.	45
Figure 3.16.	Design of the 8×12 planar array in CST, placed in the xOy plane.	46
Figure 3.17.	3D 8×12 planar array E-pattern with ($\theta = 0^\circ$, $\phi = 0^\circ$).	47
Figure 3.18.	2D far-field cut ($\phi = 0^\circ$) of the E- and gain patterns for the 8×12 planar array.	47
Figure 3.19.	2D far-field cut ($\theta = 90^\circ$) of the E- and gain patterns for the 8×12 planar array.	47

Figure 3.20.	3D 8×12 planar array E-pattern with ($\theta = 45^\circ$, $\phi = 45^\circ$).	48
Figure 3.21.	2D far-field cut ($\phi = 45^\circ$) of the E- and gain patterns for the 8×12 planar array.	49
Figure 3.22.	2D far-field cut ($\theta = 45^\circ$) of the E- and gain patterns for the 8×12 planar array.	49
Figure 3.23.	CST design using Evaluate Field on Curve tool.	50
Figure 3.24.	Dipole electric field strength as a function of distance.	50
Figure 3.25.	Dipole electric field strength decay with distance, near the far-field region.	51
Figure 3.26.	AAUxxxxw electric field strength decay with distance in the radiating near-field region.	51
Figure 3.27.	AAUxxxxw electric field strength decay with distance in the radiating near-field region.	52
Figure 3.28.	AAUxxxxw electric field strength decay with distance in the far-field region.	52
Figure 3.29.	AAUxxxxw electric field strength decay with distance for the radiating near- and far-field regions using linear scale.	53
Figure 3.30.	AAUxxxxw electric field strength decay with distance for the radiating near- and far-field regions using logarithmic scale.	54
Figure 3.31.	Computation of D_{Front} with the exclusion zone evaluation model for multi-band exposure (based on [Mour20]).	57
Figure 3.32.	$E(\theta, \phi, d)$ as a function of distance varying the antenna input power.	58
Figure 3.33.	D_{front} as a function of antenna's input power with $GM = 25$ dBi, $S_{ref} = 40$ and $Tvar = 0.25$	58
Figure 3.34.	$E(\theta, \phi, d)$ as a function of distance varying the antenna gain.	59
Figure 3.35.	D_{front} as a function of the antenna gain with $P_{in} = 240$ W, $S_{ref} = 40$ and $Tvar = 0.25$	59
Figure 3.36.	D_{front} as a function of the power density reference level established by ICNIRP with $P_{in} = 240$ W, $GM = 25$ dBi and $Tvar = 0.25$	60
Figure 4.1.	D_{front} for the carrier configuration 1/1 taking 100% of the maximum transmit power/beam.	67
Figure 4.2.	D_{front} for the carrier configuration 1/1 taking the actual transmit power/beam.	67
Figure 4.3.	D_{front} for the carrier configuration 2/1 taking 100% of the maximum transmit power/beam.	68
Figure 4.4.	D_{front} for the carrier configuration 2/1 taking the actual transmit power/beam.	68
Figure 4.5.	D_{front} for the carrier configuration 4/2 taking 100% of the maximum transmit power/beam.	69
Figure 4.6.	D_{front} for the carrier configuration 4/2 taking the actual transmit power/beam.	69
Figure 4.7.	D_{front} for the carrier configuration 4/4 taking 100% of the maximum transmit power/beam.	70
Figure 4.8.	D_{front} for the carrier configuration 4/4 taking the actual transmit power/beam.	70
Figure 4.9.	Downtilt influence on the exclusion region (adapted from [Antu12]).	73
Figure B.1.	View to sector 2 of the BS1.	88
Figure B.2.	Vertical plane sketch of sector 2 of the BS1.	88
Figure B.3.	Horizontal plane sketch of sector 2 of the BS1.	89
Figure B.4.	Measurement results of sector 2 of the BS1.	90
Figure B.5.	View of the terrace were BS1 is installed.	90
Figure B.6.	View of the terrace were BS1 is installed.	91
Figure B.7.	View of the terrace were BS1 is installed.	91

Figure B.8. View to sector 3 of the BS2.....92
Figure B.9. Vertical plane sketch of sector 3 of the BS2.....92
Figure B.10. Horizontal plane sketch of sector 3 of the BS2.....93
Figure B.11. Measurement results of sector 3 of the BS2 with no traffic induced.....94
Figure B.12. Measurement results of sector 3 of the BS2 with traffic induced.....94
Figure B.13. View of the terrace where BS2 is installed.....95

List of Tables

Table 2.1.	GSM assigned bands in Portugal (based on [ANAC20]).....	8
Table 2.2.	GSM BS maximum output power (adapted from [Corr20]).....	8
Table 2.3.	UMTS assigned bands in Portugal (based on [ANAC20]).....	9
Table 2.4.	UMTS BS maximum output power (extracted from [Corr20]).....	9
Table 2.5.	LTE assigned bands in Portugal (based on [ANAC20]).	9
Table 2.6.	Relationship between bandwidths, number of subcarriers and number of available Resource Blocks (adapted from [Corr20]).....	10
Table 2.7.	LTE BS maximum output power (extracted from [Corr20]).	11
Table 2.8.	NR assigned bands in Portugal (based on [Corr20]).....	11
Table 2.9.	Numerologies and respective SCSs (based on [Corr20]).....	12
Table 2.10.	Output power, cell radius, users and location of different types of cells (based on [Corr20]).....	13
Table 2.11.	Classification of BS antennas installation according to the range (extracted from [Antu12]).	13
Table 2.12.	Reference levels for local exposure, averaged over 6 min, to EMFs from 400 kHz to 6 GHz (unperturbed RMS values) (based on [ICNI20]).....	22
Table 2.13.	Reference levels for exposure, averaged over 30 min and the whole body, to electromagnetic fields from 400 kHz to 300 GHz (unperturbed RMS values) (based on [ICNI20]).....	23
Table 2.14.	Reference levels for local exposure, integrated over intervals between 0.5 min and 6 min, to EMFs from 400 kHz to 6 GHz (unperturbed RMS values) (based on [ICNI20]).....	23
Table 3.1.	IMT-2020 Technical Performance Requirements for DL in the context of a dense urban eMBB scenario (based on [ITUR17]).	34
Table 3.2.	Access times and average session durations for different downloads and services.....	34
Table 3.3.	Dimensions of the half-wavelength dipole antenna.....	42
Table 3.4.	Empirical tests to validate the exclusion zone evaluation model (based on [Mour20]).....	58
Table 4.1.	Percentage of maximum transmit power/beam for different scenarios and system usages.....	63
Table 4.2.	Power density reference levels, averaged over 1 min, 6 min and 30 min.....	64
Table 4.3.	Active mobile communications systems in each scenario (based on [Mour20]).	65
Table 4.4.	Output power per carrier/MIMO element and antenna gain for the considered systems.....	65
Table 4.5.	Number of MIMO elements for each band of LTE and NR.....	65
Table 4.6.	D_{front} for Urban, Suburban and Rural scenarios with only 3.6 GHz active. ...	66
Table 4.7.	D_{front} variation due to NR installation for each scenario and carrier configuration.....	71
Table 4.8.	NR contribution to D_{front} for each scenario and carrier configuration.....	71
Table 4.9.	Downtilt influence on the definition of physical barriers for the Urban 1 scenario.	74
Table 4.10.	Downtilt influence on the definition of physical barriers for the Urban 2 scenario.	

	74
Table 4.11.	Downtilt influence on the definition of physical barriers for the Urban 3 scenario.	74
Table 4.12.	Analysed directions for the back, side, top and bottom borders of the exclusion zone.	75
Table 4.13.	Normalised gains for the analysed directions for NR3600.	75
Table 4.14.	D_{back} , D_{side} , D_{top} and D_{bottom} results for Urban, Suburban and Rural scenarios with only NR3600 active.	76
Table A.1.	AAUxxxxw technical specifications (based on [HUAW21b]).....	84
Table A.2.	AAUxxxxw and AAUxxx3 technical comparison (based on [HUAW21b] and [HUAW19b]).....	84
Table A.3.	Technical characteristics of the passive antenna (extracted from [HUAW19d])..	85
Table B.1.	Characteristics of the BSs where the measurements were conducted.....	87
Table B.2.	Measurement results of sector 2 of the BS1.....	89
Table B.3.	Measurement results of sector 3 of the BS2.....	93
Table C.1.	S_{nf}^{norm} coefficients and far-field distances for the different systems considering the passive antennas with 8 elements (extracted from [Mour20]).....	98

List of Abbreviations

2D	Two-dimensional
2G	2 nd Generation
3D	Three-dimensional
3G	3 rd Generation
3GPP	3 rd Generation Partnership Project
4G	4 th Generation
5G	5 th Generation
6G	6 th Generation
AA	Active Antenna
AIOps	Artificial Intelligence for IT Operations
ANACOM	<i>Autoridade Nacional de Comunicações</i>
AR	Augmented Reality
BS	Base Station
CP	Cyclic Prefix
DCPSK	Differential Coherent Phase Shift Keying
DL	Downlink
DoA	Direction of Arrival
EIRP	Effective Isotropic Radiated Power
E-pattern	Electric Field Pattern
eMBB	Enhanced Mobile Broadband
EMF	Electromagnetic Field
FDTD	Finite Difference Time Domain
ETSI	European Telecommunications Standards Institute
EU	European Union
FDD	Frequency Division Duplex

FDMA	Frequency Division Multiple Access
FEM	Finite Element Method
FIT	Finite Integration Technique
GBR	Guaranteed Bit Rate
GPS	Global Positioning System
GMSK	Gaussian Minimum Shift Keying
GSM	Global System for Mobile Communications
HPBW	Half Power Beam Width
HSDPA	High-Speed Download Packet Access
HSPA+	Evolved High-Speed Packet Access
HSUPA	High-Speed Upload Packet Access
ICNIRP	International Commission on Non-Ionising Radiation Protection
IEEE	Electrical and Electronics Engineers
IoE	Internet of Everything
IoT	Internet of Things
ISI	Inter-Symbol Interference
ITU-R	International Telecommunication Union Radiocommunication Sector
LBS	Location-based Service
LOS	Line-of-Sight
LTE	Long Term Evolution
LTE-A	Long Term Evolution Advanced
MIMO	Multiple Input Multiple Output
MMS	Multimedia Message Service
MU	Multi-User
M2M	Machine to Machine
mMIMO	Massive MIMO
mMTC	Massive Machine Type Communication
MU	Multi-user
NA	Not Applicable
NLOS	Non-Line-of-Sight

NR	New Radio
NSA	Non-Standalone Access
nGBR	Non-Guaranteed Bit Rate
OFDMA	Orthogonal Frequency Division Multiple Access
PAPR	Peak to Average Power Ratio
PEC	Perfect Electric Conductor
PMC	Perfect Magnetic Conductor
PML	Perfectly Matched Layer
QAM	Quadrature Amplitude Modulation
QCI	Quality Channel Indicator
QoS	Quality of Service
QPSK	Quadrature Phase Shift Keying
RF	Radio Frequency
RB	Resource Block
RSRP	Reference Signal Received Power
RMS	Root Mean Square
SA	Standalone Access
SAR	Specific Absorption Rate
SC-FDMA	Single-Carrier Frequency Division Multiple Access
SCENIHR	Scientific Committee on Emerging and Newly Identified Health Risks
SCS	Subcarrier Spacing
SINR	Signal-to-Interference-plus-Noise Ratio
SMS	Short Message Service
SNR	Signal-to-Noise Ratio
SR	Scan Range
SRS	Sounding Reference Signal
TDD	Time Division Duplex
TDMA	Time Division Multiple Access
TLM	Transmission-Line Matrix
TRP	Transmission/Reception Point

TTI	Transmission Time Interval
UDS	User Distribution Scenarios
UHDV	Ultra High Definition Video
UL	Uplink
UMTS	Universal Mobile Telecommunications System
uRLLC	Ultra-Reliable Low Latency Communication
VoIP	Voice over Internet Protocol
VR	Virtual Reality
WCDMA	Wideband Code Division Multiple Access
WHO	World Health Organisation
W NR	With New Radio
W/O NR	Without New Radio

List of Symbols

α	Ratio between the electric field limit and the maximum voltage multiplied by normalised three-dimensional antenna radiation pattern
α_V	Vertical scan range
β	Phase difference between any two successive antenna elements forming the array
β_x	Phase excitation for an element in the x -axis
β_y	Phase excitation for an element in the y -axis
$\beta_{x,y}$	Phase excitation for any element located in the planar array
Δ_d	Sampling interval
Δ_{ele}	Element spacing factor
Δ_{excl}	Exclusion zone variation
Δf_{subc}	Subcarrier spacing
Δh	Height variation
η_{NR}	Contribution of NR to the exclusion zone distance
θ	Elevation angle
θ_B	3 dB beamwidth
θ_d	Elevation angle corresponding to the desired direction for the beam focus
θ_{dt}	Downtilt angle
λ	Wavelength of the transmitted electromagnetic wave
μ	Numerology
τ_{SF}	Subframe duration
ϕ	Azimuth angle
ϕ_d	Elevation angle corresponding to the desired direction for the beam focus
ϕ_{total}	Total inclination of the maximum antenna gain
ψ	Total phase difference between the signals from the antenna elements when they reach the observation point in the far-field
A_{cell}	Cell coverage area
a	Radius of the wire antenna
a_i	Fit coefficients for the passive antennas ($i = 0,1,2,3$)
a_{pd}	Average power decay

C	Propagation constant
C_i	Fit coefficient ($i = 0,1,2$)
D	Largest dimension of the antenna
D_{back}	Back border of the exclusion zone
D_{bottom}	Bottom border of the exclusion zone
$D_{excl}^{W NR}$	Exclusion zone distance with NR
$D_{excl}^{W/O NR}$	Exclusion zone distance without NR
D_{front}	Front border of the exclusion zone
D'_{front}	Front border of the exclusion zone when a downtilt is applied
D_{side}	Side border of the exclusion zone
D_{top}	Top border of the exclusion zone
d_{ele}	Distance between the antenna elements of the array
d_{ele}^H	Horizontal distance between the antenna elements of the array
d_{ele}^V	Distance between the antenna elements of the vertical array
d_l	Compliance distance
d_{max}	Maximum limit for the definition of the sampling interval
d_{min}	Minimum limit for the definition of the sampling interval
d_x	Location of the feeds at each element in respect to the x -axis, referenced to the initial element in the lower left corner of the array
d_y	Location of the feeds at each element in respect to the y -axis, referenced to the initial element in the lower left corner of the array
E	Electric field
E_{aa}	Electric field radiated by an array
E_{ele}	Electric field radiated by a single element
E_{inc}	Incident electric field strength
E_{ind}	Induced electric field
E_{lim}	Electric field limit
F_{aa}	Antenna array factor
F_{aax}	Antenna array factor of an array placed in the x -axis
F_{aay}	Antenna array factor of an array placed in the y -axis
F_{aa}^{norm}	Normalised antenna array factor
F_{ress}	Resonance factor
F_{TDD}	DL Duty Cycle
f	Frequency
f_{θ}	Normalised antenna radiation pattern in the vertical plane
f_{ϕ}	Normalised antenna radiation pattern in the horizontal plane
$f_{\theta\phi}$	Normalised three-dimensional antenna radiation pattern
f_c	Central frequency
f_d	Function representing the electric field dependency with distance

$f_{ele,H}$	Element radiation pattern in the horizontal plane
$f_{ele,V}$	Element radiation pattern in the vertical plane
G	Gain of the antenna
\bar{G}	Time-averaged gain
G_{ele}	Gain of each element
G_M	Maximum gain of the antenna
G_{mMIMO}^{beam}	Individual mMIMO beam gain
$G_r total$	Total antenna receiver gain
g	Dipole feed gap
H	Magnetic field
H_{inc}	Incident magnetic field strength
h_{ant}	Height of the antenna planar array
h_{ele}	Height of the antenna array element
$h_{min,ant}$	Minimum required antenna height
h_{person}	Average height of a person
I_m	Maximum current
k	Wavenumber
L_{ref}	Reference path loss
L^{opt}	Optimised dipole length
L	Total length of the wire antenna
l	Half of the length of the wire antenna
l_{res}	Resonance length
M	Number of array rows
M^n	Modulation order
m^{th}	Planar array row number
N	Number of array columns
N_{array}	Number of antenna elements in the considered array
N_{bands}	Number of active bands
N_{beams}	Number of beams that can actually be generated and fitted into a sphere
N_c	Number of carriers
N_c_{GSM900}	Number of carriers for GSM
N_c_{UMTS}	Number of carriers for UMTS
N_{ele}	Number of antenna elements
$N_{ele,H}$	Number of horizontal elements of the planar array
$N_{ele,V}$	Number of vertical elements of the planar array
N_{bands}	Number of active bands
N_{RB}	Number of RBs
N_{RB}^{alloc}	Number of allocated RBs

$N_{RB}^{alloc,DL}$	Number of RBs scheduled for DL transmission
N_{RB}^{DL}	Total number of RBs available for DL
N_{RB}^{max}	Maximum number of RBs allocated to a user
N_{RB}^{min}	Minimum number of RBs allocated to a user
N_{RB}^{user}	Number of RBs allocated to each user
N_{samp}	Number of samples
N_{SC}^{RB}	Number of subcarriers per resource block
N_{slot}^{frame}	Number of slots per frame
$N_{slot}^{subframe}$	Number of slots per subframe
$N_{streams}$	Order of MIMO configuration
N_{subc}	Number of subcarriers
N_{symb}^{slot}	Number of symbols per slot
N_{symb}^{SF}	Number of symbols per subframe
N_{sys}	Number of systems
N_{users}	Total number of users
N_{users}^{beam}	Maximum number of users per beam
N_{users}^T	Number of served independent users
N_{users}^{sim}	Number of simultaneous users served by the system at a specific time instant
n^{th}	Planar array column number
\bar{P}	Time-averaged transmit power
\bar{P}_{beam}	Actual time-averaged transmit power per beam
P_{EIRP}	Effective Isotropic Radiated Power
\bar{P}_{EIRP}	Time-average EIRP
P_{ele}	Antenna element power
P_{in}	Antenna input power
$P_{r min}$	Minimum power available at the receiving antenna
R_b^{user}	Throughput for each user
R_{cell}	Cell coverage radius
R_{ff}	Far-field region boundary
R_{rnf}	Reactive near-field region boundary
$r_{mn,obs}$	Distance between the element placed in the m^{th} row and n^{th} column of the planar array and the observation point
r_{obs}	Distance between the antenna and the observation point
S	Power density
$S_{final,i}$	Power density function for the i^{th} communication system
S_{inc}	Incident power density
S_{lim}	Power density limit
S_{nf}^{norm}	Power density for the near-field of the passive antennas

	normalised to the input power and antenna gain
S_{nomr}^{tot}	Total normalised power density
$S_{pass_antennas}$	Power density of the passive antennas
S_{ref}	Power density reference level established by ICNIRP
$S_{ref,i}$	Power density ICNIRP reference level at frequency i
T	Averaging time
$T_{DL,transm}$	DL transmission time
T_s	Total average scheduling time per user
$T_{UL,transm}$	UL transmission time
T_{var}	Temporal variation contribution
t	Time interval
U_{inc}	Incident power density
V_M	Maximum voltage
w_{ant}	Height of the antenna planar array
x_{max}	Maximum position in x -axis
x_{min}	Minimum position in x -axis
y_{obs}	y coordinate of the observation point
y_{mn}	y coordinates of the element placed in the m^{th} row and n^{th} column
y_{max}	Maximum position in y -axis
y_{min}	Minimum position in y -axis
Z_0	Free-space impedance
z_{mn}	z coordinates of the element placed in the m^{th} row and n^{th} column
z_{max}	Maximum position in z -axis
z_{min}	Minimum position in z -axis
z_{obs}	z coordinate of the observation point

List of Software

CST Studio Suite

Genex Probe 5

Matlab R2020a

Microsoft Excel 2016

Microsoft PowerPoint 2016

Microsoft Word 2016

Electromagnetic field simulation software

Air interface test software

Numerical computing software

Spreadsheet software

Presentation and slide software

Text editor software

Chapter 1

Introduction

This chapter provides a synopsis of the work. A discussion of the historical evolution of mobile communications is addressed, along with the main principles of the currently used communication systems. The motivation is presented with a brief description of the problem under study. At the end of this chapter, the work structure is described.

1.1 Overview and Motivation

The evolution of cellular communication networks has been happening since the early 1980s. Almost every ten years, a new generation of mobile communication networks appears, each one of them being more powerful than the previous one, presenting new features, techniques and capabilities. Technology is developed not only to serve present needs but also to improve the future. Therefore, after the 4th generation (4G), the industry started developing the 5th generation (5G) and will continue working on new generations, such as the 6th generation (6G), that will serve the needs of a future world.

The 2nd generation (2G), launched in the early 1990s, introduced the first digital systems. This generation includes the Global System for Mobile Communications (GSM), a standard developed by the European Telecommunications Standards Institute (ETSI). Services such as Short Message Service (SMS) and Multimedia Message Service (MMS) were then possible, with maximum throughput for voice equal to 22.8 kbps and 9.6 kbps for data [Corr20]. Travel with roaming services emerged.

The 3rd generation (3G) arrived in the early 2000s, leading to the widespread use of the internet on mobile phones. Smartphones were introduced, allowing users to access data from any location in the world. Developed by the 3rd Generation Partnership Project (3GPP), the Universal Mobile Telecommunications System (UMTS) is a mobile cellular system based on GSM in terms of network. With High-Speed Download Packet Access (HSDPA) and High-Speed Upload Packet Access (HSUPA), quicker internet speeds were achieved, with the maximum Uplink (UL) and Downlink (DL) speeds being 384 kbps and 14.4 Mbps for HSDPA and 5.8 kbps and 14.4 Mbps for HSUPA. A further improved 3GPP standard, Evolved High-Speed Packet Access (HSPA+), appeared, allowing bitrates to reach as high as 11.5 Mbps for UL and 28 Mbps for DL [Corr20].

Although 3GPP's purpose was to develop specifications for 3G, nowadays, it provides specifications for all telecommunications network technologies, including 4G. Long Term Evolution (LTE) was first introduced in 2010, presenting a theoretical maximum DL speed of 300 Mbps and a latency of 50 ms. The minimum speeds set by the International Telecommunication Union Radiocommunication Sector (ITU-R) were practically unreachable. LTE Advanced (LTE-A) followed LTE, getting a step closer to proper 4G. LTE-A offers higher speeds with a theoretical maximum DL speed of more than 1 Gbps, thus increasing spectral efficiency and the number of simultaneously active users, with better performance at the cell edge. LTE-A Pro followed, employing partially evolved versions of previously used technologies to increase bandwidth and data speeds by up to three times while reducing latency from 10 ms to 2 ms [Corr20].

5G, also known as New Radio (NR), constitutes the newest step in telecommunications. With 5G, broadband wireless services are taken to another level, ceasing to stick only to the mobile internet and starting to move towards the Internet of Things (IoT) and more critical communication scenarios. This generation allows for massive connectivity among people, among machines and between each other. Remote and smart health care, Augmented Reality (AR), Virtual Reality (VR), Ultra High Definition Video (UHDV), self-driving, connected vehicles, home broadband, factory automation, smart grid, smart pot, smart city and many other services can now be a reality due to 5G [HUAW19a].

With larger bandwidth, 5G can use higher frequencies (millimetre waves range), offering a maximum speed of 10 Gbps, about 10 to 100 times faster than 4G. With such a high-band spectrum, it is possible to increase the speed and decrease latency, achieving a low value of 1 ms. When compared to 4G, capacity has increased up to 100 times the number of connected devices per unit area, with 99.999% availability and improved coverage, and a 90% reduction in network energy usage [Thal20].

Despite all these achievements, the arrival of 5G brought some concerns about the exposure to Radiofrequency (RF) Electromagnetic Fields (EMFs) since it may cause adverse health effects on people.

The high data rates required by 5G imply higher signal power at the receiver, raising concerns about the amount of radiation of EMFs applied to the user. With 5G, Base Stations (BSs) will operate with more transmitters and narrower beams. Smaller cellular networks will be used to provide service for smaller areas. Thus, with the antennas being located closer to users, the chances of human exposure to radiation from EMFs may increase.

5G will use in the future spectrum that has never been used before for cellular wireless communications, i.e., besides the licenced spectrum below 6 GHz, it is foreseen to use spectrum above 6 GHz (mm-waves range). However, sub-6GHz is the candidate for early deployment networks, so for the following years, the application of 5G will be predominantly for frequencies in the bands of 700 MHz and 3.6 GHz, which are the bands taken for this thesis. While the 700 MHz band facilitates the transition to 5G and coverage in different areas, the 3.6 GHz band is responsible for providing the necessary capacity for services supported on 5G systems. 5G is located in a frequency band of the non-ionising spectrum for which several scientific pieces of evidence have already shown that this kind of radiation does not cause internal damage to human cells.

Up to today, the literature only contains very few studies defending that EMFs have a significant impact on human health. However, people remain concerned. Some even believe that 5G degrades the immune system, therefore helping the spread of COVID-19. This theory that the immune system is severely affected by EMFs is the same claimed when 2G, 3G and 4G arrived because this concern has been around for many years now, since World War II with the military radar systems. The truth is that many countries currently have no 5G infrastructure despite having a large number of confirmed cases. Scientists have confirmed that COVID-19 transmission happens via respiratory droplets, which cannot be transmitted through 5G electromagnetic waves [Euro20a], [Euro20b].

In order to ensure the safety of citizens, there are entities in charge of establishing guidelines for limiting exposure to EMFs, such as the International Commission on Non-Ionising Radiation Protection (ICNIRP).

Due to the deployment density of 5G networks and a notable reduction in the distance between the users and the antennas, the usual estimation of EMF radiation distribution in the far-field zone, only based on radiation pattern, will not be enough. The current methodology for determining the received EMF exposure assumes that the transmitting antennas have predictable radiation patterns and that the BS is transmitting signals at its theoretical maximum power. However, these assumptions should not be

made when using Massive Multiple Input Multiple Output (mMIMO) and beamforming, making the existing measuring methods of EMFs not suitable for NR antennas. Therefore, there is a need to develop a model that allows for the computation of EMF exposure in the vicinity of NR BS antennas, i.e., within the near-field region.

1.2 Contents

This thesis was developed in collaboration with Huawei with the aim to analyse the influence of Active Antennas (AAs) on EMF restrictions in 5G BSs deployment.

The main goal of this work is to develop a model to determine EMF exposure in the vicinity of BS antennas with 3.6 GHz NR installed in order to compute the respective exclusion zone that guarantees general public safety. The development of the model takes the active behaviour of the 3.6 GHz NR antennas into account by considering realistic maximum power levels, leading to less overestimated results. The obtained results are followed by an analysis of the impact of NR installation on the increase in the existing exclusion zones, allowing to determine in which circumstances that increase will require the definition of physical barriers.

This thesis is composed of 5 chapters, including the present one, along with some annexes containing additional information and complementary results.

Chapter 2 presents the fundamental concepts of mobile communication systems essential to the proper development of this thesis, such as the radio interface, BS deployments, the new 5G antennas, radiating field regions and 5G services and applications. The EMF radiation exposure around a BS is addressed, as are the respective international safety established guidelines. The definition of an exclusion zone and its importance is presented. Finally, the main performance parameters for the model implementation are described, followed by a state of the art containing the most relevant published works related to the topic under study.

Chapter 3 addresses the methodologies for the development of the model, along with some expected results. An overview of the general model is presented, containing its main goals, input and output parameters. The temporal variation of EMF exposure is studied and analysed in order to determine its effects on the results, as well as the beamforming behaviour of the NR antennas. The design and simulation of the antenna under study is addressed, using the CST Studio Suite software, followed by an analysis of the respective near-field results. A model to estimate the exclusion zone is developed and presented along with a set of empirical tests to make its assessment. Finally, a comparison with experimental results extracted to contribute to the assessment of the model is provided.

In Chapter 4, an analysis of the results obtained from the model is presented. Firstly, the scenarios under study are described. Then, for each scenario, an analysis is made on the exclusion zone values for the front, side, back, top, and bottom dimensions. An analysis of the impact of the exclusion zone dimensions on the definition of physical barriers for public protection is also presented.

Finally, in Chapter 5, the main conclusions of the thesis are summarised along with some suggestions for future work.

At the end of the thesis, a set of annexes is provided. Annexe A presents the main technical characteristics of the different antennas used in this thesis. Annexe B contains the layout and specifications of the different BSs where the measurements were performed. Lastly, Annexe C presents the equations and parameters considered for the computation of multi-band exposure.

Chapter 2

Fundamental Concepts and State of the Art

This chapter provides an overview of GSM, UMTS, LTE and NR systems, mainly focussing on the radio interfaces, description of BS deployments, active antennas, services and applications, and EMFs radiation exposure in 5G networks. The main performance parameters necessary for the development of the model, as well as the state of the art, are presented at the end of the chapter.

2.1 Radio Interface

This sub-section consists of the radio interface of GSM, UMTS, LTE and NR technologies, analysing the used frequency bands, multiple access techniques, duplexing modes and BS maximum output powers.

The transmission of bidirectional information in duplex systems can be accomplished by using Frequency Division Duplex (FDD), which is the duplexing mode used in GSM. The assigned bands for GSM in Portugal are presented in Table 2.1.

Table 2.1. GSM assigned bands in Portugal (based on [ANAC20]).

Band [MHz]	Uplink [MHz]	Downlink [MHz]	Total Bandwidth [MHz]
900	890-915	935-960	50
1800	1710-1785	1805-1880	150

As a multiple access technique, GSM uses a combination of Frequency Division Multiple Access (FDMA) and Time Division Multiple Access (TDMA). With FDMA, the 25 MHz bandwidth is divided by frequency into 124 carrier frequencies, spaced 200 kHz apart, so each channel has a bandwidth of 200 kHz. With TDMA, carriers are then divided in time, allowing different users of a single RF channel to be allocated several time slots, with a maximum of 8 users.

The fundamental unit of time in GSM, known as a burst period, lasts for approximately 577 μ s. A TDMA frame is composed of 8 of these burst periods, resulting in a duration of 4.615 ms. One burst period allocated in each TDMA frame composes a physical channel.

The modulation used by GSM is called Gaussian Minimum Shift Keying (GMSK).

For maximum output power at the BS, GSM defines eight classes. Depending on the type of cell, maximum output power limits are those shown in Table 2.2. Since GSM performs power control, a lower value is usually used instead of the maximum one.

Table 2.2. GSM BS maximum output power (adapted from [Corr20]).

BS Maximum output power [dBm]		
Macro-cell	Micro-cell	Pico-cell
[34, 58]	[9, 32]	[13, 23]

UMTS uses Wideband Code Division Multiple Access (WCDMA) technology and FDD as the duplexing mode. By using WCDMA, multiple users share the same channel with different allocated codes. Table 2.3 shows the respective assigned frequency bands in Portugal.

With a chip rate of 3.84 Mcps, radio channels in UMTS have a carrier spacing of 5 MHz and a bandwidth of 4.4 MHz. However, any multiple of 200 kHz can be used as a carrier spacing in order to increase capacity. Each UMTS frame is equal to 10 ms.

Different modulation formats are required for UL and DL since they have distinct requirements and

conditions. In DL, the modulation used is Quadrature Phase Shift Keying (QPSK) with time-multiplexed control and data streams. Time multiplexing would be a problem in UL because the transmission would lead to interference. However, this is not relevant for DL, since in this case, the BS (NodeB) is sufficiently remote from any local audio-related equipment to ensure that interference is not a problem. In UL, the used modulation is Differential Coherent Phase Shift Keying (DCPSK), which makes use of two separate channels in order to deal with interference. In later versions of UMTS, higher-order modulation levels are used to achieve higher data rates. The maximum output power limits for UMTS are shown in Table 2.4.

Table 2.3. UMTS assigned bands in Portugal (based on [ANAC20]).

Band [MHz]	Uplink [MHz]	Downlink [MHz]	Total Bandwidth [MHz]
900	890-915	935-960	50
1800	1710-1785	1805-1880	150
2100	1920-1980	2110-21670	120

Table 2.4. UMTS BS maximum output power (extracted from [Corr20]).

BS Maximum output power [dBm]			
Macro-cell	Micro-cell	Pico-cell	Femto-cell
-	≤ 38	≤ 24	≤ 20

Using different multiple access methods for each link, LTE uses Orthogonal Frequency Division Multiple Access (OFDMA) for DL and Single-Carrier Frequency Division Multiple Access (SC-FDMA) for UL. Currently, there are several frequency bands defined by ANACOM for the operation of LTE. Table 2.5 shows the assigned bands in Portugal.

Table 2.5. LTE assigned bands in Portugal (based on [ANAC20]).

Band [MHz]	Uplink [MHz]	Downlink [MHz]	Total Bandwidth [MHz]
800	832-862	791-821	60
1800	1710-1770	1805-1865	120
2600	2510-2570	2630-2690	120

The difference in the multiple access methods used in DL and UL is due to the different requirements between the two links and the respective equipment. SC-FDMA has better power behaviour since it has a lower Peak to Average Power Ratio (PAPR). This lower PAPR value improves mobile terminals by helping with the efficiency of the power transmitted and the cost of the power amplifier. SC-FDMA combines the low PAPR offered by single-carrier systems with the multipath interference resilience and flexible subcarrier frequency allocation provided by OFDMA.

OFDMA divides the band into several orthogonal subcarriers with each user assigned to a certain number of Resource Blocks (RBs), defined as a set of 12 subcarriers by a set of 7 symbols, where each subcarrier has a bandwidth of 15 kHz. The minimum number of RBs allocated to a user,

N_{RB}^{min} , is two consecutive RBs in the time domain. The allocation in the frequency domain is modified every Transmission Time Interval (TTI) of 1 ms or subframe.

One of the key parameters associated with the use of OFDMA is the choice of bandwidth. The available bandwidth influences the number of subcarriers, N_{subc} . The relationship between bandwidths, number of subcarriers, and number of available RBs, N_{RB} , is shown in Table 2.6. Operators usually make use of higher bandwidths in order to have a greater channel capacity, achieving higher data rates.

Table 2.6. Relationship between bandwidths, number of subcarriers and number of available Resource Blocks (adapted from [Corr20]).

Bandwidth [MHz]	1.4	3	5	10	15	20
Number of subcarriers, N_{subc}	72	180	300	600	900	1200
Number of RBs, N_{RB}	6	15	25	50	75	100

OFDMA is quite resistant to multipath delay and spread. However, it is still important to implement methods that help to overcome Inter-Symbol Interference (ISI). In the presence of ISI, a guard interval can be added at the beginning of each data symbol. Later, a section from the end of the symbol can be copied to the start, allowing the receiver to sample the waveform at the optimum time and avoiding ISI, which is known as the Cyclic Prefix (CP). An important aspect related to this concept is the length of the CP: if it is not long enough, then it will not be able to counteract the multipath reflection delay spread, while, if it is too long, it will reduce the data rate capacity; therefore, 4.69 μ s is the value chosen for the standard length of the CP.

LTE subcarriers are spaced 15 kHz apart from each other. The symbol length is equal to the reciprocal of the Subcarrier Spacing (SCS) in order to maintain orthogonality. Thus, a symbol length of 66.7 μ s is used. Each LTE frame is equal to 10 ms, being composed of 10 subframes of 2 timeslots each.

LTE uses QPSK (2 bits per symbol), 16 Quadrature Amplitude Modulation (QAM) (4 bits per symbol) and 64 QAM (6 bits per symbol) modulation schemes to modulate data in UL and DL and 256-QAM for DL. When there is a high enough Signal-to-Noise Ratio (SNR), a higher-order modulation must be used. QPSK does not require such a large SNR but it is not able to send data as fast. A higher QAM offers a higher data rate but is less robust against noise and interference.

In LTE, the maximum power depends on the link. In DL, it is the power transmitted by the subcarrier, while in UL, it is the power transmitted for the total maximum bandwidth. LTE BS maximum output power values for LTE are presented in Table 2.7.

Similar to LTE, NR uses OFDMA for DL and for UL it can either use OFDMA or SC-FDMA. The duplexing modes used for NR are FDD and Time Division Duplex (TDD). Table 2.8. shows the assigned bands and respective multiplexing modes used in Portugal.

NR uses the same access methods as LTE but considers a more flexible approach. For NR, subcarriers do not necessarily have to ensure a fixed SCS of 15 kHz, having a flexible SCS given by:

$$\Delta f_{subc[\text{kHz}]} = 2^\mu \times 15 \quad (2.1)$$

where:

- μ : numerology.

Table 2.7. LTE BS maximum output power (extracted from [Corr20]).

BS Maximum output power [dBm]		
Macro-cell	Micro-cell	Femto-cell
-	≤ 24	≤ 23

Table 2.8. NR assigned bands in Portugal (based on [Corr20]).

Band [MHz]	Duplex mode	Uplink [MHz]	Downlink [MHz]	Total Bandwidth [MHz]
700	FDD	758-788	703-733	60
3600	TDD	3400-3800		400

Numerology can be taken as the SCS type. Since in NR there are several different types of SCS, it supports numerologies that can scale across the sub-6 GHz to the mm-waves.

The selection of the numerology depends on the size of the cell and the frequency band. Since larger cells have a higher time dispersion at the receiver, a higher CP is needed to counteract the larger dispersion. Higher numerologies are used for higher frequencies since a wider subcarrier is less sensitive to phase noise.

In NR, a slot is also composed of 14 symbols with the aggregation of slots constituting a subframe having the number of slots in a subframe depending on the numerology as represented in Fig 2.1. By having a bandwidth that is twice as much, the transmitting time will be reduced to half, therefore increasing the data rate. Each subframe has a length of 1 ms and a set of 10 subframes constitutes a frame equal to 10 ms.

As in LTE, resource elements are grouped into RBs but, in NR, an RB is defined only in the frequency domain, containing 12 subcarriers, independently of the used numerology.

Table 2.9 shows the supported numerologies and respective SCSs, number of symbols per slot, N_{symbol}^{slot} , number of slots per frame, N_{slot}^{frame} , number of slots per subframe, $N_{slot}^{subframe}$, and the minimum and maximum number of RBs allocated to a user N_{RB}^{min} and N_{RB}^{max} , respectively, for the normal CP.

5G NR supports QPSK, 16 QAM, 64 QAM and 256 QAM. The maximum power for NR can be seen in Table 2.7 since it is the same as for LTE.

There are two possible network implementation modes for 5G systems: Non-Standalone Access (NSA) relies on 4G networks to provide higher speed and data bandwidth, making the deployment of 5G easier, while Standalone Access (SA) has its own facilities in order to provide high speeds and ultra-low latency.

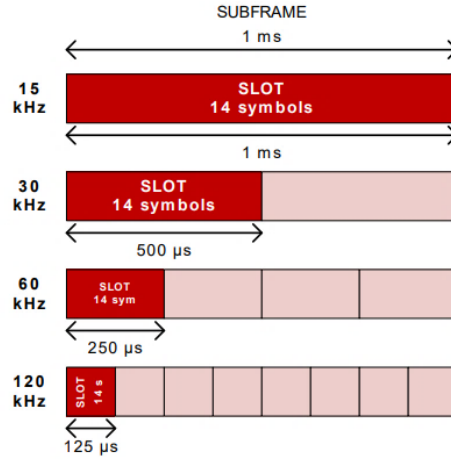


Figure 2.1. Representation of the dependency between the number of slots and numerology (extracted from [Camp17]).

Table 2.9. Numerologies and respective SCSs (based on [Corr20]).

μ	$\Delta f_{subc}[\text{kHz}]$	$f_c[\text{GHz}]$	N_{slot}^{sym}	N_{slot}^{frame}	$N_{slot}^{subframe}$	N_{RB}^{min}	N_{RB}^{max}
0	15	< 6	14	10	1	20	275
1	30	< 6	14	20	2	20	275
2	60	< 6, > 6	14	40	4	20	275
3	120	> 6	14	80	8	20	275
4	240	> 6	14	160	16	20	138

2.2 Base Station Deployments

This section, mainly based on [Corr20], addresses coverage, capacity and interference, which are the three main concepts to take into consideration when planning BS deployments.

Cellular planning is crucial to guarantee a good system performance and Quality of Service (QoS). It consists of placing BSs, establishing coverage and ensuring efficient management of radio resources, while minimising interference. Coverage can be defined as the geographic area where the BS is able to communicate and depends on several aspects, such as the technology used, orography and buildings, frequency, among others. The covered area is divided into cells, which can be divided into several types according to their radius, R , and to the relative position of the BS antennas to neighbouring buildings, Δh , also taking the transmitted power, P_{EIRP} , into account. Small cells can be classified as Micro-, Pico- or Femto-cells, the purpose being to increase capacity, data rate and overall network efficiency. Table 2.10 shows the output power, cell radius, number of users, location of the different types of cells and classification of BS antennas installation, according to coverage range, which can be seen in Table 2.11.

Based on [Corr20], and considering that L_{ref} and a_{pd} depend on the propagation chosen model, the cell coverage radius can be given by:

$$R_{cell[km]} = 10^{\frac{P_{EIRP}[dBm] - P_{rmin}[dBm] + G_{rtotal}[dB] - L_{ref}[dB]}{10 a_{pd}}} \quad (2.2)$$

where:

- P_{EIRP} : Effective Isotropic Radiated Power (EIRP);
- P_{rmin} : minimum power available at the receiving antenna;
- G_{rtotal} : total antenna receiver gain;
- L_{ref} : reference path loss;
- a_{pd} : average power decay.

Table 2.10. Output power, cell radius, users and location of different types of cells (based on [Corr20]).

Cell Type	Cell Radius [km]	Δh	P_{EIRP} [dBm]	Users	Location
Macro-cell (Large)	> 3	> 0	[50, 60]	> 2000	Outdoor
Macro-cell (Small)	1 - 3	> 0	[47, 50]	> 2000	Outdoor
Micro-cell	0.1 - 1	≤ 0	[30, 47]	100 to 2000	Indoor/Outdoor
Pico-cell	< 0.1	$\ll 0$	[22, 33]	30 to 100	Indoor/Outdoor
Femto-cell	< 0.05	$\ll 0$	[10, 25]	1 to 30	Indoor

Table 2.11. Classification of BS antennas installation according to the range (extracted from [Antu12]).

Denomination	Cell type	Environment	Installation type	Antenna height [m]
Rtower	Macro-cell	Rural, Suburban	Tower, Mast, Water sump, "Tree"	20-50
Uroof	Micro/ Macro-cell*	Urban	Rooftop	2-5**
Utower			Tower	20-40
Ufaçade	Micro-cell		Building façade	3-10
Upole			Light pole or other	3-5
Iceil	Pico-cell	In-building	Ceiling	2-3
Iwall			Walls	

* The cell type will depend on the coverage area

** Height from the rooftop

Considering a regular hexagon as a representation of a cell, it is possible to determine the cell coverage approximate area by:

$$A_{cell[km^2]} = \frac{3\sqrt{3} R_{cell[km]}^2}{2} \quad (2.3)$$

In NR, capacity depends strongly on the number of users and their type of service. It is characterised by the number of users that the system is able to serve with a given QoS and must be estimated in order to compute the number of required RBs that can be offered to the user. The number of RBs allocated to each user is given by:

$$N_{RB}^{user} = \frac{N_{RB}}{N_{users}} \quad (2.4)$$

where:

- N_{RB} : total number of RBs;
- N_{users} : total number of users.

According to [Mour20], the theoretical throughput for each user (excluding control and synchronisation data) for DL can be calculated as follows:

$$R_{b[\text{kbps}]}^{user} = \frac{N_{RB}^{user} N_{SC}^{RB} N_{symb}^{SF} [\text{symbols}] \log_2(M^n)_{[\text{bits/symbol}]} N_{streams}}{\tau_{SF}[\text{ms}]} \quad (2.5)$$

where:

- N_{RB}^{user} : number of RBs allocated to each user;
- N_{SC}^{RB} : number of subcarriers per RB;
- N_{symb}^{SF} : number of symbols per subframe;
- M^n : modulation order;
- $N_{streams}$: order of MIMO configuration;
- τ_{SF} : subframe duration.

After analysing (2.5) and assuming that all users have the same MIMO configuration, it is possible to conclude that the throughput per user is determined solely by the number of assigned RBs for each user and the modulation employed, as the remaining numbers are fixed for NR networks. As a result, the system's capacity can be defined as:

$$N_{users} = \left\lfloor \frac{N_{RB} N_{SC}^{RB} N_{streams} N_{symb}^{SF} [\text{symbols}] \log_2(M^n)_{[\text{bits/symbol}]}}{\tau_{SF}[\text{ms}] R_{b[\text{kbps}]}^{user}} \right\rfloor \quad (2.6)$$

Interference, noise and other sources of signal distortion, such as ISI, are all undesirable features of a mobile radio system, with interference being one of the most common.

Interference is responsible for decreasing the Signal-to-Interference-plus-Noise Ratio (SINR), causing throughput to decrease, as well, at the risk of not being able to supply the required service. Special care must be taken at the cell edge, since as one moves away from the cell centre, the power of the carrier of the desired signal decreases and the power of the carriers of the interfering signals increases, reaching the minimum and the maximum values at the cell edge, respectively. The use of different cell sizes also leads to an increase of interference due to the lack of uniformity in the cellular structure, requiring additional care in the location of the BSs in transition regions. Interference may be reduced by using sectorised cells, downtilting the main lobe of the BS antenna, lowering the BS antenna, optimising the location of the BS, using frequency hopping or power control.

Noise may play a role, for example, when the mobile terminal goes away from the BS and the received power decreases. Given the case under study, noise can be neglected.

2.3 Antennas in 5G

Based on [HUAW19a] and [Mand19], this section approaches 5G antennas.

2.3.1 Arrays and Beamforming

The fast development of 5G has resulted in antennas able to support flexible all-band configuration and scenario-specific beam management. These active antennas suffer from fewer cable and power losses than passive ones. The integration of these two types of antennas is accomplished through interleaved design, which reduces occupied space and facilitates installation. For example, AAs are commonly found in streetlamps.

To improve accuracy and network capacity, 5G AAs use high-precision beamforming to implement a flexible beam configuration, resulting in a more efficient transmission. It consists of narrow beams with adjusted widths and changing directivity that sweeps across the desired areas, having no cover failures, minimal overlap coverage, maximum Reference Signal Received Power (RSRP) and SINR.

With beamforming, antennas can radiate highly focused beams towards specific users rather than spreading in all directions. Some AAs are even capable of beamforming in both horizontal and vertical planes (full-dimension MIMO). Beam steering allows a beam pattern to be adjusted dynamically in real-time by adjusting the signal phase without changing the antenna elements. Because beams can discover any point in space thanks to mobile network feedback, the service is available at all times, even when the user is moving.

Antennas must also support Multi-User (MU) beamforming so that multiple user beams are able to share time and frequency domain resources, maximising spectral efficiency. Networks can switch between serving one or multiple users simultaneously, with beams being usually narrower, with more focused power, when serving only one user and wider when serving MUs at different spatial positions.

MU beamforming requires accurate pointing toward MUs and accurate null-steering to users. Null-steering or zero-forcing precoding is a method of spatial signal processing by which an antenna with multiple transmitters is able to null the MU interference. Multi-user beamforming coverage behaviour is represented in Figure 2.2.

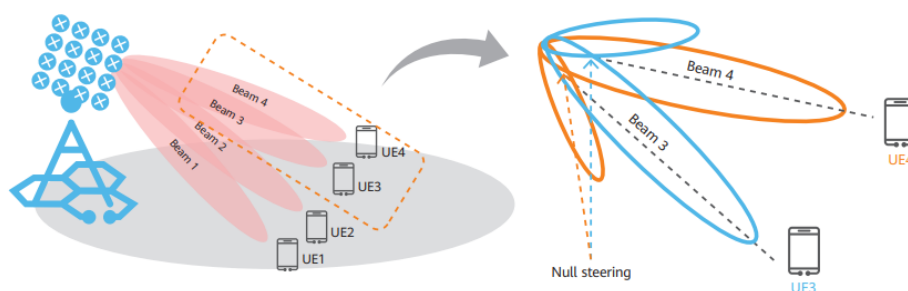


Figure 2.2. Multi-user beamforming accurate coverage (extracted from [HUAW19a]).

5G has scenario-oriented management, meaning the network automatically recognises scenarios and configures beams accordingly through Artificial Intelligence for IT Operations (AIOps) and maintenance. Antennas generate beams with different widths and directions, improving user experience by meeting the requirements of the several application scenarios so that the energy is focused on the desired areas, minimising interference. While wide beams are suitable for buildings, narrow beams with specific directivity are mandatory for highways.

As 5G evolves, the number of IoT terminals increases. 5G antennas use beamforming to obtain the Direction of Arrival (DoA) of the signals that reach the terminals. Based on high-precision measurements, antennas can generate absolute geographical coordinates. Thus, the Global Positioning System (GPS) not being able to determine the position of IoT terminals with high power consumption and Location-based Service (LBS) is no longer a problem.

Thanks to shorter wavelengths (compared to previous systems) MIMO antennas have evolved to mMIMO. The latter can have several elements to send and receive more data simultaneously (192 or more deployed for current bands such as 2.3 GHz TDD, 2.5 GHz TDD and 3.6 GHz TDD and 256 elements or more for mm-waves bands).

NR antennas can be seen as matrices with $N \times M$ elements. In order to generate beamforming beams, a minimum of 2 antenna array columns is required. Therefore, NR antennas must support a minimum of 2 arrays on each band, i.e., at least a 4T4R configuration on each band. Most implementations use at least 4 columns. MIMO requires uncorrelated channels with a typical column spacing of around 0.7λ or above. However, its best performance happens with closely spaced arrays having 0.5λ as the recommended distance between columns.

According to the pattern multiplication rule, the total field of an antenna array can be determined as the product of the field of a single antenna multiplied by an array factor, F_{aa} , which can be obtained by considering the antenna elements to be point sources [Bala16]. Hence, the total electric field radiated by an array with N_{ele} identical elements can be given by:

$$\mathbf{E}_{aa} = \mathbf{E}_{ele} F_{aa} \quad (2.7)$$

where:

- \mathbf{E}_{ele} : electric field radiated by a single element.

Considering a dipole, the electric field radiated by a single element is given by [Corr20]:

$$\mathbf{E}_{ele}(\theta, r_{obs}) = j \frac{Z_0 I_m e^{-jk r_{obs}}}{2\pi r_{obs}} \frac{\cos(kl \cos(\theta)) - \cos(kl)}{\sin(\theta)} \mathbf{u}_\theta \quad (2.8)$$

$$k = \frac{2\pi}{\lambda} \quad (2.9)$$

where:

- θ : elevation angle, i.e., the angle between the positive half of z-axis and the observation point;
- r_{obs} : distance between the antenna and the observation point;
- Z_0 : free-space impedance;
- I_m : maximum current;
- k : wavenumber;
- l : half of the length of the wire antenna;
- λ : wavelength of the transmitted electromagnetic wave.

According to [Bala16], a vertical linear array of N_{ele} antennas with uniform amplitude and spacing has an array factor given by:

$$F_{aa} = e^{j(N_{ele}-1)\psi/2} \left(\frac{\sin(N_{ele}\psi/2)}{\sin(\psi/2)} \right) \quad (2.10)$$

where:

- ψ : total phase difference between the signals from the antenna elements when they reach the observation point in the far-field.

The total phase difference is given by:

$$\psi_{[\text{rad}]} = k d_{ele} \cos(\theta) + \beta \quad (2.11)$$

where:

- d_{ele} : distance between the antenna elements of the array;
- β : phase difference between any two successive antenna elements forming the array.

The distance between the antenna elements of the array is uniform and can be given by the wavelength multiplied by the element spacing factor:

$$d_{ele} = \Delta_{ele} \lambda \quad (2.12)$$

where:

- Δ_{ele} : element spacing factor.

The element spacing factor may be provided by the antenna manufacturer, not being usually included in the equipment's datasheet.

If the reference point happens to be the array's physical centre, the antenna array factor is reduced to:

$$F_{aa} = \left(\frac{\sin(N_{ele}\psi/2)}{\sin(\psi/2)} \right) \quad (2.13)$$

One should notice that the maximum value of (2.13) is equal to N_{ele} . Therefore, the normalisation of the antenna array factor, F_{aa}^{norm} , should be considered:

$$F_{aa}^{norm} = \frac{1}{N_{ele}} \left(\frac{\sin(N_{ele}\psi/2)}{\sin(\psi/2)} \right) \quad (2.14)$$

By changing the amplitudes, phases and spacing, it is possible to create a wide variety of patterns, making possible almost any specified radiation pattern. One can determine an approximated mathematical function to describe the generalised gain $G(\theta, \phi)$ based on the analysis of the antenna patterns. Hence, the generalised gain of the antenna can be determined for any direction by:

$$G(\theta, \phi) = G_M f_{\theta\phi}(\theta, \phi) = G_M f_{\theta}(\theta) f_{\phi}(\phi) \quad (2.15)$$

where:

- G_M : maximum gain of the antenna;
- $f_{\theta\phi}(\theta, \phi)$: normalised three-dimensional antenna radiation pattern;
- $f_{\theta}(\theta)$: normalised antenna radiation pattern in the vertical plane;
- $f_{\phi}(\phi)$: normalised antenna radiation pattern in the horizontal plane.

2.3.2 Radiating Field Regions

The surroundings of an antenna are usually divided into three regions: Reactive near-field, Radiating near-field (Fresnel) and Far-field (Fraunhofer), presented in Figure 2.3.

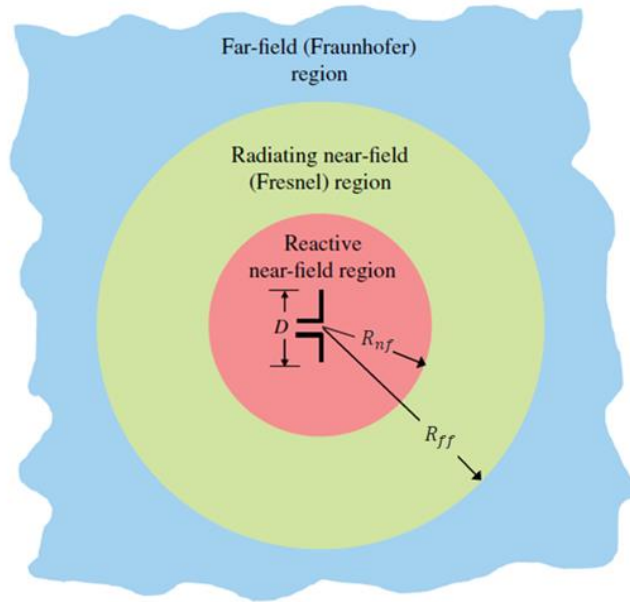


Figure 2.3. Radiating field regions (adapted from [Bala16]).

Considering the 700 MHz and 3600 MHz bands, it is possible to define the boundaries of these different regions. The Reactive Near-Field Region, $r_{obs} < R_{nrf}$, is the closest one to the centre of the antenna [Bala16]. The border of this region, R_{nrf} , can be calculated by:

$$R_{nrf} = 0.62 \sqrt{\frac{D^3}{\lambda}} \quad (2.16)$$

where:

- D : the largest dimension of the antenna.

In this region, fields are predominately reactive fields, meaning electric, E , and magnetic, H , fields are out of phase by 90° .

The Radiating Near-Field (Fresnel) region is the one between the Reactive Near-Field and the Far-Field ones, $R_{nrf} < r_{obs} < R_{ff}$, where the far-field boundary, R_{ff} , is given by:

$$R_{ff} = \frac{2D^2}{\lambda} \quad (2.17)$$

is only true for free-space propagation and antennas with $D \gg \lambda$. In this region, reactive fields are not dominating and radiating fields begin to emerge. The shape of the radiation pattern may vary with distance. This region may or may not exist, depending on the values of D and λ .

The far-field (Fraunhofer) region is the furthest one from the antenna, where the radiation pattern shape does not change with distance. The E and H fields decrease with $1/r_{obs}$, while the power density, S , decreases with $1/r_{obs}^2$.

As the observation distance varies from the reactive near-field to the far-field, the amplitude pattern of an antenna changes in shape because of variations in magnitude and phase of the fields. Typical changes in antenna amplitude pattern shape from reactive near-field toward the far-field are represented in Figure 2.4.

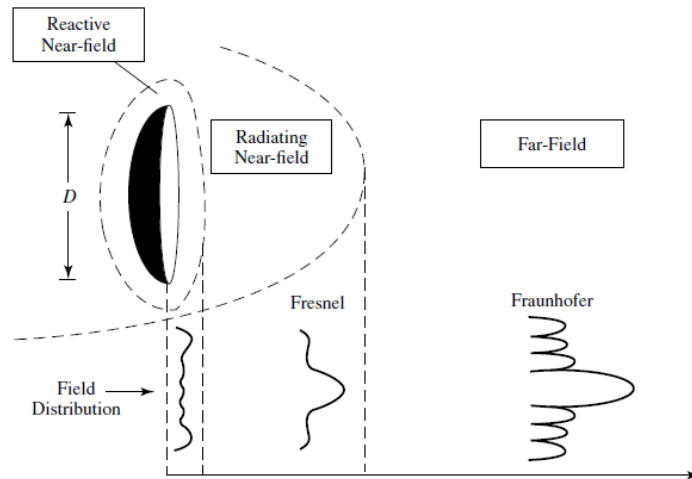


Figure 2.4. Typical changes of antenna amplitude pattern shape from reactive near-field toward the far-field (extracted from [Bala16]).

Generally, in the reactive near-field region, the pattern is more spread out and nearly uniform, only with slight variations. Moving to the radiating near-field region (Fresnel), the pattern begins to smooth and form some lobes. In the far-field region (Fraunhofer), the pattern is well defined, consisting of a few minor lobes and one, or more major lobes.

2.4 Services and Applications

This section presents an overview of 5G services and applications. The main use cases for 5G are defined as well as the corresponding needed features and functionalities. There are many use cases (grouped into three categories), characterised by the performance attributes required.

Enhanced Mobile Broadband (eMBB) is an evolution of 4G networks that provides higher data rates, offering a better user experience. Broadband access should be available everywhere, providing a higher capacity. Higher user mobility will also be provided, since eMBB will enable mobile broadband services in moving vehicles, such as cars, buses, planes and trains. In a scenario with static or slow-moving users, there will be a requirement for very high traffic capacity but the requirement for mobility will be low. In contrast, in a scenario where users are passengers on a high-speed train, there would be a high requirement for mobility. However, traffic capacity requirements will be lower than in the previous scenario. eMBB will work across all connected devices, enabling applications such as VR, AR, real-time video monitoring, virtual meetings with 360° video, and real-time interaction.

Ultra-Reliable Low Latency Communications (uRLLC) will enable multiple services with very low latency, such as factory automation, autonomous driving, industrial internet and smart grid or robotic surgeries. With low latency, networks can be optimised in order to be able to process high amounts of data with minimal delay. In order to achieve low latency, all the devices have to synchronise to the same time-base. These networks need to adapt to these large amounts of data changing in real-time. While uRLLC is one of the most promising additions to 5G capabilities, it will also be the hardest to guarantee since it requires a completely different QoS.

Massive Machine Type Communications (mMTC) is a type of communication between machines over networks, where there is minimal to no intervention from humans. Wireless connectivity, amongst massive numbers of machines, is considered to be the key aspect that raised IoT to the Internet of Everything (IoE). Limited by the required connectivity to support large numbers of Machine to Machine (M2M) interactions and low energy consumption, mMTC uses small data packets, not optimally supported by the cellular networks designed for human communication.

Multi-band and ultra-wide bandwidth capabilities combined with mMIMO enable networks to support the eight key features used by the three leading use cases. Figure 2.5. maps the key capabilities into the different application scenarios. While eMBB presents a vast range of requirements, mMTC and uRLLC show more specific needs.

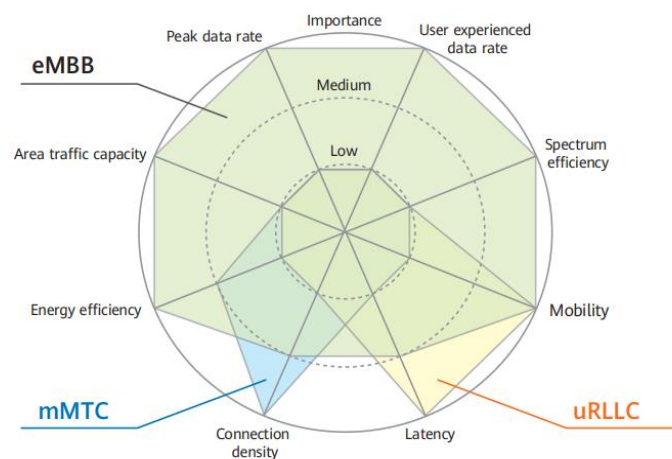


Figure 2.5. Key capabilities in different application scenarios (extracted from [HUAW19a]).

QoS is the measurement of the overall performance of a service, particularly the one seen by the network. To quantitatively measure QoS, some aspects of the service must be considered. Services can be grouped into four main classes: Conversational are real-time services, in which a low delay is very important; Streaming is characterised by unidirectional real-time data flow, and delay is not as important as in the previous service; Interactive is characterised by remote access; Background is characterised by exchanging data in the background, being the least delay-sensitive service of all.

In order to measure the overall performance of each service from the user's viewpoint, one must use the Quality Channel Indicator (QCI) that carries information regarding the communication channel's quality (channel quality increases with the increment of QCI). LTE and NR have defined priority classes, and a service can either be assigned a Guaranteed Bit Rate (GBR) bearer that guarantees a minimum

bit rate for the service or a Non-Guaranteed Bit Rate (nGBR) one, suitable for non-real-time services.

2.5 EMF Radiation Exposure

This section studies EMF behaviour and radiation exposure guidelines, as well as measurement methods.

2.5.1 EMF Radiation

The World Health Organisation (WHO), the Scientific Committee on Emerging and Newly Identified Health Risks (SCENIHR) of the European Union (EU) and ICNIRP play an essential role in protecting the general public from EMFs.

In response to the public concern regarding the health effects of exposure to EMFs, WHO has established the International EMF Project in 1996 to assess the scientific evidence of possible health effects of EMF radiation in the frequency range from 0 to 300 GHz, encouraging research in this area and facilitating the development of internationally acceptable standards limiting EMF exposure [Wor120].

ICNIRP and the Institute of Electrical and Electronics Engineers (IEEE) have defined exposure guidelines and limits in terms of Specific Absorption Rate (SAR), electric field strength, magnetic field strength and power density in the 5G frequency range. These exposure limits may differ in some countries.

In this thesis, ICNIRP guidelines are adopted as EMFs radiation exposure limit values. These guidelines provide a high level of protection against adverse health effects from exposures to RF EMFs. Some exposure scenarios, e.g., medical ones, are considered to be outside the scope of these guidelines since ICNIRP assumes that those rely on medical knowledge to identify potential risks and compare them with the possible benefits [ICNI20].

When a signal propagates away from a source, it may encounter obstacles, interacting with the constituting matter. If a human body is exposed to RF EMFs, some of the power is absorbed. The results of EMF exposure are then present in the body, being strongly dependent on the EMF characteristics, as well as the physical properties and dimensions of the body.

The electric field inside the body is referred to as induced electric field, E_{ind} , which “exerts a force on both polar molecules and free-moving charged particles, such as electrons and ions. In both cases, a portion of the EMF energy is converted into kinetic energy, forcing the polar molecules to rotate and the charged particles to move as a current. As the polar molecules rotate and charged particles move, they typically interact with other polar molecules and charged particles, causing the kinetic energy to be converted to heat, which can adversely affect health” [ICNI20].

It is important to define appropriate metrics according to the different types of penetration into the body.

At below 6 GHz, where EMF radiation penetrate deep into the tissue, it is preferable to describe SAR (the power absorbed per unit mass, W/kg). In order to suit different health effects, SAR is defined over different masses. While whole-body average SAR represents power absorbed per kg over the entire body, SAR10g represents the power absorbed per kg over a 10 g cubical mass.

In order to facilitate the evaluation of EMF radiation, reference level quantities were defined, such as the Incident Electric Field Strength, E_{inc} , Magnetic Field Strength, H_{inc} , and Power Density, S_{inc} . The reference levels for E , H and S have been derived from studies assuming whole-body exposure to a uniform field distribution, which is generally the worst-case scenario.

An important aspect to take into account is the averaging time, since this is the appropriate time over which exposure is averaged for purposes of determining compliance. ICNIRP considers 4 W/kg averaged over 30 minutes as the RF EMF exposure level corresponding to a 1°C rise in body core temperature. Therefore, in order to adopt a conservative position, an averaging time of 30 min is used to take the time it takes to reach a steady-state temperature into account.

Reference levels for exposures averaged over 6 min and 30 min are shown in Table 2.12 and Table 2.13, respectively. Regarding the reference levels for an exposure ≥ 6 min, a graphic representation is done in Figure 2.6, considering unperturbed Root Mean Square (RMS) values. One should note that “Not Applicable” (NA) means that the entity does not need to be taken into account when determining compliance. E_{inc} , H_{inc} and S_{inc} are to be averaged over 30 min, over the whole-body space. For frequencies between 2 GHz to 300 GHz, within the reactive near-field zone, reference levels cannot be used to determine compliance, so one must use basic restrictions.

Table 2.12. Reference levels for local exposure, averaged over 6 min, to EMFs from 400 kHz to 6 GHz (unperturbed RMS values) (based on [ICNI20]).

Exposure scenario	Frequency range, f [GHz]	Incident electric field strength, E_{inc} [V/m]	Incident magnetic field strength, H_{inc} [A/m]	Incident power density, S_{inc} [W/m ²]
General public	[0.4, 2]	$4.72f_{[MHz]}^{0.43}$	$0.0123f_{[MHz]}^{0.43}$	$0.058f_{[MHz]}^{0.86}$
	[2, 6]	NA	NA	40

Table 2.13. Reference levels for exposure, averaged over 30 min and the whole body, to electromagnetic fields from 400 kHz to 300 GHz (unperturbed RMS values) (based on [ICNI20]).

Exposure scenario	Frequency range, f [GHz]	Incident electric field Strength, E_{inc} [V/m]	Incident magnetic field Strength, H_{inc} [A/m]	Incident Power Density, S_{inc} [W/m ²]
General public	[0.4, 2]	$1.375f_{[MHz]}^{0.5}$	$0.0037f_{[MHz]}^{0.5}$	$f_{[MHz]}/200$
	[2, 300]	NA	NA	10

The most commonly used ICNIRP reference levels for exposure are the ones averaged over 6 min and 30 min. However, it is possible to determine reference levels for exposure for lower averaging times by using the reference levels for local exposure, integrated over intervals of between 0.5 min and 6 min, presented in Table 2.14. These values can be useful when investigating EMF exposure in scenarios where the average service duration is less than 6 min.

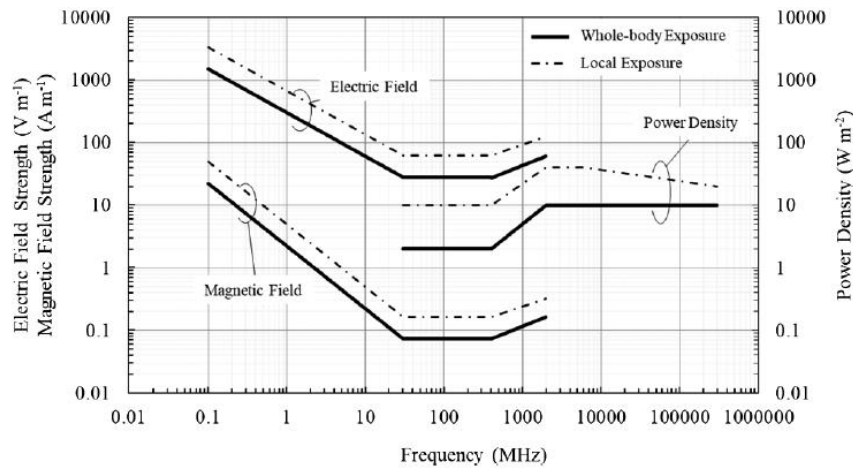


Figure 2.6. Reference levels for E , H and S , for time-averaged general public exposures higher than 6 min from 100 kHz to 300 GHz (unperturbed RMS values) (extracted from [INC120]).

Table 2.14. Reference levels for local exposure, integrated over intervals between 0.5 min and 6 min, to EMFs from 400 kHz to 6 GHz (unperturbed RMS values) (based on [ICNI20]).

Exposure scenario	Frequency, f [GHz]	Incident Energy Density, U_{inc} [kJ/m ²]
General public	[0.4, 2]	$0.058 f_{[MHz]}^{0.86} \times 0.36 [0.05 + 0.95(t_{[s]}/360)^{0.5}]$
	[2, 6]	$40 \times 0.36 [0.05 + 0.95(t_{[s]}/360)^{0.5}]$

Since reference levels may often be exceeded even if the respective basic restrictions are not, one should always verify both. In the case of simultaneous exposure to multiple frequency fields, it is important to understand if the effects of the exposures add up.

Based on [PaKŽ19], the evaluation of compliance with the guidelines for EMF exposure is achieved by measuring the resulting levels of EMF and comparing them with the reference levels. Measurements are usually performed in the far-field area, where the field behaves like a plane wave (E and H fields are orthogonal to each other). The use of mMIMO and beamforming together with high-frequency bands results in the fact that the distribution of EMF energy in the proximity of a BS does not meet the requirements of the deterministic model. However, it may be described in a probabilistically way.

2.5.2 Exclusion Zones

There are some regions near the antenna, usually some metres within the near-field region of the BS,

where human exposure limits are known to be exceeded, which are usually positioned around antennas on rooftops in urban or suburban scenarios. These regions may require physical delimitation or signalization in order to protect the general public from radiation exposure, unless the antennas are on masts, especially in rural scenarios, in an area that is not accessible to the general public.

BS installation characteristics, along with some relevant parameters and recommended values, are essential for the estimation of exclusion zones around BSs and specific procedures are needed for the evaluation of EMFs near BSs.

The radiated field behaviour is not the same for each of the three regions surrounding an antenna, hence, the importance of accurate propagation models to accurately estimate the field strength at any given distance. For typical radiated power values and antenna dimensions, the field at the minimum far-field distance is below the recommended values. However, it is essential to guarantee improved near-field propagation models for the estimation of the exclusion zones [OFRC05].

Exclusion zones may be determined either through measurements or prediction, using complex simulations or applying simple models that enable the calculation of radiation levels in the vicinity of BS antennas. The last one is considered to be the most practical solution, since most models are very accurate and relatively simple to apply, while measurements and simulations are more time-consuming and require powerful equipment in order to generate precise results.

In the literature, several models for the estimation of EMFs in the far- and near-field regions of BS antennas can be found, aiming to provide simple formulas that would, otherwise, be available only through complex simulations. [OFRC05] does a brief analysis of six of these models. The validity of the models is presented in Figure 2.7. It is possible to conclude that, while the far-field model is the one with the narrower validity range, the cylindrical exclusion model is one of the models with a wider one, having a very simple definition of the corresponding exclusion zones.

According to [OFRC05], the best approach is to start by estimating the far-field region to see if it is possible to use the far-field model, since it is the simplest one. If the far-field distance is too large and the computed power density at that distance happens to be far below the threshold values, then one should choose a model with a smaller validity range, since it allows one to obtain results at a smaller distance, closer to the antenna. A simpler but more dependable approach is to consider the minimum valid distance for the model as the limit for the exclusion zone, assuming that the determined distance is adequate for the type of BS installation, even if the power density is below the threshold level.

The distance values determined in most of the models consider the worst-case scenario and the direction of the main lobe of the antenna, D_{front} . In order to obtain the remaining distances, D_{back} , D_{side} , D_{top} and D_{bottom} , correction factors may be applied to D_{front} or to the maximum antenna gain. The representation of an antenna exclusion zone can be seen in Figure 2.8.

In order to determine the antenna exclusion zone, an analysis of the performance parameters is done with the most fundamental ones being:

- Averaging time, T : It is the time over which exposure is averaged for purposes of determining compliance. Devices are capable of actively monitoring and adjusting power output over time in

order to comply with exposure limits, which are based on average exposure over a time period. As frequency increases, the depth of penetration decreases and SAR increases at the skin surface, decreasing the averaging time.

- Electric field strength, E : the electric field is a parameter that is under constraints in order to protect the health of the general population, which can be measured on-site or determined through mathematical models.
- Power density, S : Also under constraints, power density can be determined through both E and H fields or just one of them, depending on the radiating field region. If both E and H field values are lower than the most limiting reference value, the power density must also be lower.

Validity range [m]	Propagation models validity range (expression of the power density)							
	0	$\frac{\lambda}{2}$	λ	2λ	3λ	$\frac{D^2}{4\lambda}$	$\frac{\alpha_{3dB} G(\theta, \phi) D}{4\pi}$	$\frac{2D^2}{\lambda}$
Far-field model								
Far-field Approximation								
Far-field gain-based model								
Gain based model								
Synthetic based model								
Cylindrical exclusion zone								
Hybrid								

Figure 2.7. The validity range of several surveyed propagation models (extracted from [OFRC05]).

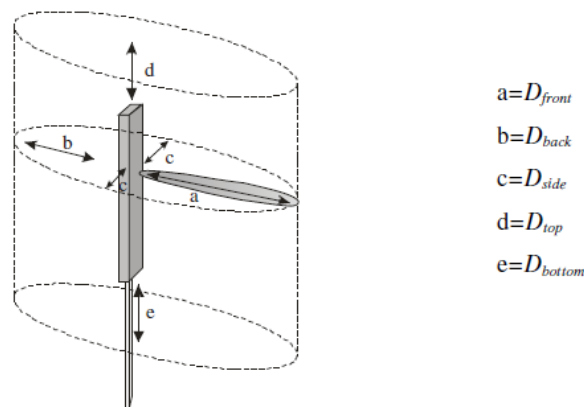


Figure 2.8. Representation of an antenna exclusion zone (extracted from [OFRC05]).

2.6 State of the Art

In this section, an overview of previous research related to the thesis is done. Despite the number of dedicated studies in the literature, the influence of 5G deployment on EMF levels is still unclear.

Not every published work addresses all the important aspects required to achieve the main goal of this thesis. Thus, a slightly deeper analysis of the most complete and appropriate studies is done, regarding frequencies, technologies and deployments used, as well as possible models provided for measuring EMFs radiated by 5G antennas.

[InTU20a] and [InTU20b] consist of two workshops about 5G and EMFs, organised by the ITU. Some issues, such as tight EMF limits decreasing the QoS experienced by users and increasing the installation costs for operators (due to the impossibility of the reuse of existing sites) were raised.

In [InTU19], an analysis of 5G technology and the consequent human exposure to RF EMFs is made, although a model for measuring the radiated power is not provided. The implications of EMF exposure on 5G devices are assessed in [Nasi19], [CoTT15], [TCYB16], [XZYS19], [XGSY18] and [XZTC17], which present, in some cases, different power measurement schemes for EMF compliance assessment of 5G deployment. In [XGSY18], the problem of exposure compliance of the User Equipment (UE) with MIMO systems is addressed and an evaluation of EMF exposure in the frequency range of [10, 60] GHz for an array of antennas is done in [TCYB16]. In [ZGLZ17], a ray-tracing technique is used to evaluate the body effects on the channel characteristics in DL at 15 GHz and 28 GHz; their results are assumed for devices close to users (up to dozens of centimetres). However, all previously mentioned studies only take frequencies above 6GHz into consideration, which is not the case in our study.

In [PaKŽ19], issues and challenges related to EMF measurements in 5G technology are analysed. Two methods for EMF exposure assessment are presented, namely, broadband measurement, where the identification of frequency components is not possible, and frequency-selective measurement, allowing for selective measurements in the frequency domain and enabling the determination of the EMF level in a well-defined frequency range. The obtained results, from both methods, reflect the level of EMF exposure in the vicinity of a BS. However, the measurements are usually performed in the far-field area.

In [BWWG18], a statistical approach for the computation of EMF exposure, considering mMIMO systems and exploiting narrow beams, is provided. By taking a three-dimensional spatial traffic model into account, it was possible to conclude that the exclusion zone is approximately half of the one in the traditional case, based on the maximum radiated power in all directions.

In [TWGH20], a new average power feedback controller has been developed. For a given distance, the power density limit can be turned into a power limitation. Therefore, taking the maximum beam gain, the exclusion zone corresponding to the maximum EIRP of the BS can be reduced to one corresponding to a selected maximum average power, computed over a given time interval. Since traffic may fluctuate, the instantaneous power can be quite higher than this selected maximum average power during shorter durations than the given time interval. However, the transmitted average power must be guaranteed to always be below the determined average power threshold. This paper has designed, validated and

characterised a new average power feedback controller that guarantees all these requirements.

In [CCMF18], the planning of 5G networks under EMF constraints is addressed. Two realistic case studies are presented, showing the saturation of EMF levels occurring under current 2G/3G/4G networks, as well as the negative impact of strict regulations on network planning and user QoS. The first case study considers a portion of the Fuorigrotta district, in Naples, Italy, where EMF levels are determined using a ray-tracing simulator. Results show that, for the maximum input power and 75% of the maximum input power, several zones exceed the Italian limits for EMF exposure, reinforcing the concern that these limits (below the ones proposed by ICNIRP) may significantly limit the deployment of 5G network structures. The second case studies the Torrino Mezzocammino area in Rome, Italy, resorting to CellMapper, a monitoring application able to collect different features of BSs. In this region, results show that several zones experience very low values of received power (equal or below 110 dBm).

In [TFCT17], a model to compute realistic maximum power levels of 5G BSs with mMIMO is proposed. Results have shown that the time-averaged radiated power is approximately between 7% and 22% lower than the maximum theoretical one, which can be translated into a reduction of the distance from the antenna to the compliance limit up to 60% compared with the more common evaluations.

In [CJPT20] and [CJXG20], an analysis of the actual power and EMF exposure from BSs with mMIMO antennas in a Commercial 5G Network is done. Since the results are based on actual measurements, they end up being highly influenced by the surrounding environment and software limitations. While an exclusion zone is only determined in the second work, both of them make several assumptions and simplifications, affecting the results. However, those end up being in accordance with the ones presented by other works.

In [Jevr20], exclusion zones are determined for different countries in Europe, based on actual power and EMF exposure estimation from other known works. This paper can be seen as a simplified and conservative work since, for example, it is assumed that the gain is the same in all directions inside the vertical and horizontal beam range.

Finally, in [Mour20], an analysis of the impact of EMF restrictions on 5G BSs deployment in the existing network is done. A model for estimating the exclusion region of a BS is proposed, which estimates the power density as a function of distance for each mobile communication system and any given direction by using far- and near-field mathematical models and considering the antennas being continuously radiating at maximum power. Taking representative scenarios of BSs with co-location of antennas, an analysis on the exclusion zone distance is made before and after the installation of NR. The obtained results support that, for urban scenarios, the highest increase is 248.7%, while, for suburban and rural scenarios, it is 131.6% and 56.4%, respectively.

Chapter 3

Model Development and Simulator Description

This chapter presents an overview of the general model along with a description of the model development. An exclusion zone evaluation model is presented and assessed.

3.1 Model Overview

With the fundamental theoretical concepts consolidated, an overview of the different sub models required to fully solve the problem at hands is provided, along with a brief description of the main input and output parameters of the main model. A representation of the model configuration is presented in Figure 3.1.

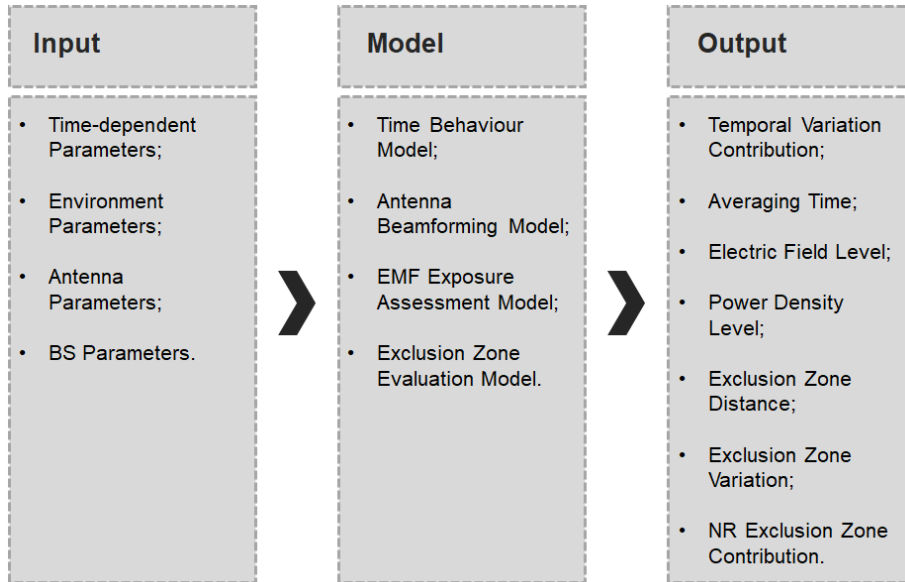


Figure 3.1. Model configuration (based on [Mour20]).

When estimating exclusion zones for scenarios with mMIMO 5G AAs, one may notice that the maximum beamforming gain and EIRP may increase significantly compared to traditional scenarios with passive antennas. Hence, in this case, the commonly used methods for estimating the exclusion zones based on the maximum EIRP may generate overly conservative results. In order to mitigate some deployment challenges due to this overly conservative use of the maximum EIRP when determining exclusion zones, the estimation of the exclusion zones based on a time-averaged EIRP is considered. Since the goal is to determine time-averaged realistic maximum power levels, it is necessary to estimate the temporal variation contribution to exposure, T_{var} , taking users' mobility and services' characteristics into account. Therefore, a time behaviour model was developed in order to estimate the duration of a service and an antenna beamforming model was developed to estimate mobility, distinguishing user's movement.

Then, the general model for estimating exclusion zones around a BS was developed, taking the EMF exposure assessment model and the previous estimation of T_{var} into account. Since regulation is based on the total exposure of a site, the variation of the exclusion zone when an NR antenna is installed in a BS with GSM, UMTS, and LTE technologies must be determined. Thus, the exclusion zone distance needs to be computed before and after the installation of the NR antenna.

The inputs for the model can be divided into four categories. Time-dependent parameters, such as the usage duration of the service, the system utilisation and the user distribution and mobility, are essential to determine the temporal variation contribution.

Environment parameters, such as terrain undulation, vegetation density, building density and height, open areas density and water areas density take the environment characteristics where the BS is installed into account. Usually, the environment can be classified as urban, suburban or rural.

Antenna parameters such as type of system, frequency range, maximum input power, gain, radiation pattern, beamwidth, sidelobe level, front-to-back ratio, polarisation, directivity, effective aperture, number of subcarriers, carriers frequencies, antenna type/number of sectors, tilt, azimuth, MIMO order, and antenna dimensions (height/width/depth) are relevant to use as inputs for the models, along with some BS parameters, such as active systems, installation type, cell type and BS height.

Regarding output parameters, seven different outputs can be estimated. The temporal variation contribution and the averaging time are the outputs from the first two models, becoming the drivers of the following ones. The temporal variation contribution is expected to generate smaller exclusion zones, since the actual power density is expected to be significantly smaller than the maximum one. The electric field and correspondent power density levels are computed, as a function of distance, in order to allow for the computation of the exclusion zone. The exclusion model is then able to compute the exclusion zone distance. Consequently, the exclusion zone variation and NR contribution may also be determined.

3.2 Temporal Variation Contribution

This section studies the temporal variation contribution to the EMF exposure near AAs, caused by a set of system parameters, such as the number of served users, service usage duration and user's mobility in order to obtain time-averaged realistic levels for EMF exposure assessment.

3.2.1 Temporal Variation

Since the goal of this thesis is to determine the EMF compliance distance, i.e., the distance at which the power density, S , is equal to the EMF limit, S must be averaged over time, as well as all the parameters that contribute to it. Therefore, it is necessary to consider and evaluate the main parameters responsible for the temporal variation of antenna parameters, such as power and gain.

Considering a scenario where the user is located within Line-of-Sight (LOS) from the BS antenna, a focused beam is used. In the case of a Non-Line-of-Sight (NLOS) propagation, the system may transmit simultaneously in several directions. However, the maximum exposure is usually caused by focused beams, therefore, in this thesis, the LOS scenario is considered. AAs can steer beams and change their shapes, focusing the energy on the desired direction by changing the gain. In NR, EIRP is considered to be a very useful power measurement, since it is a reliable indicator of signal strength cell-wide.

Usually, when dealing with mMIMO, EIRP is defined per beam. Since it is not useful to have all beams transmitting simultaneously because it would deteriorate SINR and reduce throughput, only some beams are active at the same time. Deciding which beams to activate is made in real time, trying to minimise interference. Therefore, EIRP per beam must be averaged out.

Time-averaged EIRP in elevation and azimuth (θ, ϕ) , can be determined as a function of time using:

- total time-averaged transmit power, \bar{P} ;
- time-averaged gain, $\bar{G}(\theta, \phi)$.

The assessment of \bar{P} is based on the number of RBs scheduled by the BS for DL transmission, providing a measure of the total cell-wide time-averaged transmitted power. However, it does not provide any information on its spatial distribution [BWWG18]. Since beams are constantly switching on and off, the spatial distribution of the transmit power will vary over time, depending on the beam selection for transmission, which makes the radiation pattern change in real time.

Therefore, the dynamics of the antenna radiation patterns should be studied, taking the time-averaged gain, $\bar{G}(\theta, \phi)$, into account, which can be obtained by averaging the antenna radiation patterns [CJXG20]. The gain is three-dimensional, varying in space and assuming a peak along a direction perpendicular to the antenna panel (broadside direction) for directional antennas.

Hence, time-averaged EIRP can then be determined by combining \bar{P} with $\bar{G}(\theta, \phi)$, according to:

$$\bar{P}_{EIRP}(\theta, \phi, t) = \bar{P}(t) \bar{G}(\theta, \phi, t) \quad (3.1)$$

Since \bar{P} is directly related to the amount of DL traffic, the time-averaged transmit power is expected to increase with the number of users. Simultaneously, more users will result in a larger spread of energy over the antenna Scan Range (SR), given by the pair (θ, ϕ) , where $(\theta = 0^\circ, \phi = 0^\circ)$ corresponds to the broadside beam direction. This leads to a reduction of \bar{G} regarding the peak envelope gain, therefore, \bar{P}_{EIRP} is expected not to increase considerably with the increase in the number of users.

The total transmitted power from the BS is proportional to the RBs share, i.e., the number of RBs scheduled for DL transmission, $N_{RB}^{alloc,DL}$ [CJPT19]. The RBs share can be determined by dividing the number of allocated RBs, N_{RB}^{alloc} , by the total number of RBs available for DL, N_{RB}^{DL} :

$$N_{RB}^{alloc,DL} = \frac{N_{RB}^{alloc}}{N_{RB}^{DL}} \quad (3.2)$$

However, it is necessary to take into account not only the BS utilisation but also the spatial distribution of the power, which also has a substantial influence on EMF exposure. This distribution depends on the beams selected for transmission.

For TDD, beam scheduling can be done by a channel estimate performed by the BS through the reception of a Sounding Reference Signal (SRS) that is continuously being transmitted by the connected users. Through the SRS reception, it is possible to estimate the signal DoA [CJPT19]. Therefore, the actual time-averaged transmit power per beam, \bar{P}_{beam} , measured over the averaging time, T , and normalised to the theoretical maximum, can be given by [CJPT19]:

$$\bar{P}_{beam} = N_{RB}^{alloc,DL} \frac{N_{users}^{beam}}{N_{users}} \quad (3.3)$$

where:

- N_{users}^{beam} : maximum number of users per beam.

\bar{P}_{beam} is usually based on the beam with the highest user density. A user is considered to be scheduled by a beam if the respective DoA is within its vertical and horizontal Half Power Beam Widths (HPBW).

When spectrum is shared between UL and DL (TDD systems), DL's transmission duration as a fraction of the overall one needs to be known. In order to assess DL exposure, the realistic maximum exposure should be proportional to the TDD DL Duty Cycle, given by [TFCT17]:

$$F_{TDD} = \frac{T_{DL,transm}/T_{UL,transm}}{(T_{DL,transm}/T_{UL,transm}) + 1} \quad (3.4)$$

where:

- $T_{DL,transm}$: DL transmission time;
- $T_{UL,transm}$: UL transmission time.

F_{TDD} may assume seven possible configurations in LTE, ranging from 2:3 to 9:1, which corresponds to a range of about 0.4 to 0.93. In [TFCT17] and [CJXG20], 0.75 has been assumed as a reasonable value for NR.

The transmission to all connected users during the averaging time, T , needs to be taken into account, since EMF exposure may vary with the spatial location of the users.

Considering the total average scheduling time per user, T_s , the number of served independent users, N_{users}^T , during the EMF averaging time, can be approximated in terms of the number of simultaneous users served by the system at a specific time instant, N_{users}^{sim} [TFCT17]:

$$N_{users}^T \cong N_{users}^{sim} \frac{T}{T_s} \quad (3.5)$$

where:

- N_{users}^{sim} : number of simultaneous users served by the system at a specific time instant;
- T_s : total average scheduling time per user.

The ratio T/T_s depends on the system usage pattern. Considering a scenario with a periodic download of web pages, where the web page size is exponentially distributed with a mean page size of 3 MB and another scenario based on stream media, both considering a low peak 5G data rate equal to 50 Mbps, one may consider as a realistic conservative approximation $T/T_s \cong 10$ [TFCT17].

In general, it is possible to list the main parameters that have a substantial influence on the temporal variation of \bar{P} and \bar{G} . \bar{P} may change in time, due to:

- the total number of users in the system, hence the number of RBs;
- the service usage duration of each user;
- TDD Downlink Duty Cycle.

while $\bar{G}(\theta, \phi)$ may suffer some changes in time, due to:

- user density distribution (to guarantee coverage and capacity, beam shape adjustment may be necessary, changing $\bar{G}(\theta, \phi)$ in time; the smaller the area to be covered, the greater the gain);
- an increase in traffic usually results in an increase in energy spread; increasing the number of users may lead to an increase in the number of beams to be steered in different directions.

IMT-2020 has defined different test environments for different 5G usage scenarios: an Indoor Hotspot, a Dense Urban and a Rural environment for eMBB and an Urban Macro environment for mMTC and URLLC. Taking into account the goal of this thesis, the most appropriate test scenario to be studied is the dense Urban-eMBB, which simulates an urban environment with high user density and a large amount of user traffic considering pedestrians and users in vehicles in outdoor and outdoor-to-indoor settings. Being an interference-limited scenario, it contemplates overlaying macro-transmission/reception points (TRPs) with or without micro-TRPs, which are typically found in city centres and dense urban areas. The radial coverage in this environment is typically less than 100 m. Table 3.1 contains the IMT-2020 technical performance requirements for DL taking a dense urban eMBB scenario.

Table 3.1. IMT-2020 Technical performance requirements for DL in the context of a dense urban eMBB scenario (based on [ITUR17]).

Performance indicator	Value
Peak data rate	20 Gbps
User experience data rate	100 Mbps
Area traffic capacity	Depends on average spectral efficiency and site density
Supported mobility and normalised data rate	Stationary (0 km/h), pedestrian (0 to 10 km/h), vehicular (up to 30 km/h); 1.12 bps/Hz
Mobility interruption time	0 ms
Bandwidth	≥ 100 MHz

For the eMBB usage scenario, one can define 5 major mobile applications: streaming, computing, gaming, communicating and storage. For a realistic performance assessment, appropriate service usage time durations must be determined. The respective access times for downloading files and average session durations are presented in Table 3.2.

Table 3.2. Access times and average session durations for different downloads and services.

File download/ Service	Access time/ Average session duration	Reference
Video (10 MB)	0.8 s	[Corr20]
Web Browsing	2 to 3 min	[Simi21]
Video Streaming	3 to 15 min	[Stat21]
Film (5 GB)	7 min	[Corr20]
Video Conference	45 to 60 min	[Zoom21], [Skyp21]
Real-time Gaming	79 min	[KDRS15]
Film8K (800 GB)	18 h	[Corr20]

The access times were determined taking 100 Mbps as the average user experience data rate. These access times and average session durations allow one to conclude whether or not it is necessary to determine exposure for lower averaging times.

3.2.2 Temporal Variation of the Reference Level

In order to determine reference levels for exposure taking averaging times lower than 6 min into account, one should use the reference levels for local exposure, integrated over intervals of between 0.5 min and 6 min, presented in Table 2.14. Thus, it is possible to analyse the temporal variation of the incident power density, taking into account the relationship between the power and energy density.

The incident energy density can be derived as the temporal integration of the incident power density during a time interval, t :

$$U_{inc} = C \int S_{inc}(t) dt \quad (3.6)$$

where:

- C : propagation constant.

Hence, the expression for the temporal variation of the power density integrated over intervals between 0.5 min and 6 min, based on the expressions for the incident energy density established in [ICNI20] and presented in Table 2.14, is given by:

$$S_{inc}(t) = \frac{C}{\sqrt{t}} \quad (3.7)$$

Since the S_{inc} reference level for local exposure to EMFs from 2 GHz to 6 GHz, averaged over 6 min, is equal to 40 W/m^2 , [ICNI20], the propagation constant is equal to $40\sqrt{360}$, therefore, the time variance of the S_{inc} reference value, over $t \in]0.5, 6[\text{ min}$, is given by, Figure 3.2:

$$S_{inc}(t_{[s]}) = \frac{40\sqrt{360}}{\sqrt{t_{[s]}}} \quad (3.8)$$

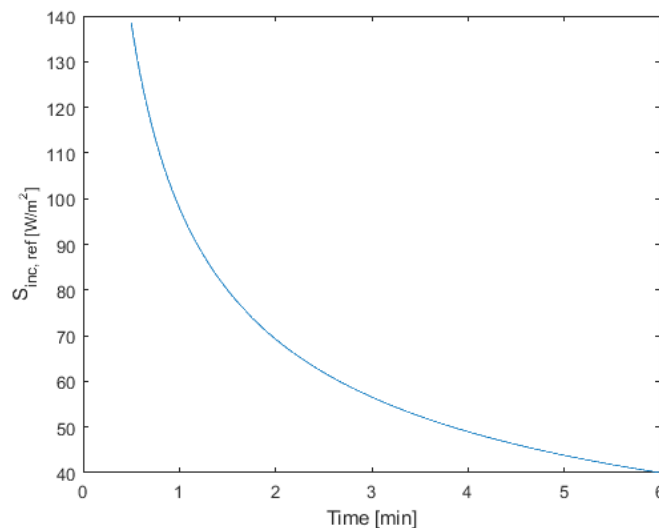


Figure 3.2. Incident Power Density, S_{inc} , reference level for exposure, integrated over time intervals between 0.5 min and 6 min, from 2 GHz to 6 GHz (unperturbed RMS values).

3.2.3 Beamforming Behaviour

A planar array is assumed to have $N \times M$ antennas, where N is the number of columns M is the number of rows. The elements composing the array consist of two dipoles with orthogonal polarisation (crossed-dipoles) in order to achieve polarisation diversity, since two orthogonal polarisations generate almost uncorrelated signals in a scattering environment. In Figure 3.3, a planar array is represented. The antenna elements are characterised by points in three-dimensional (3D) space with x, y, z coordinates, where the planar antenna is placed on the yOz plane ($x = 0$).

Depending on element spacing and steered angle, an array might generate additional large sidelobes, known as grating lobes. According to [COMM21], 0.5λ spacing between elements is enough to guarantee protection against possible grating lobes. In general, when the array spacing is less than or equal to 0.5λ , only the main lobe exists, with no other grating lobes.

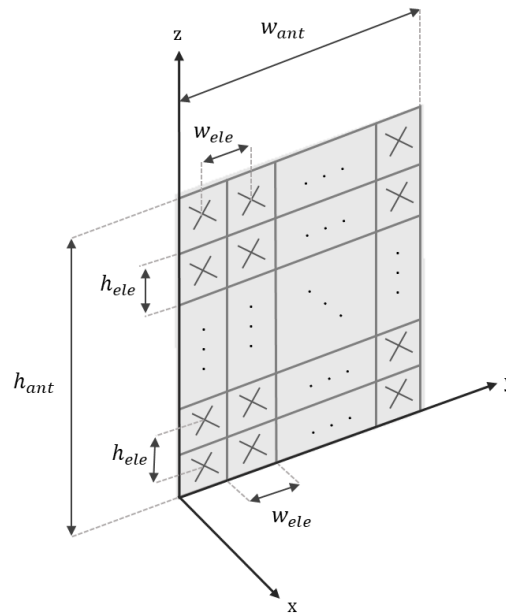


Figure 3.3. Representation of a planar array with crossed-dipole elements.

The azimuth angle, ϕ , and the elevation angle, θ , may vary 180° . Since sectorisation should be considered, ϕ will vary according to the order of sectorisation. Taking the most common topology (three sectors), beams will be able to scan horizontally with an azimuth angle that can vary approximately 120° .

Starting by defining the geometry of the problem, the point of observation is at a distance r_{obs} from the antenna and changes position according to the user's location. As there can be several users to be served simultaneously, there can be several observation points. Based on [Mour20], it is possible to assume, for a simplified analysis, that each element occupies a rectangle with a width w_{ele} and height h_{ele} as follows:

$$h_{ele} = \frac{h_{ant}}{N_{V,el}} \quad (3.9)$$

$$w_{ele} = \frac{w_{ant}}{N_{H,el}} \quad (3.10)$$

where:

- h_{ant} : height of the antenna planar array;
- w_{ant} : width of the antenna planar array;
- $N_{ele,V}$: number of vertical elements of the planar array;
- $N_{ele,H}$: number of horizontal elements of the planar array.

Assuming also that each element is placed at the centre of each rectangle, the y and z coordinates of the element placed in the m^{th} line and n^{th} column can be expressed, respectively, as:

$$y_{mn} = \frac{w_{ele}}{2} + (n - 1) w_{ele} \quad (3.11)$$

$$z_{mn} = \frac{h_{ele}}{2} + (m - 1) h_{ele} \quad (3.12)$$

Since the first line of elements starts at the bottom of the antenna, increasing from bottom to top, the distance from an element to the observation point can be given by:

$$r_{mn,obs} = \sqrt{r_{obs}^2 + (y_{obs} - y_{mn})^2 + (z_{obs} - z_{mn})^2} \quad (3.13)$$

where:

- y_{obs} : the y coordinate of the observation point;
- z_{obs} : the z coordinate of the observation point.

Based on [Skol90] and considering an element spacing of 0.5λ , the 3 dB beamwidth can be related to the number of radiating elements by:

$$\theta_B \cong \frac{100}{\sqrt{N_{ele}}} \quad (3.14)$$

where:

- θ_B : 3 dB beamwidth in degrees.

The number of beams that can actually be generated and fitted into a sphere can be given by [Skol90]:

$$N_{beams} \cong \frac{\pi}{2} N_{ele} \quad (3.15)$$

Assuming that the total power is equally distributed over all elements, the power of each element is:

$$P_{ele} = \frac{P_{in}}{N_{ele}} = \frac{P_{in}}{N_{ele,H} N_{ele,V}} \quad (3.16)$$

where:

- P_{in} : antenna input power.

The gain of each element can be given by:

$$G_{ele}(\theta, \phi) \cong \frac{G_M f_{ele,V}(\theta) f_{ele,H}(\phi)}{N_{ele}} \quad (3.17)$$

where:

- $f_{ele,V}(\theta)$: element radiation pattern in the vertical plane;
- $f_{ele,H}(\phi)$: element radiation pattern in the horizontal plane.

For a dipole, the horizontal radiation pattern is omnidirectional, hence, the normalised horizontal radiation pattern is equal to unity. However, the vertical radiation pattern depends on the elevation angle and the length of the dipole relative to the wavelength [Silv20], therefore, based on (2.8), the element vertical radiation pattern can be given by:

$$f_{ele,V}(\theta) = \left| \frac{\cos\left[\frac{\pi}{2}\cos(\theta)\right] - \cos\left(\frac{\pi}{2}\right)}{\sin(\theta)} \right|^2 \quad (3.18)$$

Since the antenna elements consist of crossed-dipoles, i.e., two dipoles inclined at $\pm 45^\circ$ (90° out of phase), the changes in pattern behaviour for this particular case should be taken into account. The correspondent change in pattern is represented in Figure 3.4.

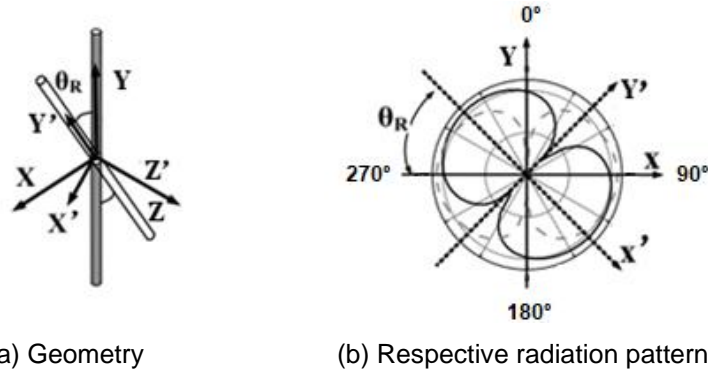


Figure 3.4. Half-wavelength dipole with a rotation angle equal to 0° and 45° (extracted from [ZhTC15]).

The individual mMIMO beam gain can be asymptotically given by:

$$G_{mMIMO}^{beam} = G_{ele} + 10 \log_{10} N_{array} \quad (3.19)$$

where:

- N_{array} : Number of antenna elements in the considered array.

The AAUxxxxw antenna gain patterns are represented in Figure 3.5, where the area outlined with the blue line corresponds to the maximum beam coverage scope, the one in red to the minimum beam coverage scope and the one in green to the area of actual operation of the antenna.

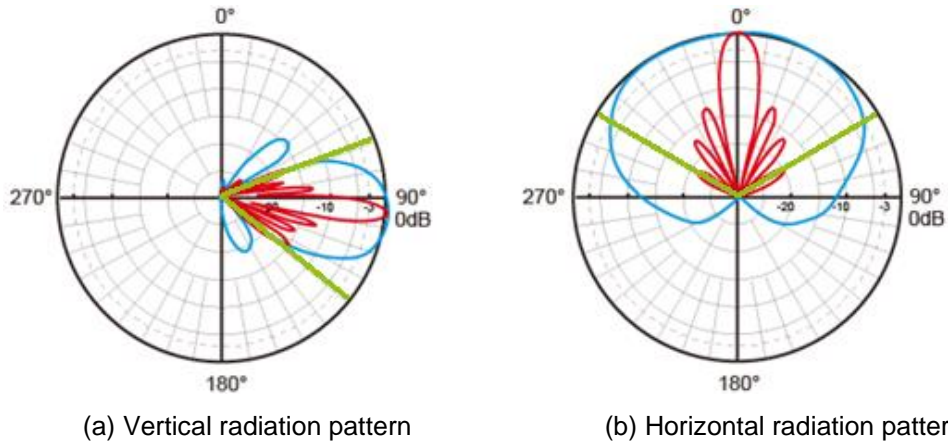


Figure 3.5. AAUxxxxw radiation patterns in a macro coverage scenario (adapted from [HUAW21b]).

Taking the maximum beam coverage scope of the radiation patterns into account, the gain of the

antenna can be determined for any direction using (2.15) along with:

$$f_{\theta}(\theta) = \left| \frac{\cos\left[\frac{\pi}{2}\cos(\theta)\right] - \cos\left(\frac{\pi}{2}\right)}{\sin(\theta)} \right|^2 \frac{\sin(N_{ele}\Psi/2)}{N_{ele}\sin(\Psi/2)} \quad (3.20)$$

$$f_{\phi}(\phi) = \frac{1 + \cos(\phi)}{2} \quad (3.21)$$

3.3 CST Simulation Software

This section contains a brief introduction to the CST simulation software, along with a more detailed description of its main features and specifications. A description of the different simulations performed, as well as the obtained results, is presented.

3.3.1 Software Features and Operation

CST Studio Suite is a high-performance 3D electromagnetic analysis software for designing, analysing, and optimising electromagnetic components and systems [Dass21a].

CST Studio Suite for High Frequency Simulation, in particular, is adequate for electromagnetic analysis and design in the high frequency range, simplifying the design of the structure by providing a powerful graphical solid modelling front end, based on the ACIS modelling kernel. After the design of the model, a fully automatic meshing procedure is applied before the simulation, followed by the processing and visualisation of results.

When launching CST Studio Suite, it is possible to configure a project template where the required basic settings can be set. It is necessary to identify and define the application type that best suits the requirements of the system to be designed and simulated.

For this thesis, one should choose Microwaves & RF & Optical as the application area and Antennas as the workflow, selecting Wire as the type of antenna. Later, one must choose a recommended solver for the selected workflow, which in this case should be the Time Domain. These solvers offer the largest simulation flexibility, while being very efficient for high frequency applications, such as the case under study. Furthermore, since the goal is to simulate a planar antenna array (considerably larger than the unit cell), the Frequency Domain solver, based on the Finite Element Method (FEM), is not the most adequate, since the numerical requirements scale exponentially with the size of the problem.

The software offers two different possible solvers of this type: the Transient solver, based on the Finite Integration Technique (FIT) and the Transmission-Line Matrix (TLM) method, both using a hexahedral mesh. These solvers simulate the EMF behaviour, showing the broadband frequency-domain effects through S-parameters. According to [Dass19], for the case under study, the most adequate solver is the Transient one. Unlike FEM, the numerical requirements of FIT scale linearly, i.e., the simulation time

increases in the same proportion as the number of mesh cells, allowing for the simulation of larger problems using fewer computational resources in a shorter time.

The hexahedral mesh is constituted by small, variable size cuboids, the grid cells. Each cell represents a small volume in space, having a specific electric, \mathbf{E} , and magnetic, \mathbf{H} , fields behaviour. The behaviour of these cells is based on the Finite Difference Time Domain (FDTD) method, where in each cell, \mathbf{E} and \mathbf{H} are spatially organised so that each element of \mathbf{E} is surrounded by four elements of \mathbf{H} and each element of \mathbf{H} is surrounded by four elements of \mathbf{E} , discretising Maxwell's equations in space, Figure 3.6.

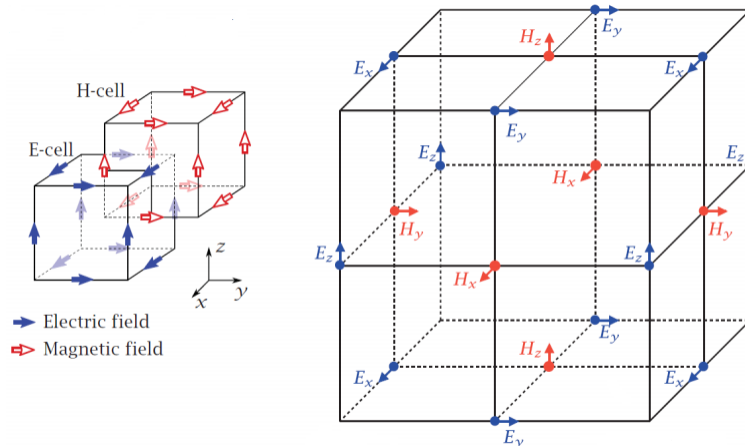


Figure 3.6. Representation of a FDTD cell (adapted from [Laak15]).

The greater the number of cells used for discretisation, the more accurate the field gradients are captured. However, one must note that by increasing the number of cells, the simulation time may also increase, hence the importance of using a well-balanced mesh, which provides a good compromise between those two important factors. The total number of mesh cells cannot be controlled directly, being a result of the min/max cell size, computing the number of mesh cells required to discretise the computational volume.

The definition of the mesh is another very important aspect to take into consideration, since the quality and type of mesh will affect simulation time and accuracy. There are two different ways of defining a hexahedral mesh without doing it manually, which is quite discouraged in the user guide, since it requires very high knowledge of the software tool and it is not necessary in the vast majority of the cases.

When designing the structure, CST automatically generates a mesh adapted to the design, the Automatic Mesh Generation with an Expert System. There is also the Adaptive Mesh Refinement that discovers the best mesh by a loop, where an initial mesh is created and will be gradually redefined until the solution converges to some user's predefined convergence criteria.

In order to globally control the mesh, some settings need to be defined [Dass21b]:

- maximum cell: it defines the largest allowed cell size in the calculation domain. For high-frequency electromagnetic simulations, the maximum cell size is often defined with respect to the wavelength in order to provide an optimal spatial sampling rate for the fields inside the structure. The highest frequency of interest determines the smallest wavelength. The maximum cell size can be defined separately inside the model bounding box (near to model) and outside

the model bounding box (far from model). There are two possibilities to provide this wavelength-based definition of the maximum cell size.

- cells per wavelength: it defines the upper limit of the cell size with respect to the wavelength while also setting the spatial sampling rate for the signals inside the structure. It has a strong influence on both the quality of the results and the calculation time. Increasing this number leads to higher accuracy, but also increases the total calculation time.
- minimum cell: it can be used in order to avoid an overrefinement due to small geometric details, such as thin regions or gaps. The smallest mesh step influences the time step width and thus the overall simulation speed.
- fraction of maximum cell near to model: the minimum allowed cell size is determined by dividing the maximum cell size near to model by this number.

Another important aspect to take into account when simulating a structure in CST is the boundary conditions, since, from a computational perspective, all simulations require a finite expansion. In CST, a rectangular grid system is used, being defined by minimum and maximum positions $(x_{min}, x_{max}, y_{min}, y_{max}, z_{min}, z_{max})$ in each coordinate direction in order to identify the six boundary surfaces.

For high frequency simulations, there are seven possible boundary conditions:

- electric: operates as a Perfect Electric Conductor (PEC), so all the tangential \mathbf{E} and the normal \mathbf{H} fields are set to zero;
- magnetic: operates like a Perfect Magnetic Conductor (PMC), so all the tangential \mathbf{H} and the normal \mathbf{E} fields are set to zero;
- open (PLM): extends the touching geometry virtually to infinity by using a Perfectly Matched Layer (PML) boundary, therefore, waves pass this boundary with minimal reflection;
- open (add space): similar to Open (PML), except that it adds some extra space for far-field calculation, being recommended for antenna problems, since it automatically adapts the centre frequency of the working bandwidth;
- periodic: connects two opposite boundaries with a definable phase shift, so that the calculation domain is simulated to be periodically expanded in the corresponding direction, thus, changing one boundary to this type will automatically change the opposite one;
- conducting wall: acts as a lossy metal material conducting wall;
- unit cell: similar to the periodic boundary, where a two-dimensional periodicity other than the direction of the coordinate axes may be set [Dass21b].

3.3.2 Antenna Unit Simulation

The first step to the simulation of the planar array antenna is the dimension of its unit element, a half-wavelength dipole. The representation of a half-wavelength dipole antenna and its respective dimensions are presented in Figure 3.7.

The imaginary part of the impedance of a linear dipole can be eliminated by making the total length of the wire antenna, L , slightly less than an integral number of half-wavelengths or slightly greater than an

integral number of wavelengths, with the amount of reduction or increase in length as a function of the wire radius [Bala16].

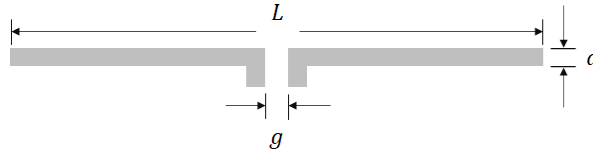


Figure 3.7. Representation of a half-wavelength dipole antenna and its dimensions.

The resonance length, l_{res} , is given by:

$$l_{res} = 0.48 \lambda F_{ress} \quad (3.22)$$

where:

- F_{ress} : resonance factor:

$$F_{ress} = \frac{L/2 a}{1 + L/2 a} \quad (3.23)$$

where:

- a : radius of the wire antenna.

Matching (3.22) and (3.23), for a given radius, it is possible to obtain an initial length for the half-wavelength dipole:

$$L = \frac{0.48 \lambda}{2 a} \quad (3.24)$$

For $a = 0.5$ mm, a length of 39.97 mm is obtained. Considering 3.6 GHz as the resonant frequency, it is possible to determine the initial dimensions of the half-wavelength dipole. The dipole, composed of a PEC material, has the dimensions listed in Table 3.3.

Table 3.3. Dimensions of the half-wavelength dipole antenna.

Half-wavelength dipole measures [mm]	
Wavelength, λ	83.28
Radius, a	0.50
Length, L	39.97
Feed gap, g ($L/200$)	0.20

The corresponding CST design of the dimensioned half-wavelength dipole is presented in Figure 3.8.

Setting the frequency between 3.45 GHz and 3.7 GHz, the half-wavelength dipole is fed with a 50 Ω impedance and an input power of 1 W. Considering the mesh options, the hexahedral mesh type is chosen, with an accuracy of -40 dB. As chosen mesh properties, one has 15 Cells per Wavelength Near to Model and Far from Model, and 20 as the Fraction of Maximum Cell Near to Model, resulting in a total of 113 256 mesh cells, Figure 3.9. The goal is always to obtain the best trade-off between simulation speed and accuracy.

Since the antenna radiates into free-space, open boundary conditions must be used. However, for far-field calculations, open boundary conditions need to consider some space between the antenna and the

boundary planes for optimum performance and accurate calculations. The Open (add space) option automatically estimates the required space. Therefore, this option was chosen for all limits.



Figure 3.8. Design of the slanted half-wavelength dipole antenna in CST, placed in the xOy plane.

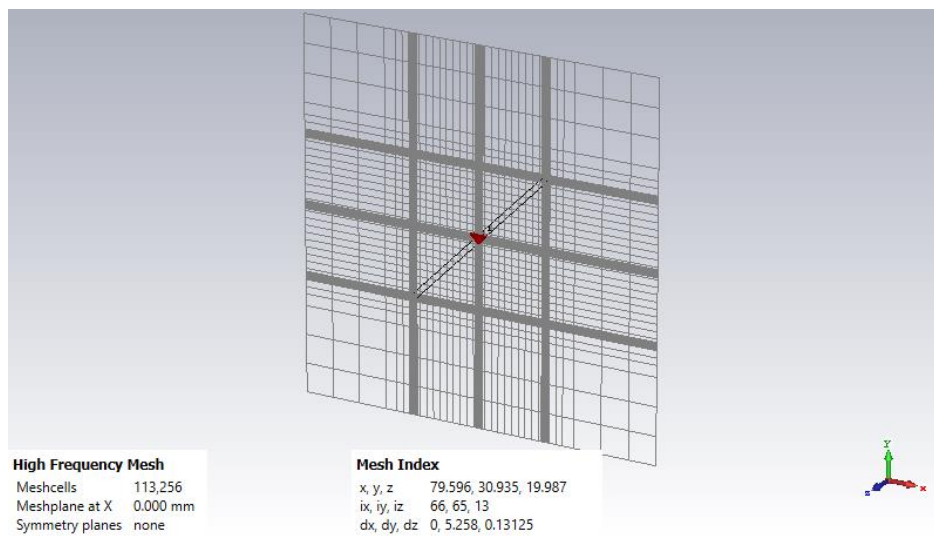


Figure 3.9. Mesh representation of the 45° slanted half-wavelength dipole antenna, in xOy plane.

All simulations performed were executed using a laptop equipped with an AMD Ryzen 5 2500U, Radeon Vega Mobile Gfx CPU, 2 GHz of clock speed and 20 GB of RAM.

It is possible to adjust the initial length of the dipole, presented in Table 3.3, in order to guarantee the location of the S_{11} parameter's minimum at 3.6 GHz. CST offers a powerful built-in optimiser feature for this type of parametric optimisation. An optimised dipole length, $L^{opt} = 36.14$ mm, was found and the respective S_{11} parameter is represented in Figure 3.10.

For far-field calculations, appropriate monitors or probes should be chosen. After running the simulation, in the Far-field Plot Mode inside the Far-field Properties menu, it is possible to see a reference distance equal to 1 m and a far-field approximation. The reference distance can be seen as the radius of the virtual sphere for which the far-field is calculated. It is possible to change the distance and also disable the far-field approximation. However, changing this distance is only possible for the electric field, since there is a matter of the minimum distance of the bounding box [Dass21b].

If the Near-field Calculation checkbox in the Far-field Monitor is turned on, the near-fields on the monitor box surface are kept and combined in later post-processing, which is required in some cases, such as the removal of the far-field approximation.

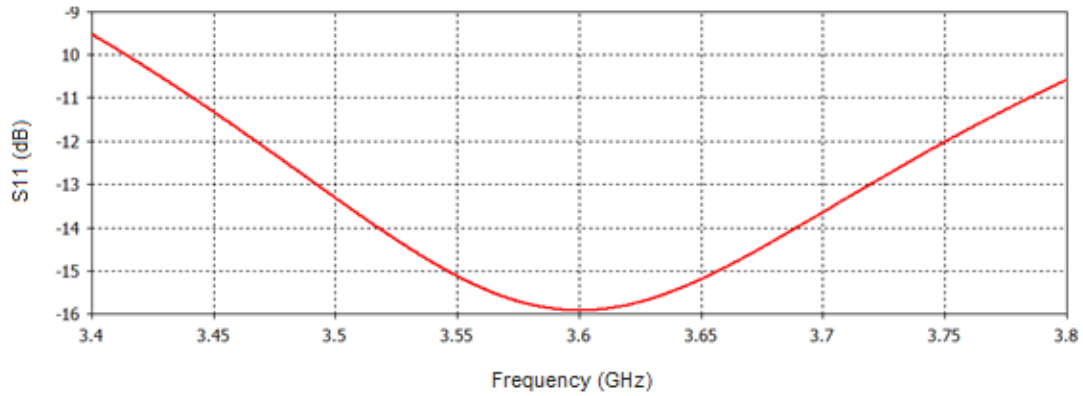


Figure 3.10. S_{11} parameter, as a function of frequency, of the half-wavelength dipole.

The 3D and two-dimensional (2D) Electric Field Pattern (E-pattern) and gain far-field results for the slanted dipole are represented in Figures 3.11, 3.12, 3.13, 3.14 and 3.15. In the 2D representations, while the area outlined with red represents the radiation pattern, the light blue line corresponds to the 3 dB beamwidth and the dark blue one to the direction of the main lobe, i.e., of maximum radiation.

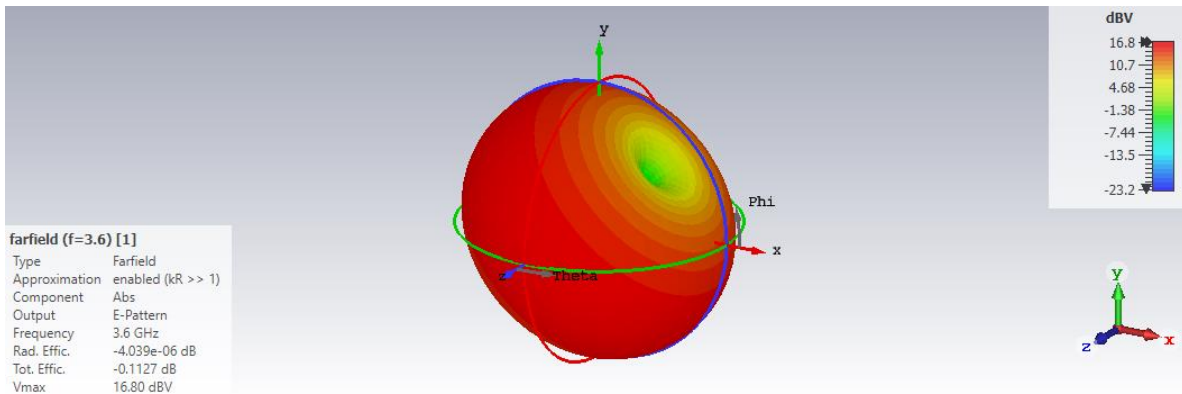


Figure 3.11. 3D E-pattern pattern of the 45° slanted dipole operating at 3.6 GHz.

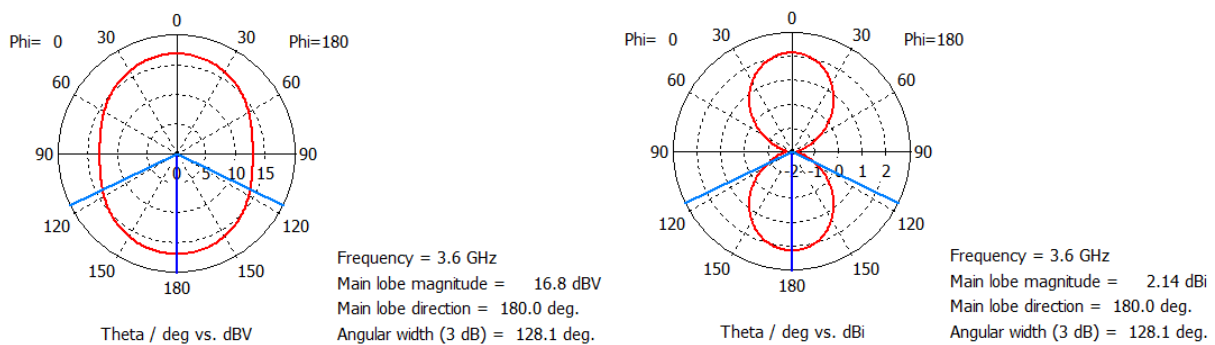


Figure 3.12. 2D far-field cut ($\phi = 0^\circ$) of the E- and gain patterns for the 45° slanted dipole.

3.3.3 Antenna Full Array Simulation

If the array would consist of an infinite number of identical elements, the study of the unit cell alone would be enough. However, the size of the planar array is finite, hence it is necessary to take into consideration some non-periodic effects, such as the edge effects and other physical realities. Hence,

a simulation of the full array must be performed.

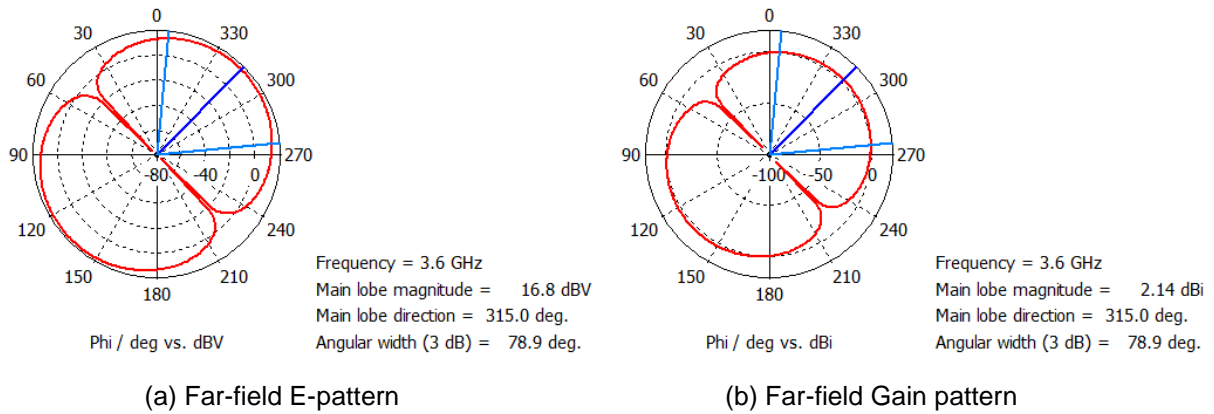


Figure 3.13. 2D far-field cut ($\theta = 90^\circ$) of the E- and gain patterns for the 45° slanted dipole.

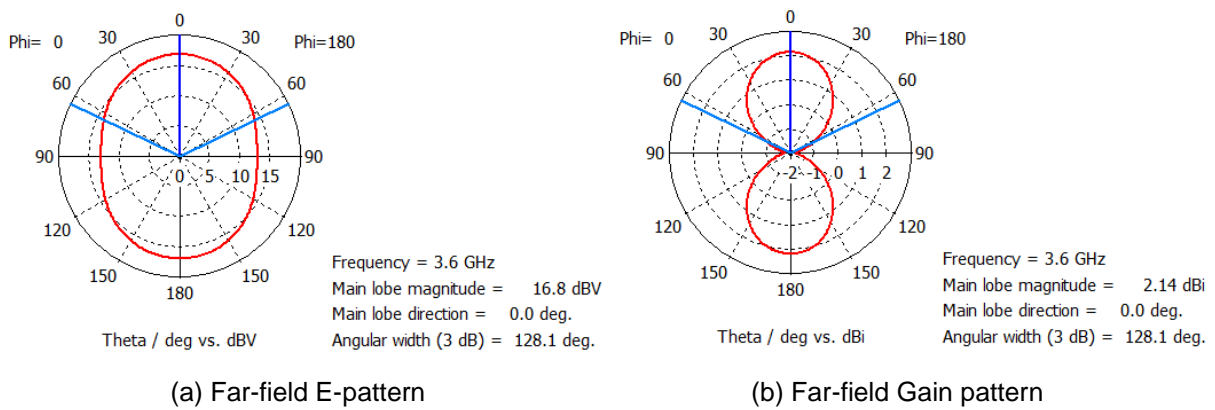


Figure 3.14. 2D far-field cut ($\phi = 0^\circ$) of the E- and gain patterns for the -45° slanted dipole.

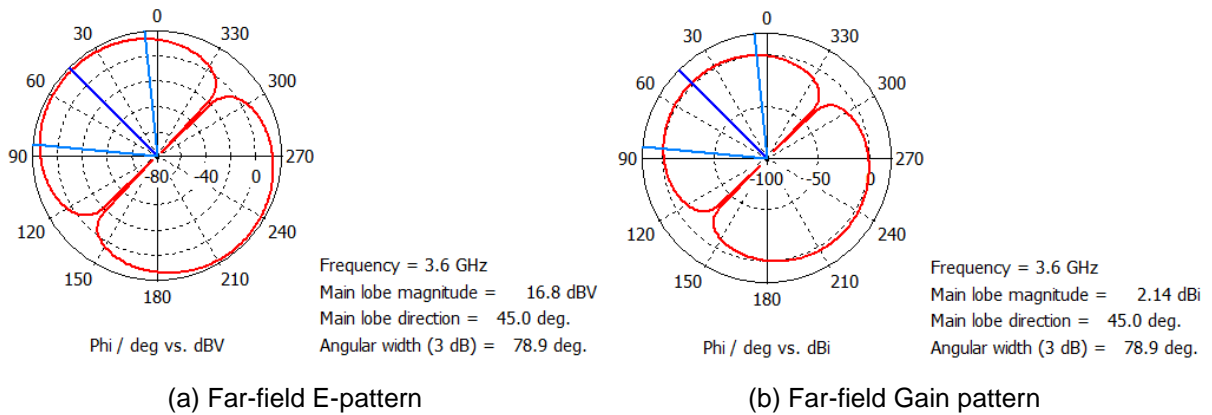


Figure 3.15. 2D far-field cut ($\theta = 90^\circ$) of the E- and gain patterns for the -45° slanted dipole.

Taking the specifications of the antenna into account, it is possible to define the desired planar array using the CST Array task. This tool uses the unit cell geometry along with a definition of the pretended layout to efficiently design the full array geometry, setting up the port excitations according to the choice of the user. When creating the planar array in CST, it is also possible to enable and disable some elements by using the Element Type tool, where an element can be set as Active, Passive or Empty.

By considering the elements equally spaced along the correspondent dimensions of the antenna, it is possible to approximately determine the horizontal and vertical distances between elements, d_{ele}^H and

d_{ele}^V , given, respectively, by:

$$d_{ele}^H = 0.53 \lambda \quad (3.25)$$

$$d_{ele}^V = 0.67 \lambda \quad (3.26)$$

A PEC material ground plane with the dimensions of the planar array antenna must be added at a distance $\lambda/4$ from the antenna elements [Bala16]. The boundaries should be fixed to Open (add space) for all limits, except for the z_{min} which should be settled as Electric. One should note that, when adding the ground plane, the reflection coefficient will obviously change, however, for the scope of this thesis, this behaviour does not significantly affect the intended results. A design of the full planar array antenna is presented in Figure 3.16.

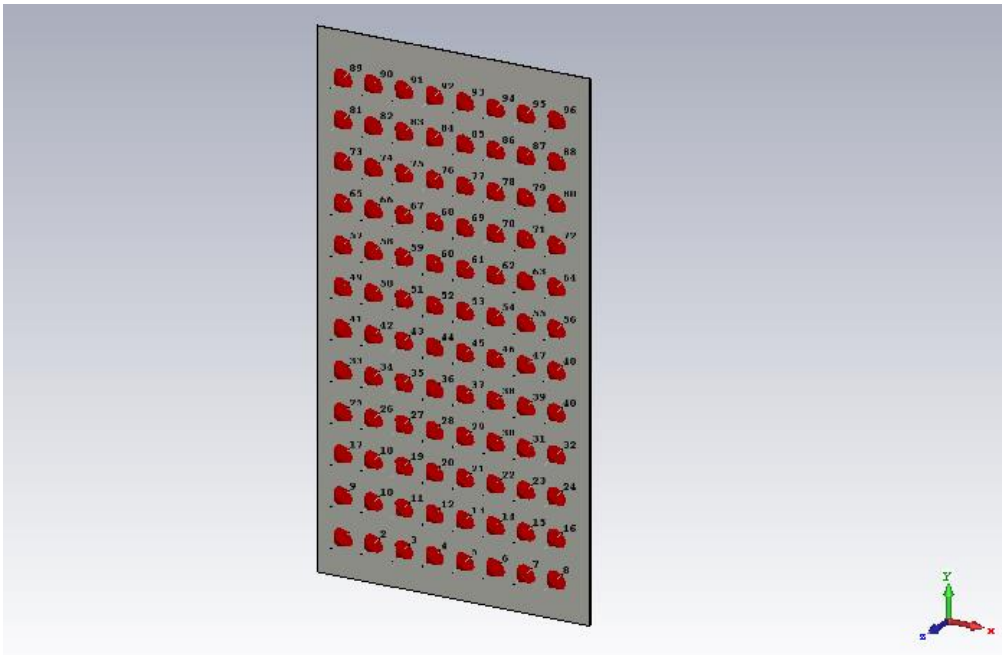


Figure 3.16. Design of the 8×12 planar array in CST, placed in the xOy plane.

There are two ways to excite the planar array. One can individually excite each port, obtaining a full S-matrix, which is considered to be a flexible approach, since it allows one to experiment more in post-processing. However, from the perspective of a transient analysis, it would mean that the ports would be excited and simulated in series, increasing the simulation time. Another option is to simultaneously excite all of the elements, which would not result in significant S-parameters as it does not follow the required conditions. However, for the scope of this thesis, S-parameters are not of great relevance, making the latter the best choice, since it reduces the simulation time. The previous simulation settings were used to simulate the 8×12 planar array.

The 3D and 2D E-pattern and gain far-field results for the AAUxxxxw antenna are represented in Figures 3.17, 3.18 and 3.19, respectively. In the 2D representations, while the area outlined with red represents the radiation pattern, the light blue line corresponds to the 3 dB beamwidth, the green line to the -3 dB mark and the dark blue line to the direction of the main lobe, i.e., of maximum radiation.

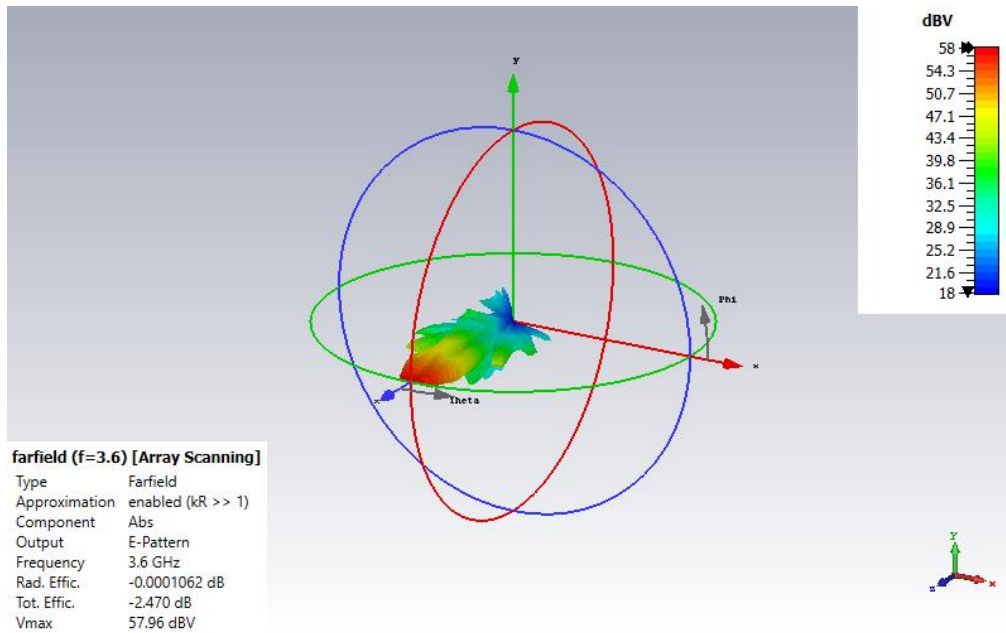


Figure 3.17. 3D 8×12 planar array E-pattern with $(\theta = 0^\circ, \phi = 0^\circ)$.

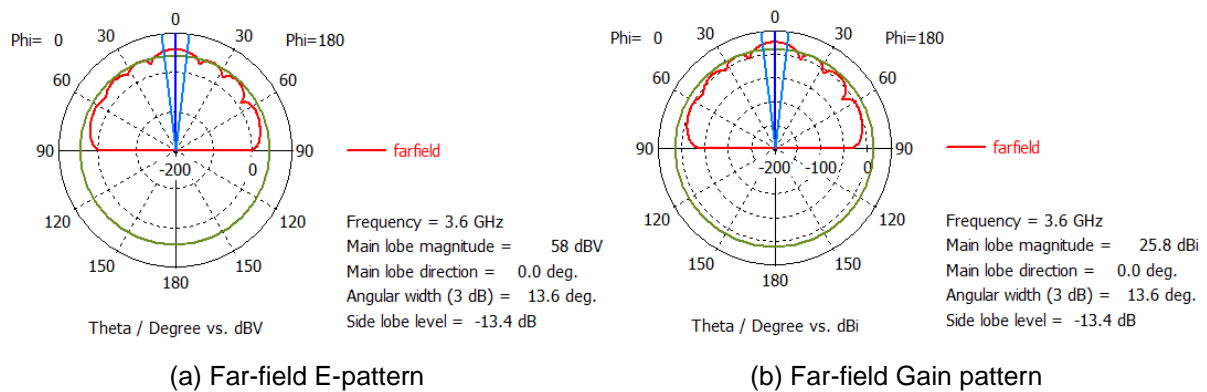


Figure 3.18. 2D far-field cut ($\phi = 0^\circ$) of the E- and gain patterns for the 8×12 planar array.

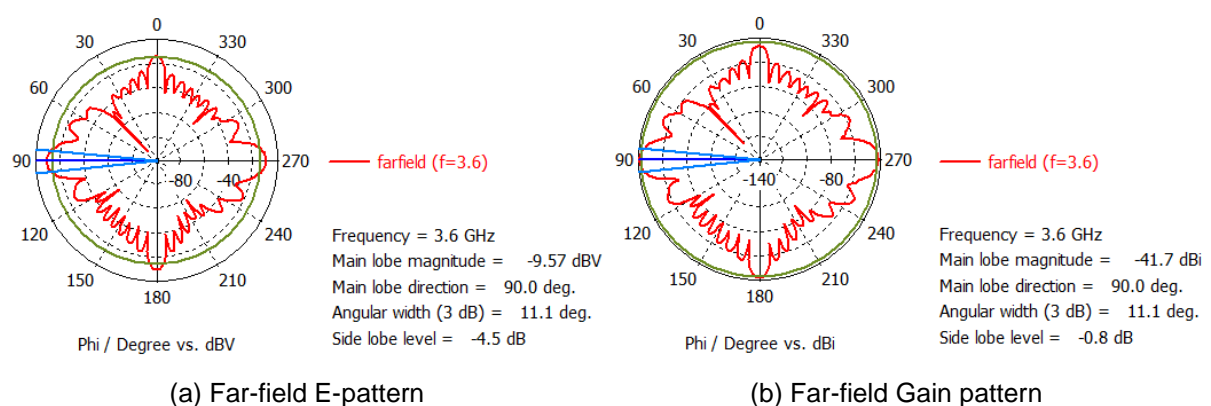


Figure 3.19. 2D far-field cut ($\theta = 90^\circ$) of the E- and gain patterns for the 8×12 planar array.

In CST, there are two ways to define the direction of interest of the beam. By default, the beam will assume the broadside beam direction, where $(\theta = 0^\circ, \phi = 0^\circ)$. One can define the elevation and azimuth angles in the Parameter List: in the array file, two parameters are created by the system, under the name PAA_FA_SCANTHETA and PAA_FA_SCANPHI, respectively. By assigning values to these

parameters, one can change the direction of the beam. By default, the x , y and z axes and spherical coordinate system are defined. In the Post-processing menu, one can define the axis and coordinate system type.

Another option is to assign a different phase to each feed element. Considering the amplitude of excitation equal to unity, the array factor of a $N \times M$ planar array placed in the xOy plane ($z = 0$) can be given by [Bala16]:

$$F_{aa} = F_{aa_x} F_{aa_y} = \sum_{n=1}^N e^{-j(n-1)(kd_x \sin(\theta_d) \cos(\phi_d) + \beta_x)} \times \sum_{m=1}^M e^{-j(m-1)(kd_y \sin(\theta_d) \sin(\phi_d) + \beta_y)} \quad (3.27)$$

where:

- $F_{aa_{x,y}}$: Antenna array factor of an array placed in the x, y -axis;
- $d_{x,y}$: location of the feeds at each element in respect to the x, y -axis, referenced to the initial element in the lower left corner of the array;
- θ_d : elevation angle corresponding to the desired direction for the beam focus;
- ϕ_d : elevation angle corresponding to the desired direction for the beam focus.

β_x and β_y represent the phase excitation for an element in the x - and y -axes, respectively:

$$\beta_{x,y} = -k_{[\text{rad/m}]} d_{x,y[\text{m}]} \sin(\theta_d) \begin{cases} \cos(\phi_d), \beta_x \\ \sin(\phi_d), \beta_y \end{cases} \quad (3.28)$$

therefore, the phase excitation for any element located in the planar array can be given by:

$$\beta_{x,y} = -k_{[\text{rad/m}]} \sin(\theta_d) [d_{x[\text{m}]} \cos(\phi_d) + d_{y[\text{m}]} \sin(\phi_d)] \quad (3.29)$$

While for both methods the results are the same, the former turns out to be more time-efficient. The 3D and 2D E-pattern and gain far-field results for the AAUxxxxw antenna with ($\theta = 45^\circ$, $\phi = 45^\circ$) are represented in Figures 3.20, 3.21 and 3.22, respectively.

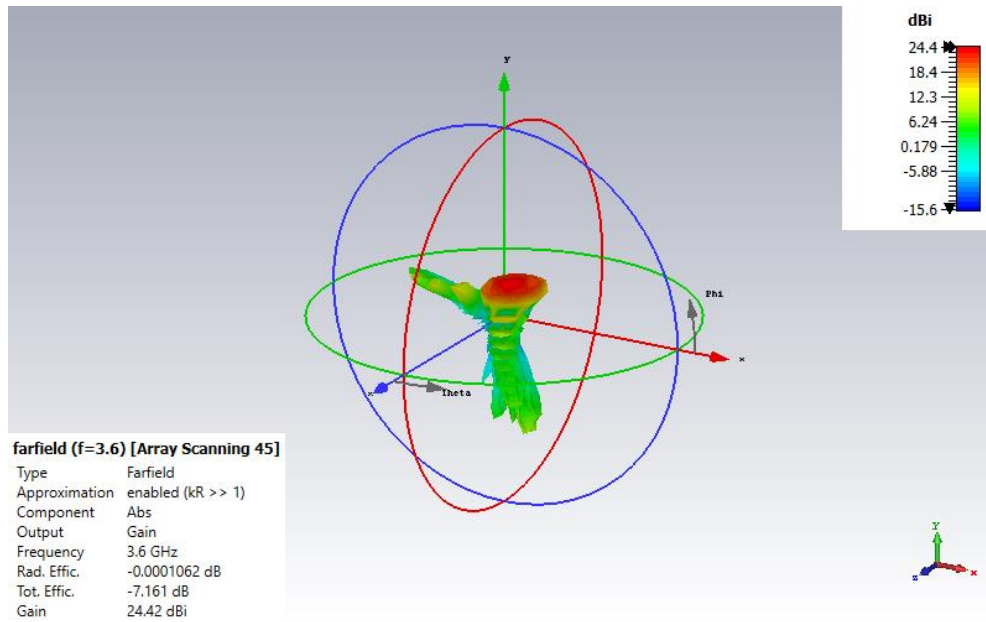


Figure 3.20. 3D 8×12 planar array E-pattern with ($\theta = 45^\circ$, $\phi = 45^\circ$).

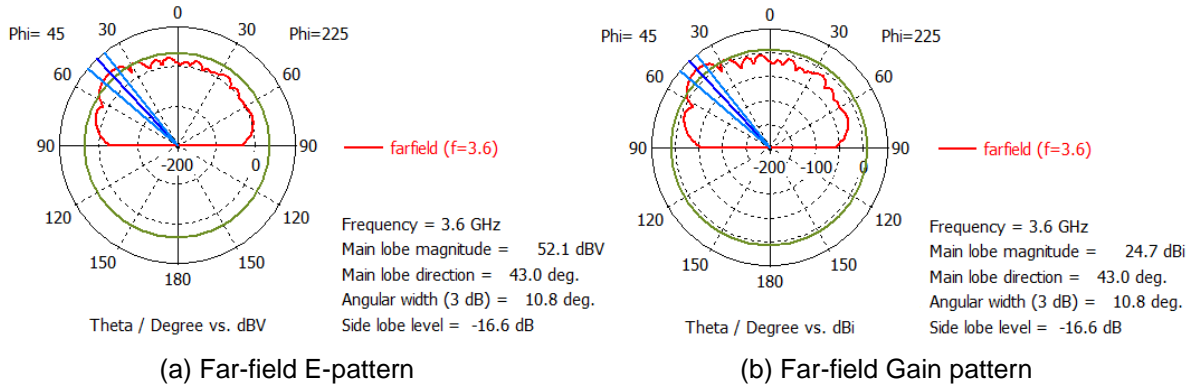


Figure 3.21. 2D far-field cut ($\phi = 45^\circ$) of the E- and gain patterns for the 8×12 planar array.

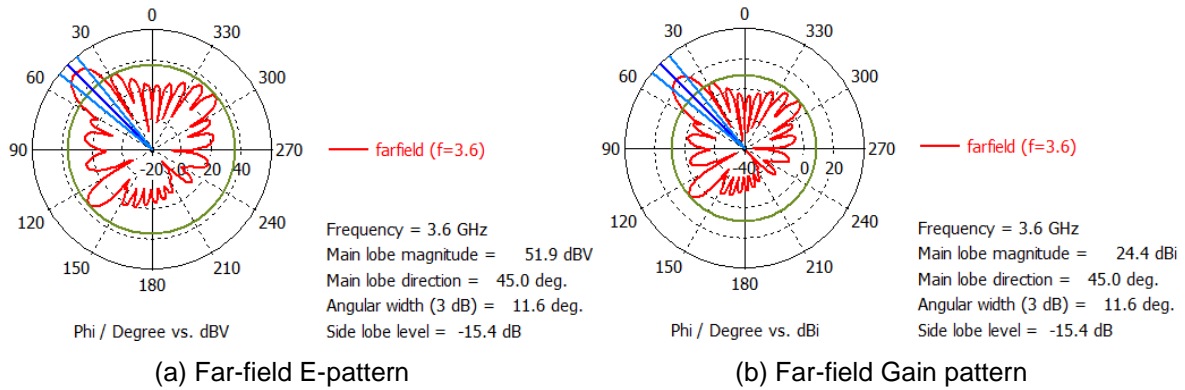


Figure 3.22. 2D far-field cut ($\theta = 45^\circ$) of the E- and gain patterns for the 8×12 planar array.

3.3.4 Near-field Results

The limit distance between the reactive near-field and radiating near-field is given by (2.16), assuming the value of approximately 1.62 m. Considering the largest dimension of the antenna, D , equal to the diagonal of the planar phased array, one can obtain a crossing limit distance between the radiating near-field region and the far-field region, given by (2.17), equal to approximately 16.54 m.

Given the goal of these experiments, one must focus on the near-field results between approximately 1.62 m and 16.54 m in order to determine whether the behaviour of the electric field in this region follows the expected theoretical behaviour, i.e., varies with distance according to [Bala16]:

$$E \propto \frac{C_2[m]}{d_t^2[m]} + \frac{C_1}{d_t[m]} + C_0[m^{-1}] \quad (3.30)$$

where:

- C_2, C_1, C_0 : fit coefficients.

In order to obtain the near-field results, one can use Field Probes or Field Monitors. The first option is more appropriate when one is interested in determining the field for different frequencies. Since that is not the case, Field Monitors must be used instead. Taking these monitors, there are three different ways to analyse the results. A field can be evaluated using arbitrary coordinates, a plane, or a curve. The most appropriate option for the case under study is the latter. Therefore, one must draw a line along the desired direction, as represented in Figure 3.23 and run the simulation.

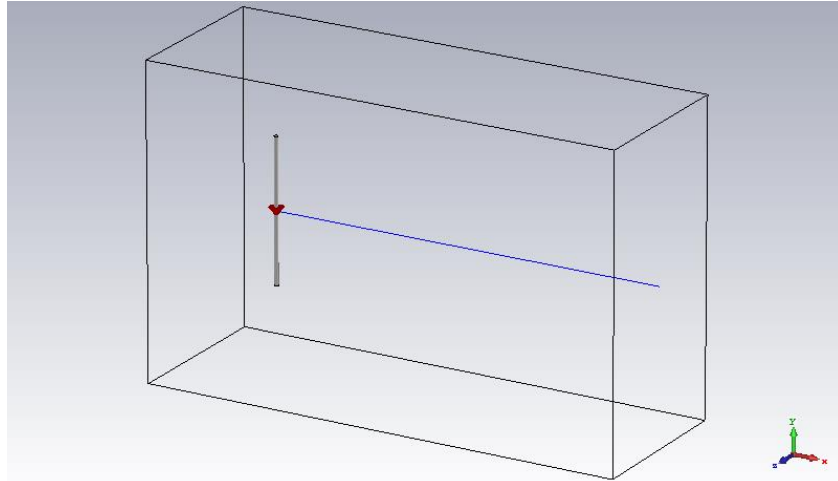


Figure 3.23. CST design using Evaluate Field on Curve tool.

Since, by using this method, the calculation domain will increase significantly, the mesh properties and accuracy must be adjusted in order to allow the simulations to run with the available CPU and RAM. As chosen mesh properties, one has 10 Cells per Wavelength for Near to Model and Far from Model and 60 as the Fraction of Maximum Cell Near to Model. The latter guarantees that the excitation ports are located along the mesh edges.

The accuracy is set at -30 dB, which is considered to be a moderate accuracy level. If there is still a certain amount of energy left in the structure when the solver stops, a truncation error will appear. This may cause some ripples in the S-parameter curves but does not shift the frequency of the pole. Because the location of the minimum is all that matters for the purpose of this thesis, a larger truncation error is acceptable [Dass19], [Dass21b]. After the simulation is finished, the results appear in the 2D/3D Results menu. By using the Evaluate Field on Curve option, it is possible to obtain, among others, the real and imaginary parts of the field, as well as the respective magnitude.

By simulating a vertical half-wavelength dipole with the properties and dimensions of the single element dipole of the AAUxxxxw to assess the chosen simulation method, it was possible to obtain a representation of the electric field strength as a function of distance, presented in Figure 3.24.

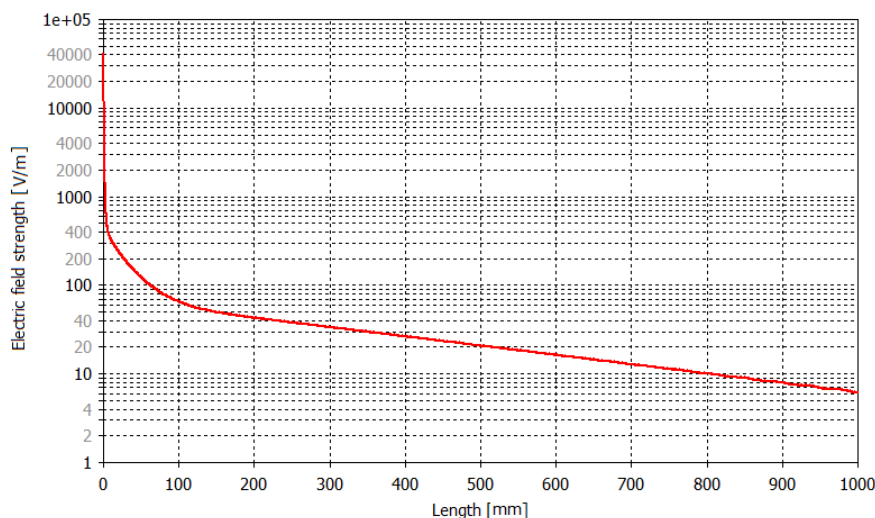


Figure 3.24. Dipole electric field strength as a function of distance.

By using (2.16) and (2.17) and considering the optimised dipole length, $L^{opt} = 36.14$ mm, one is able to determine approximations for the R_{rnf} and R_{ff} values for the half-wavelength dipole, obtaining $R_{rnf} = 14.76$ mm and $R_{ff} = 31.37$ mm. Analysing the behaviour of the field, it is possible to notice that close to the far-field region, the electric field starts to decay inversely proportional to the distance, i.e., proportionally to $1/d$, as expected, Figure 3.25.

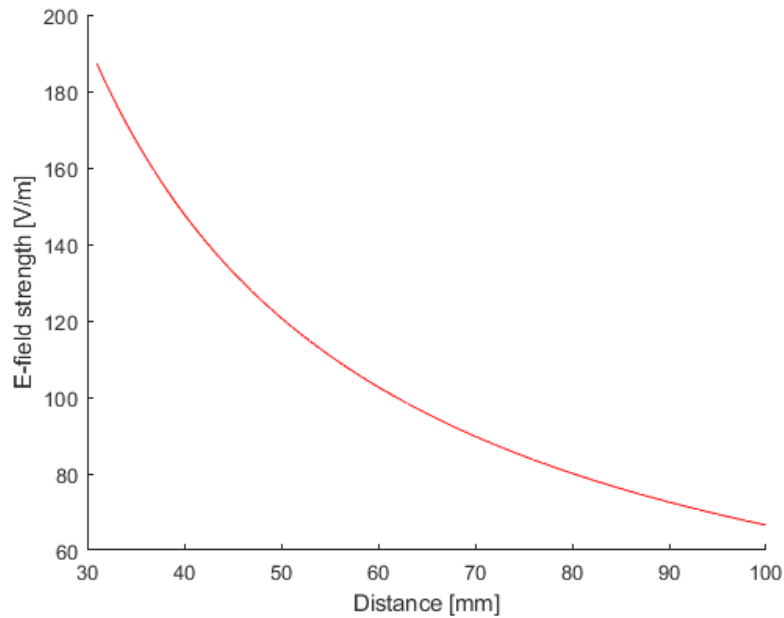


Figure 3.25. Dipole electric field strength decay with distance, near the far-field region.

Simulating now the AAUxxxxw in order to determine the behaviour of the electric field along the radiating near-field region in the direction of maximum radiation of the antenna, it was possible to obtain a representation of the electric field strength as a function of distance, presented in Figure 3.26.

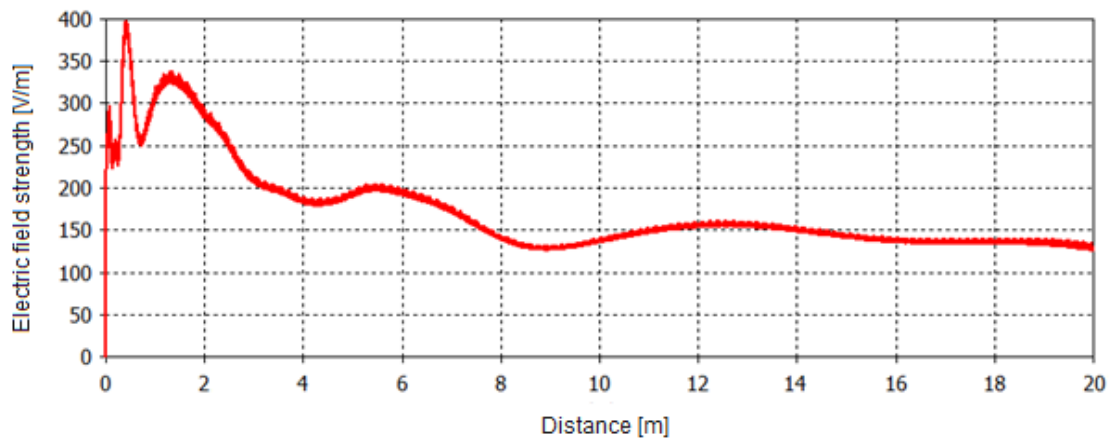


Figure 3.26. AAUxxxxw electric field strength decay with distance in the radiating near-field region.

With the obtained results, an overestimation of the electric field is performed, i.e., an interpolation is performed based on the maxima of the electric field strength as a function of distance. It is then possible to verify the expected behaviour in (3.30) through a regression, obtaining as fit coefficients: $C_2 = -297.5$ m, $C_1 = 513.2$ and $C_0 = 123.1$ m⁻¹. The near-field data, along with the respective fitted curve are represented in Figure 3.27.

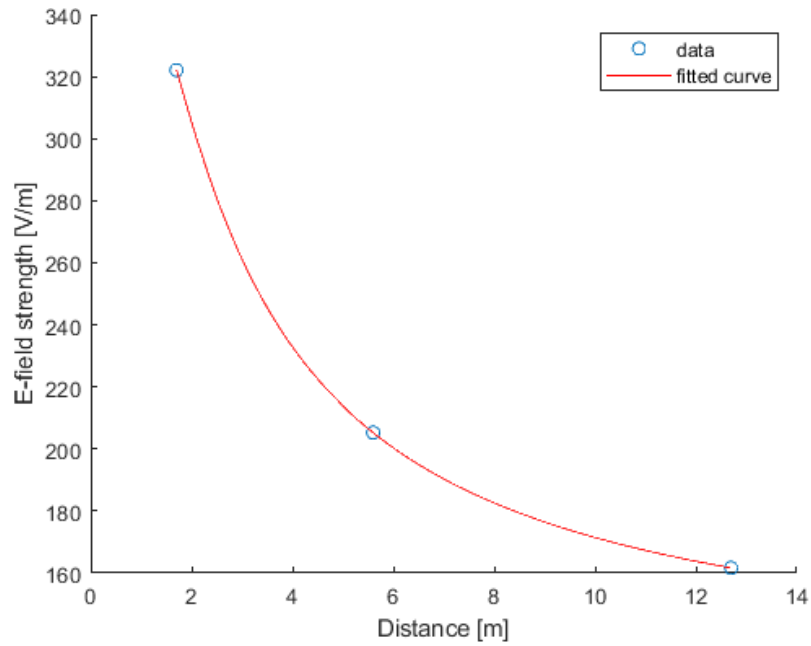


Figure 3.27. AAUxxxxw electric field strength decay with distance in the radiating near-field region.

Due to the high far-field region distances of the antenna under study, the resulting calculation domain would require an unavailable computational capacity in order to determine the electric field at these distances, using the previously used method. However, by using the Far-field Monitor tool, it is possible to observe an approximated behaviour of the electric field in the far-field region, concluding that the field decays proportionally to $1/d$, as expected. Figure 3.28 shows the electric field strength as a function of distance in the far-field region.

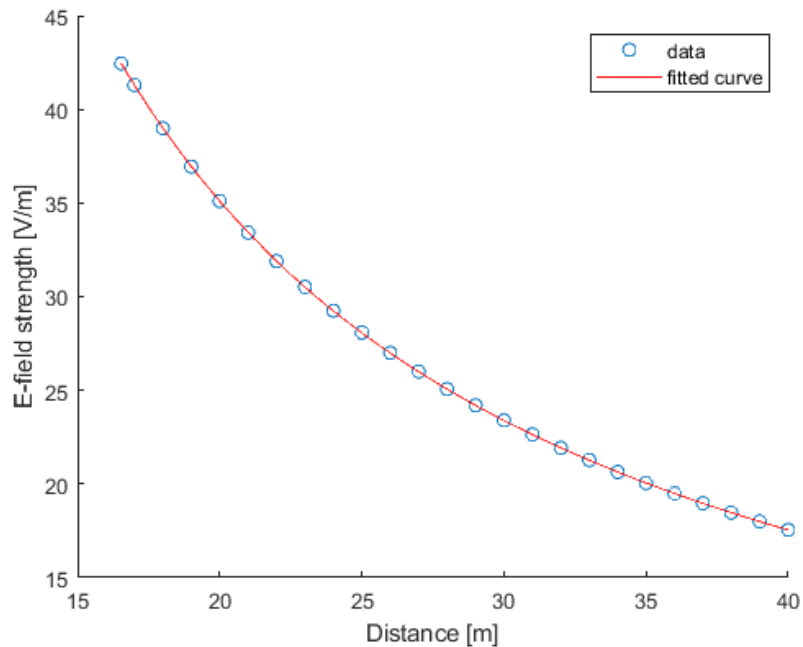


Figure 3.28. AAUxxxxw electric field strength decay with distance in the far-field region.

This behaviour, along with the 3D far-field patterns, are good indicators for assessing the correct design of the AAUxxxxw antenna in CST.

Given the behaviour of the field in the different radiating regions, it is possible to conclude that the limits between radiation regions seem to be according to the theoretical limits.

One should note that, while C_2 and C_1 coefficients define the curvature of the curve resulting from the performed regression, C_0 is only responsible for shifting the plot in the y -axis. Therefore, C_2 and C_1 remain constant but C_0 must change according to the computed far-field distance. Taking into account the behaviour of the electric field in the far-field region, it is necessary to make some adjustments to the obtained near-field curve in order to guarantee a smooth transition to the far-field region. Hence, the electric field plot for the near-field region must be shifted by updating C_0 , according to:

$$\frac{C_2[m]}{d_{[m]}^2} + \frac{C_1}{d_{[m]}} + C_0[m^{-1}] = \frac{1}{d_{[m]}} \Big|_{d_{[m]} = 16.54} \quad (3.31)$$

which results in a C_0 equal to -29.88 m^{-1} .

The final plot contemplating the field behaviour in both the radiating near- and far-field region is presented in Figure 3.29.

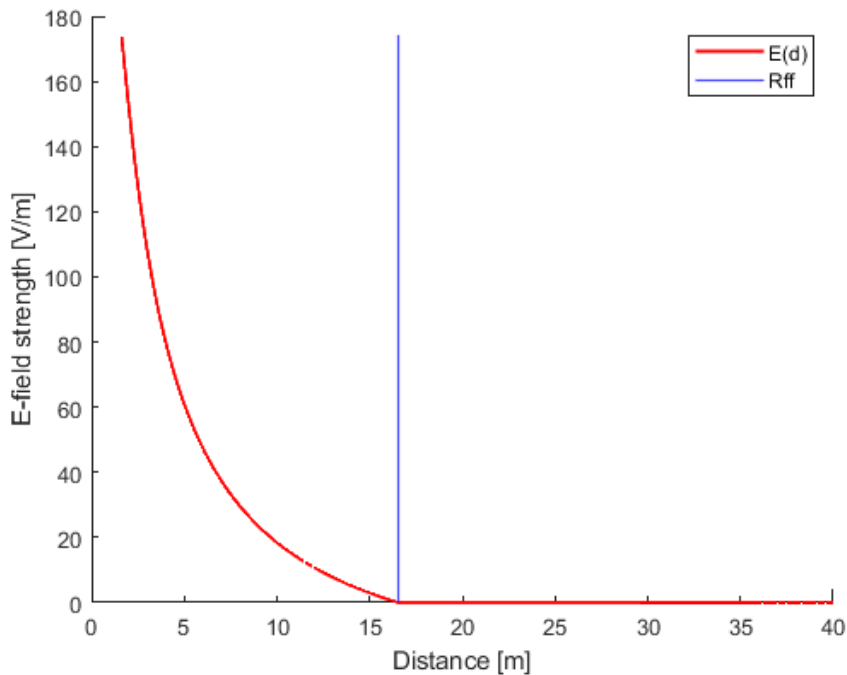


Figure 3.29. AAUxxxxw electric field strength decay with distance for the radiating near- and far-field regions using linear scale.

Since the electric field in the far-field region has a less pronounced decay than the one in the near-field region, the exact behaviour of the field along these two regions is not noticeable from the observation of the plot using a linear scale. Therefore, a plot using a logarithmic scale is presented in Figure 3.30 in order to allow the assessment of the behaviour of the electric field in both regions.

In order to simulate the antenna in the near-field region for other beam directions, a very large calculation domain would be necessary due to the increase in the Calculation Domain Box, requiring an amount of CPU and RAM that is not available. However, the decay of the field is expected to remain similar for

different beam directions, making it acceptable to extrapolate the obtained results for other directions besides the direction of maximum radiation.

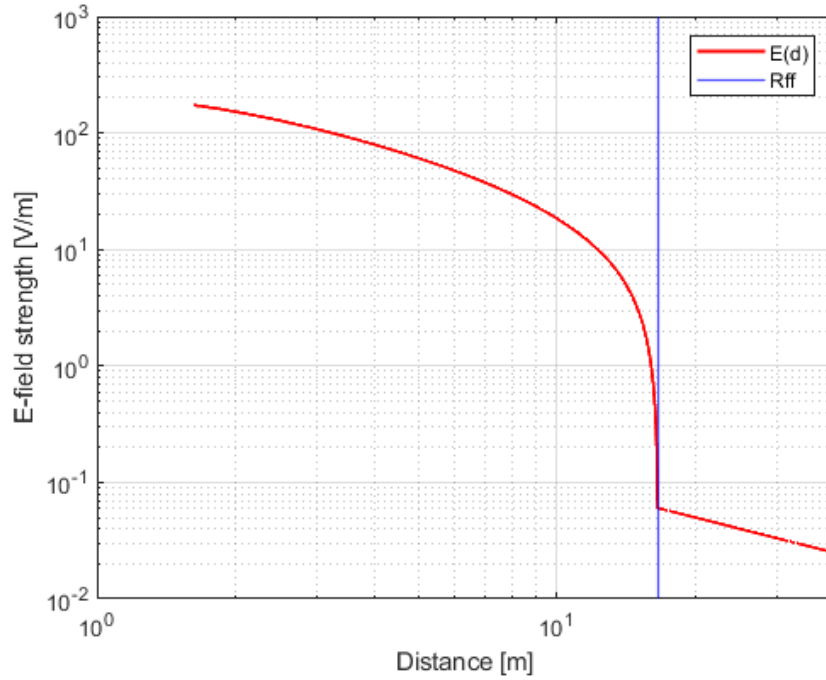


Figure 3.30. AAUxxxxw electric field strength decay with distance for the radiating near- and far-field regions using logarithmic scale.

3.4 Exclusion Zone Evaluation Model

Considering the results obtained in Subsection 3.3.4, the general expression for the electric field strength can be given by:

$$E(\theta, \phi, d)_{[V/m]} \cong V_{M[V]} f_{\theta\phi}(\theta, \phi) f_d(d)_{[m^{-1}]} \quad (3.32)$$

where:

- V_M : maximum voltage;
- $f_d(d)$: function representing the electric field dependency with distance.

The maximum voltage is given by:

$$V_M = \sqrt{30 P_{in} G_M} \quad (3.33)$$

The function representing the distance dependency of the electric field, $f_d(d)$, is given by:

$$f_d(d)_{[m^{-1}]} = \begin{cases} \frac{C_2[m]}{d_t^2[m]} + \frac{C_1}{d_t[m]} + C_0[m^{-1}], & R_{rnf} < d < R_{ff} \\ \frac{1}{d[m]}, & d \geq R_{ff} \end{cases} \quad (3.34)$$

Considering:

$$E(\theta, \phi, d_l) \cong E_{lim} \quad (3.35)$$

where:

- d_l : compliance distance;
- E_{lim} : electric field limit.

The compliance distance is then given by:

$$d_{l[m]} \cong \frac{2 C_{2[m]}}{-C_1 \pm \sqrt{C_1^2 - 4 C_{2[m]}(C_{0[m^{-1}]} - \alpha_{[m^{-1}]})}} \quad (3.36)$$

where:

- α : ratio between the electric field limit and the maximum voltage multiplied by normalised 3D antenna radiation pattern,

$$\alpha_{[m^{-1}]} = \frac{E_{lim[V/m]}}{V_{M[V]} f_{\theta\phi}(\theta, \phi)} \quad (3.37)$$

For the direction of maximum radiation, one has the maximum gain, i.e., $\max\{f_{\theta\phi}(\theta, \phi)\} = 1$. Hence, in this case, the computed distance corresponds to the front border of the exclusion zone, D_{front} . The dimensions of the exclusion zone for the remaining directions can be determined by applying correction factors to the maximum antenna gain, according to the antenna radiation patterns, obtaining a cylindrical exclusion zone such as the one described in the Subsection 2.5.2.

The power density limit, S_{lim} , is given by:

$$S_{lim} = \frac{S_{ref}(t)}{T_{var}(t)} \quad (3.38)$$

where:

- S_{ref} : power density reference level established by ICNIRP;
- $T_{var}(t)$: temporal variation contribution.

Since the region under study is the transition between the radiating near- and far-field regions, it is possible to consider the electric and magnetic fields directly interrelated by Z_0 , according to:

$$S = \frac{E^2}{120 \pi} \quad (3.39)$$

therefore,

$$E_{lim} = \sqrt{120 \pi S_{lim}} \quad (3.40)$$

Factors such as BS utilisation, DL duty cycle and spatial distribution of users should be considered in order to determine the temporal variation contribution to the variation of the electric field strength. Hence, the temporal variation contribution, T_{var} , may be given by:

$$T_{var}(t) = N_{RB}^{alloc,DL} \frac{N_{users}^{beam}}{N_{users}} F_{TDD} \quad (3.41)$$

In multiband networks, such as the case under study, it is important to understand if exposure effects add up. Therefore, the compliance distance must be determined for the case where the antennas for multiple bands are allocated and all the different spectrum bands are active. For this thesis, one can consider BS antennas as the only source of radiation since, in comparison, the remaining sources do not have as much impact inside the exclusion zone. Hence, only the frequencies in use in the BSs should be considered for exposure computation. Based on [ICNI20] and considering the reference values as well as the frequencies under study, one has:

$$S_{norm}^{tot}(d) = \sum_{i=1}^{N_{bands}} \left(\frac{S_{final,i}(d)}{S_{ref,i}} \right) \leq 1 \quad (3.42)$$

where:

- $S_{norm}^{tot}(d)$: total normalised power density;
- N_{bands} : number of active bands;
- $S_{final,i}(d)$: power density function for the i^{th} communication system;
- $S_{ref,i}$: power density ICNIRP reference level at frequency i .

The exclusion zone front boarder, corresponding to the distance of maximum radiation, D_{front} , is such that the total normalised power density is equal to 1. Computationally speaking, solving (3.42) as a function of distance is quite complex, since it is composed by two different models with two equations to describe each one. Therefore, an iterative process over different distance samples must be executed until the relationship is achieved. Due to MATLAB approximations and numerical precision, one should take into account that $S_{norm}^{tot}(d)$ is a discrete function with Δ_d as the sampling interval, thus, the distance for which $S_{norm}^{tot}(d)$ is exactly equal to 1 may not exist. Therefore, D_{front} must be given by the minimum distance that guarantees a $S_{norm}^{tot}(d) < 1$.

In order to determine the complete exclusion zone, the distances for the remaining directions can be computed by applying correction factors to the antenna gain, as stated previously. The normalised gains for each direction can be extracted from the radiation patterns of each system and applied as correction factors for the antenna gain.

The model developed in [Mour20] is used to calculate the exposure for GSM, UMTS, LTE and NR at 700 MHz, i.e., for passive antennas. This model, along with the defined parameters for the computation of the multi-band exposure, are presented in Annexe C. The method for determining the multi-band exposure is described in Figure 3.31.

The analysis of the exclusion zone results considering multi-band exposure can be enriched by taking into account the exclusion zone variation and the contribution of NR to the exclusion zone distance. The exclusion zone variation, Δ_{excl} , can be described as:

$$\Delta_{excl}[\%] = \left(\frac{D_{excl[m]}^{W NR} - D_{excl[m]}^{W/O NR}}{D_{excl[m]}^{W/O NR}} \right) \times 100 \quad (3.43)$$

where:

- $D_{excl}^{W NR}$: exclusion zone distance with NR;

- $D_{excl}^{W/O NR}$: exclusion zone distance without NR.

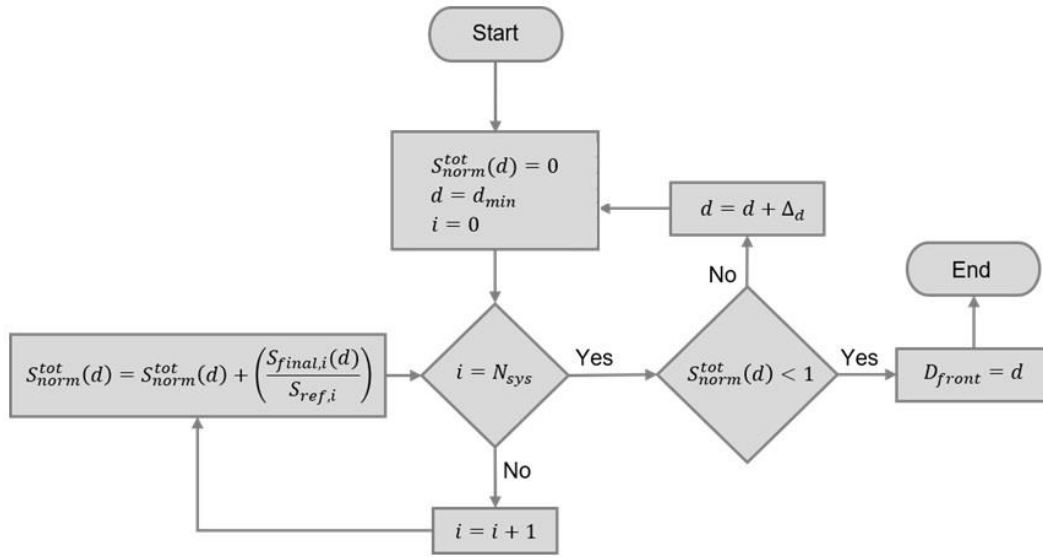


Figure 3.31. Computation of D_{Front} with the exclusion zone evaluation model for multi-band exposure (based on [Mour20]).

The contribution of NR to the exclusion zone distance, η_{NR} , can be given by:

$$\eta_{NR} [\%] = \left(\frac{D_{excl[m]}^{W NR} - D_{excl[m]}^{W/O NR}}{D_{excl[m]}^{W NR}} \right) \times 100 \quad (3.44)$$

One should note that the model does not take into consideration the surrounding environment, i.e., the presence of different objects in the vicinity of the antenna, such as poles, masts and buildings that do have some influence on the power density levels in this region.

3.5 Model Assessment

In order to assess the validity of the exclusion zone evaluation model, a set of empirical tests was performed, Table 3.4.

Through the analysis of Figures 3.32 and 3.33, it is possible to conclude that, by increasing the input power, the electric field strength and the exclusion zone front distance increased as well. From Figures 3.34 and 3.35, one is able to conclude that by increasing the gain, the electric field strength and the exclusion zone front distance also increased. Finally, Figure 3.36 shows a decrease in the exclusion zone front distance when increasing the power density reference level.

All performed tests had the expected results, concluding the assessment of the model. Although variations are not highly pronounced, it is possible to conclude that the model is behaving as expected.

The small variations can be explained by characteristics of the antenna, such as the quite high values of input power and gain being used.

Table 3.4. Empirical tests to validate the exclusion zone evaluation model (based on [Mour20]).

Test ID	Validation Element
1	Verify if the exclusion zone front border increases with the increase of the antenna input power.
2	Verify if the exclusion zone front border increases with the increase of the antenna gain.
3	Verify if the exclusion zone front border decreases with the increase of the reference values for exposure.

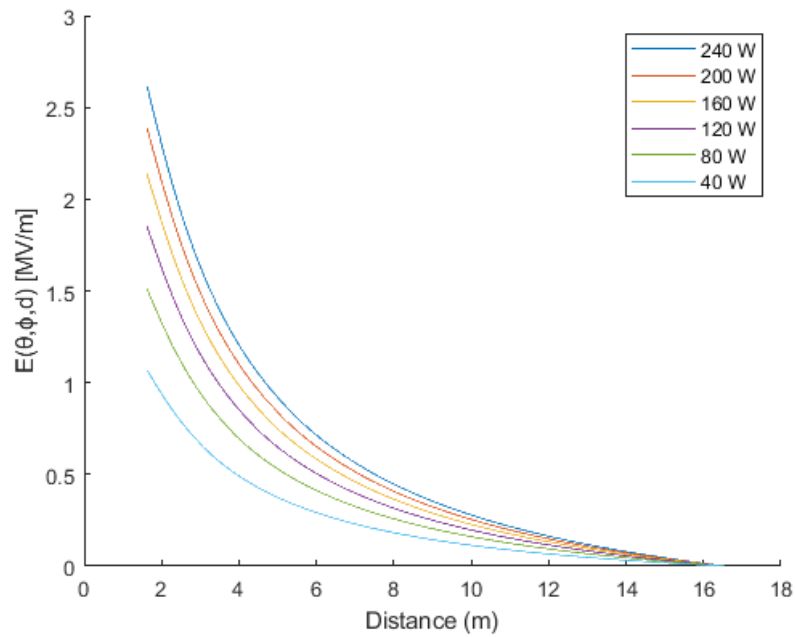


Figure 3.32. $E(\theta, \phi, d)$ as a function of distance varying the antenna input power.

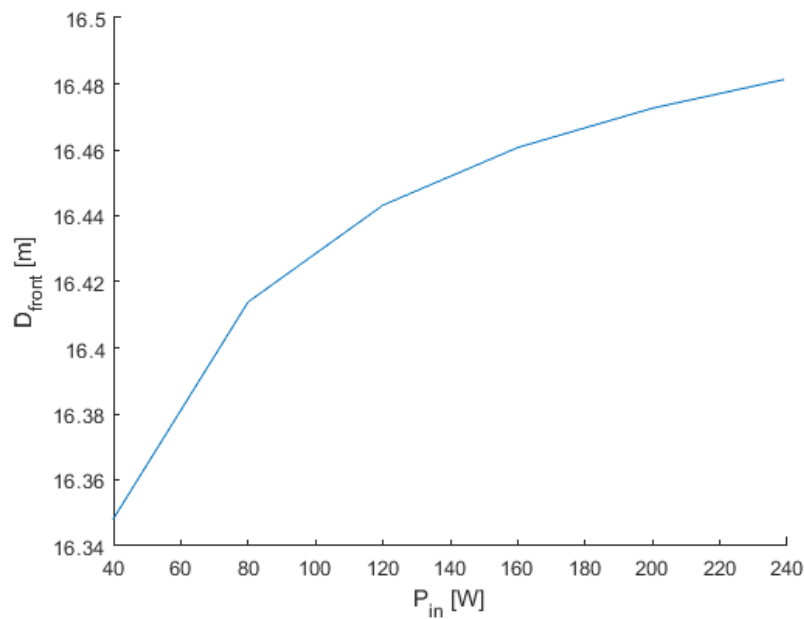


Figure 3.33. D_{front} as a function of antenna's input power with $G_M = 25$ dBi, $S_{ref} = 40$ and $T_{var} = 0.25$.

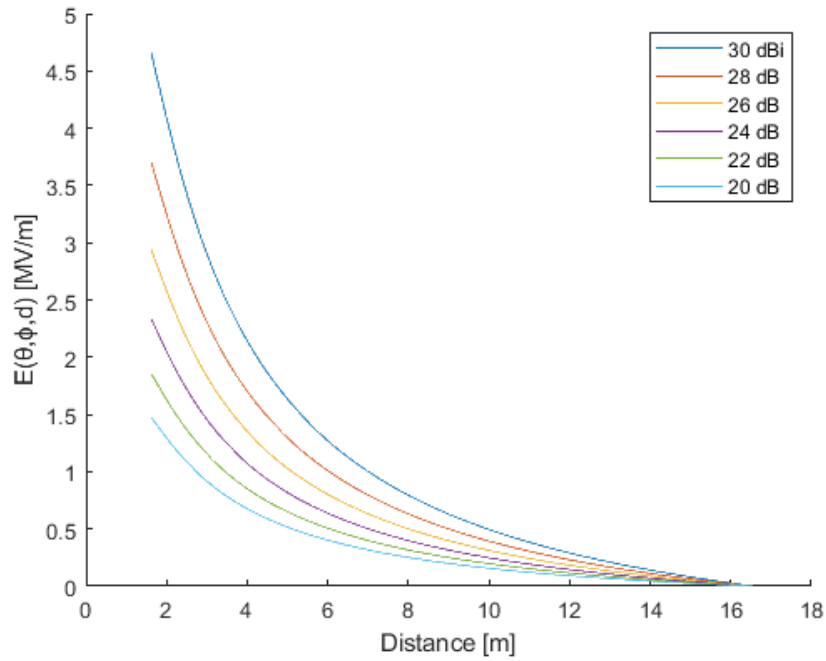


Figure 3.34. $E(\theta, \phi, d)$ as a function of distance varying the antenna gain.

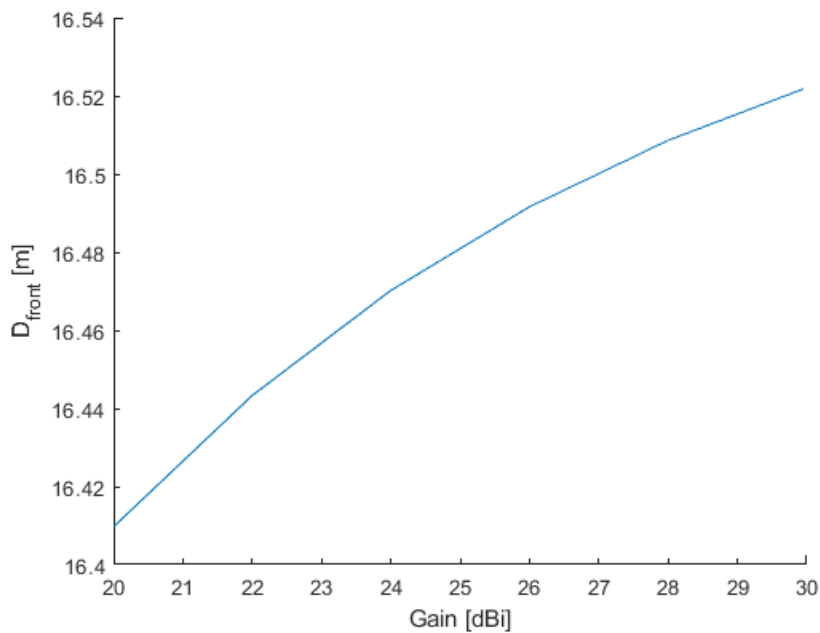


Figure 3.35. D_{front} as a function of the antenna gain with $P_{in} = 240 \text{ W}$, $S_{ref} = 40$ and $T_{var} = 0.25$.

One should note that, when taking the results obtained from the model, it is essential to carry out a careful and critical analysis of the model's validation interval, i.e., the conditions under which the model was developed and within what boundaries can it be applied in order to obtain valid results.

For the development of the exclusion zone model, the active behaviour of the NR antennas was taken into account by studying the time and beamforming behaviour of the antenna. However, the decay of the electric field with distance was exclusively determined based on the simulation of an active antenna with 96 active elements, for the direction of maximum radiation. Hence, the computed decay is based on large antennas with high gains and input powers, leading to an inevitable overestimation of the

results, since subarrays and other beam directions are not being taken into account. Therefore, the developed model is only valid within the previously established distances, not being very sensitive to variations in power and gain.

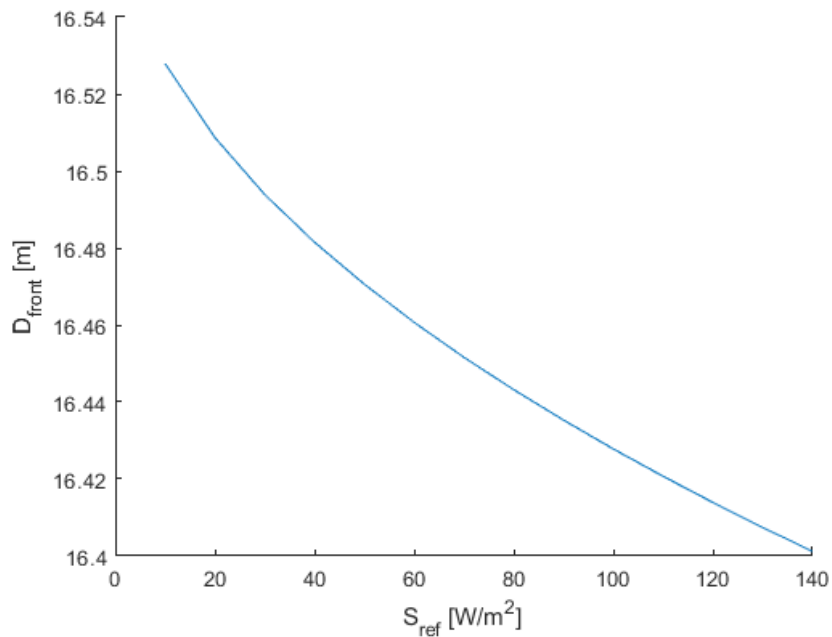


Figure 3.36. D_{front} as a function of the power density reference level established by ICNIRP with $P_{in} = 240$ W, $G_M = 25$ dBi and $T_{var} = 0.25$.

It is worth noting that, in the developed model, power, gain and other parameters, such as those defining the various scenarios are contained within a fourth root, causing the variations of these parameters to be quite attenuated.

Experimental EMF measurements were conducted in operational BSs in order to analyse the actual power decay in the vicinity of the BSs. The purpose of the measurements was to help evaluate the model by giving the deviation between these values and the ones resulting from the model. However, the comparison between the theoretical and measurements results was not possible due to the physical conditions of the rooftops, since they contained a reasonable number of reflective objects, as one can confirm in Figures B.1, B.5, B.6, B.7, and B.13, leading to meaningless and insufficient results which prevent proper conclusions.

Chapter 4

Results Analysis

This chapter presents the description of the different study scenarios as well as the analysis of the results.

4.1 Scenarios Description

Since the goal of the present study is to analyse EMF exposure levels as well as the impact of EMF restrictions on the computation of exclusion zones exclusively on outdoor BSs, indoor users served by indoor BSs are not taken into account.

First, the computation of the exclusion zone takes NR 3.6 GHz as the only active system. Later, the exclusion zone without NR (W/O NR), i.e., considering all systems to be active except for NR, as well as with NR (W NR), i.e., the exclusion zone considering all systems to be active including NR, is determined. The exclusion zone computation is done by considering the chosen scenarios and varying some parameters of interest, in order to assess their influence on the result.

It is important to notice that there are two different types of beams: the broadcast beam, always on air, and the traffic beams for user data, only on air when there is data to be exchanged (usually high gain narrow beams). According to [HUAW21a], the broadcast beam has an associated power equal to 19 dBm (0.08 W), hence, due to this very low power, only traffic beams are taken into consideration for the computation of exclusion zones.

Regarding NR3600, for all scenarios, the frequency in use is 3.6 GHz, the input power of the antenna, P_{in} , is equal to 240 W, the maximum antenna gain, G_M is equal to 25 dBi, and the maximum number of RBs is 273, considering a 100 MHz BS bandwidth, which corresponds to a SCS equal to 30 kHz [iTec21]. A realistic F_{TDD} value equal to 0.75 is considered.

It is possible to assume appropriate values for the temporal variation contribution to EMF exposure, T_{var} , based on previous studies conducted by means of simulations and statistical analysis. These studies give the percentage of the maximum transmit power per beam considering the 95th percentile, all of them having obtained very close and agreeing values.

While it is not advisable to use the maximum output power of the antenna due to interference and EMF exposure, it may be appropriate to do so in the case where the BS is only serving one user and the maximum power may allow better service results. However, in this case, special attention must be paid to the resulting increased EMF exposure.

For the different scenarios, different percentages of the maximum transmit power per beam values were defined based on [TFCT17]. Of all the works published in the literature, [TFCT17] is the one that gathers the best conditions regarding the goal of this thesis while also providing values for different types of environments, user distributions and system usage, making it suitable for most general cases.

In [TFCT17], a statistical model was developed to provide a realistic conservative EMF exposure assessment. The estimation of BS usage is based on the number of simultaneous users served by the system at a given time instant (the system being described using an M/M/1 queue). For the DL/UL transmission configuration, an F_{TDD} value of 0.75 has been assumed as a reasonable value for 5G. Since the maximum exposure is usually obtained when focused beams are used (LOS scenario), this is the case considered in this thesis. A 5G BS designed to cover $\pm 60^\circ$ in azimuth and $\pm 15^\circ$ in elevation is assumed.

Four User Distribution Scenarios (UDS) are defined in [TFCT17]. Urban_a considers an urban environment with a density of users uniformly distributed in azimuth and elevation. Urban_b is based on an urban environment with the highest density of users in the centre of both the azimuthal and elevation SR where the variation in elevation is chosen to reflect a larger density of users in the horizontal plane. The density of users is weighted by a cosine function in azimuth and a squared cosine distribution in elevation. Rural_a considers a rural environment with a density of users uniformly distributed in azimuth and no elevation scanning employed. Finally, Rural_b also takes into account a rural environment, but with a higher density of users in the centre of the azimuthal SR, weighted by a cosine function in azimuth and no elevation scanning employed. Since, in [TFCT17], only percentages for urban and rural environments were provided, an average between those two environments values was considered for the suburban one.

The distribution of users within the cell was determined using cumulative binominal distribution functions in order to guarantee the exposure contributions from the broadside and adjacent directions conservatives for 95% of all possible exposure scenarios. Another conservative parameter is the number of served independent users during the averaging time, chosen to correspond to a realistic maximum activity factor, i.e., the ratio between the averaging time and the total average scheduling time per user equal to 10 (considering a low peak 5G data rate of 50 Mbps).

The conservativeness of the model depends also on the chosen system usage. According to [TFCT17], the maximum values for EMF exposure were found to occur for very large degrees of system usage. However, in practice, usage levels close to 100% are unrealistic, since this may lead to a decrease in QoS. 2016 network-based measurements in a Swedish LTE network showed a 95th percentile system usage of about 11% [JTCT16]. According to [HUAW21a], the expected average number of connected users in a 5G BS is estimated to be around 60 users by 2025. Therefore, considering high usage levels will most certainly generate conservative results. The described scenarios along with the corresponding percentage of the maximum transmit power per beam (considering the 95th percentile) for two different system usage levels are presented in Table 4.1.

Table 4.1. Percentage of maximum transmit power/beam for different scenarios and system usages.

Scenarios	Percentage of the maximum transmit power/beam (95 th percentile) [%]	
	System usage, ρ [%]	
	50	95
Urban_a	2.50	7.00
Urban_b	5.00	13.00
Suburban_a	4.25	11.00
Suburban_b	6.50	17.50
Rural_a	6.00	15.00
Rural_b	8.00	22.00

It is important to note the results taken from [TFCT17] were determined for an 8×8 array antenna with an element spacing of $\lambda/2$, using a model developed to be applied in the far-field. Thus, although

supported by other papers, one should look at these values only as an approximation.

Since the duration of EMF exposure has a direct impact on the reference level for exposure, it is necessary to choose appropriate values for the duration of exposure when computing the exclusion zone. According to the access times and average session durations defined in Subsection 3.2.1, different averaging times are set, corresponding to different reference levels based on ICNIRP guidelines. The power density reference levels for the different systems considering averaging times equal to 1 min, 6 min and 30 min are presented in Table 4.2. One should note that “NA” means that the entity does not need to be taken into account when computing the results for the different scenarios. Power density reference levels for the different systems, averaged over 1 min, 6 min and 30 min, were determined based on Tables 2.12, 2.13 and 2.14, respectively.

Table 4.2. Power density reference levels, averaged over 1 min, 6 min and 30 min.

System	S_{ref} [W/m ²]		
	Averaging Time [min]		
	1	6	30
NR700	NA	17.47	3.82
LTE800	NA	18.51	4.08
GSM/UMTS900	NA	20.97	4.72
LTE1800	NA	37.17	9.18
UMTS/LTE2100	NA	40.00	10.00
LTE2600	NA	40.00	10.00
NR3600	98.00	40.00	10.00

In order to study the exposure when several systems are active in the BS, 9 different outdoor scenarios were defined (3 in each environment, i.e., urban, suburban and rural). The definition of these scenarios is based not only on the NR active antennas but also on the typical antennas installed previous to the implementation of NR. Hence, it is possible to determine the variation of the exclusion zone region before and after NR installation on the BSs. The different scenarios along with the active mobile communication systems and frequency bands are presented in Table 4.3.

For each of the mobile communication systems, an output power per carrier (in the case of GSM and UMTS) and an output power per MIMO element (in the case of LTE and NR) is defined in Table 4.4. The number of MIMO elements for each LTE and NR band is presented in Table 4.5.

Since the number of carriers, N_c , used in a system may differ for distinct BSs installations, the exclusion zone distances corresponding to the broadside direction, D_{front} , should be obtained by taking different carrier configurations. Hence, in order to obtain a wide variety of results, four different configurations ($N_{c\text{ GSM900}}/N_{c\text{ UMTS}}$) are defined: 1/1, 2/1, 4/2 and 4/4. One should note that $N_{c\text{ UMTS}}$ is referring to the number of carriers for all UMTS bands, e.g., for a scenario that makes use of the 900 MHz and 2100 MHz bands, a 4/2 configuration means that 2 carriers are being used for each one.

The number of carriers and MIMO elements must be accounted for in the input power of the antenna, i.e., a system with 2 carriers and 20 W per carrier has a P_{in} equal to 40 W. The same behaviour is

applied to systems with MIMO. It is important to notice that this method generates more conservative results, since it assumes that the direction of maximum radiation is the same for different carriers and MIMO beams.

Table 4.3. Active mobile communications systems in each scenario (based on [Mour20]).

Scenarios	Mobile Communications Systems Frequency Bands								
	GSM	UMTS		LTE				NR	
	900	900	2100	800	1800	2100	2600	700	3600
Urban 1	×		×		×				×
Urban 2	×		×	×			×		×
Urban 3	×		×		×		×	×	×
Suburban 1	×	×	×	×	×				×
Suburban 2	×	×		×		×		×	
Suburban 3	×		×	×	×	×		×	×
Rural 1	×	×		×				×	
Rural 2	×	×	×			×		×	
Rural 3	×	×	×	×		×		×	×

Table 4.4. Output power per carrier/MIMO element and antenna gain for the considered systems.

System		Central Frequency, f_c [MHz]	Output Power per Carrier/MIMO Element [W]	Maximum Antenna Gain [dBi]
GSM	900	943	20.00	16.0
UMTS	900	943	20.00	16.0
	2100	2137	30.00	15.9
LTE	800	816	40.00	15.5
	1800	1835	40.00	15.5
	2100	2137	10.00	15.9
	2600	2660	40.00	16.7
NR	700	763	40.00	15.2
	3600	3650	3.75	25.0

Table 4.5. Number of MIMO elements for each band of LTE and NR.

System		Number of MIMO elements
LTE	800	2
	1800	2
	2100	2
	2600	4
NR	700	2
	3600	64

One should also take into account that the values used for the transmitting powers in GSM, UMTS, LTE and NR are the maximum ones, leading to a more conservative exclusion zone. The actual transmitted power for each system varies throughout the day and depends on BS usage and power control.

While, for NR3600, the previously studied AAUxxxxw active antenna is considered, for GSM, UMTS, LTE and NR700, a single passive antenna should be taken into account, the ASlxxxxxxxx6. The technical characteristics of these antennas can be found in Annexe A.

4.2 Exclusion Zone for Broadside Beam Direction

The results for the computation of D_{front} when only NR is active in the BS are presented in Table 4.6 for the Urban_a, Suburban_a and Rural_a scenarios, considering a system usage of 50% and 1 min, 6 min and 30 min as averaging times. Results for the Urban_b, Suburban_b, and Rural_b scenarios, as well as for other system usage and averaging times, were also determined, however, since the model has been proven not to be very sensitive to variations in scenarios and respective parameters, only a representative sample of the results is presented.

Table 4.6. D_{Front} for Urban, Suburban and Rural scenarios with only 3.6 GHz active.

Scenario	T_{avg} [min]	D_{Front} [m]
Urban	1	16.12
	6	16.28
	30	16.43
Suburban	1	16.23
	6	16.35
	30	16.46
Rural	1	16.28
	6	16.39
	30	16.48

In order to facilitate a comparison with the results from [Mour20], the computation of the exclusion zone taking into account multi-band exposure was made for an averaging time of 30 min, considering a system usage of 50%. The results taking 100% of the maximum transmit power per beam and the actual percentage of the maximum transmit power per beam for each scenario are presented, for each carrier configuration, in Figures 4.1, 4.2, 4.3, 4.4, 4.5, 4.6, 4.7 and 4.8, respectively.

In a first analysis, it is possible to conclude that the compliance distance with active 3.6 GHz is much higher when considering 100% of the maximum transmit power per beam than in the case where the actual percentage of the maximum transmit power per beam of each scenario is taken, as expected. However, this difference is the most noticeable when using an averaging time equal to 30 min, since it

is the averaging time corresponding to the lowest power density reference level. In this case, when considering 100% of the maximum transmit power per beam, the compliance distance is no longer within the near-field region but in the far-field one, which explains the increase in the exclusion zone front boarder (in the far-field region, the field decay with distance is much less pronounced).

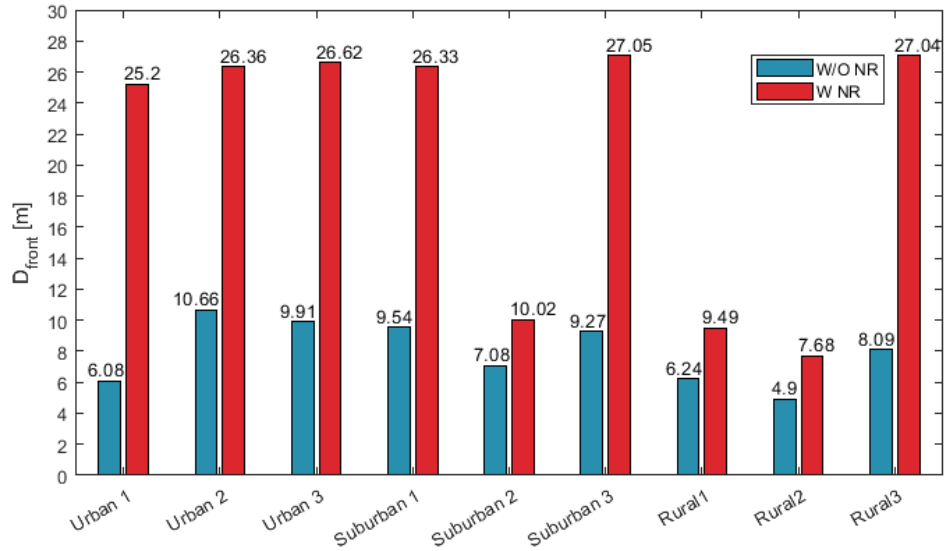


Figure 4.1. D_{front} for the carrier configuration 1/1 taking 100% of the maximum transmit power/beam.

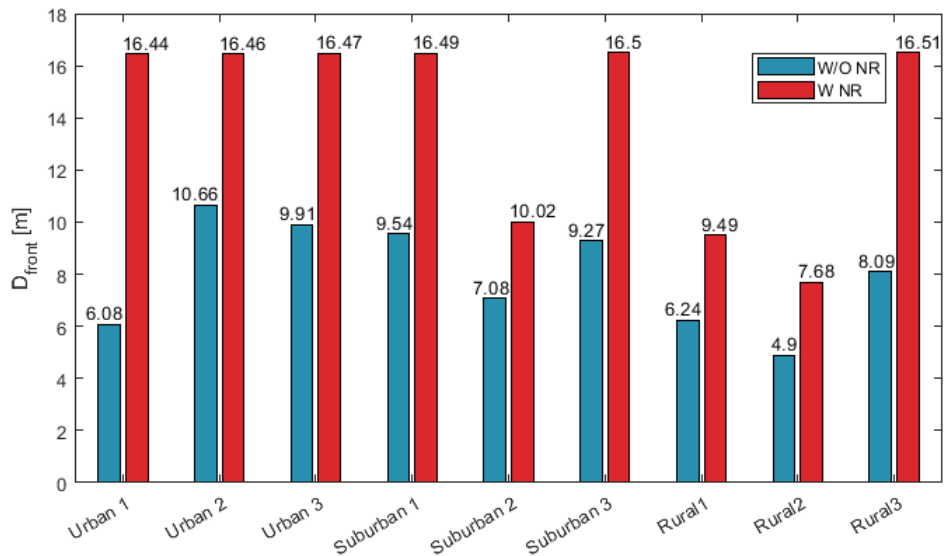


Figure 4.2. D_{front} for the carrier configuration 1/1 taking the actual transmit power/beam.

Another general conclusion to extract from these results is the fact that the compliance distance, when accounting multi-band exposure with all active systems, is almost the same as the one obtained when considering only NR3600, which can be explained by the fact that, at the computed distance, legacy systems do not have much impact, because of their lower gains and input powers in comparison with the ones from NR3600 and the fact that almost every system is within the near-field region, excluding LTE1800, UMTS2100 and LTE2100, which cause the field to decay much faster with distance than it would in the far-field region.

The increase in D_{front} is overall lower for the scenarios that only consider the deployment of NR700, as

opposed to the environments where NR3600 is installed, since NR700 works with passive antennas, having transmitted powers and antenna gains significantly lower than the ones used in NR3600. The variation of D_{front} due to NR installation and NR contribution to D_{front} for each scenario and carrier configuration obtained from (3.43) and (3.44), respectively, are presented in Tables 4.7 and 4.8.

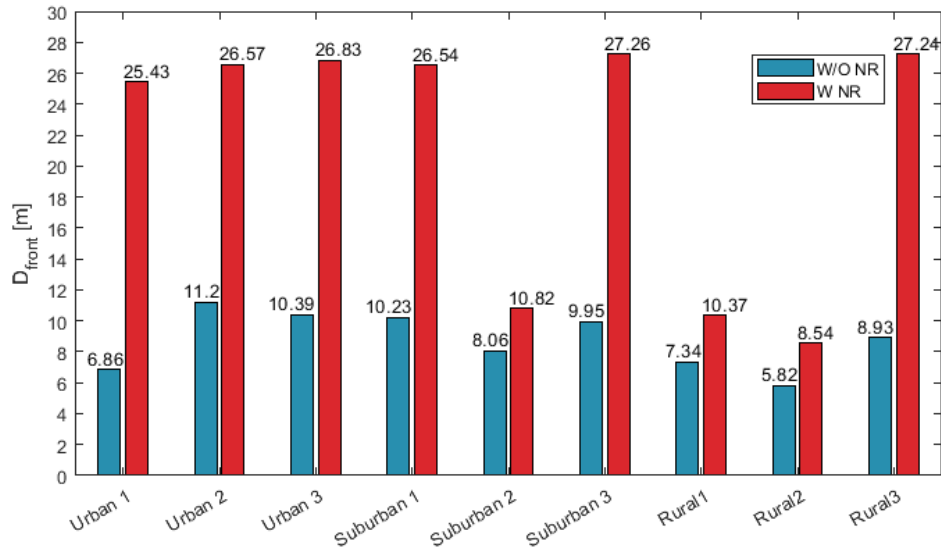


Figure 4.3. D_{front} for the carrier configuration 2/1 taking 100% of the maximum transmit power/beam.

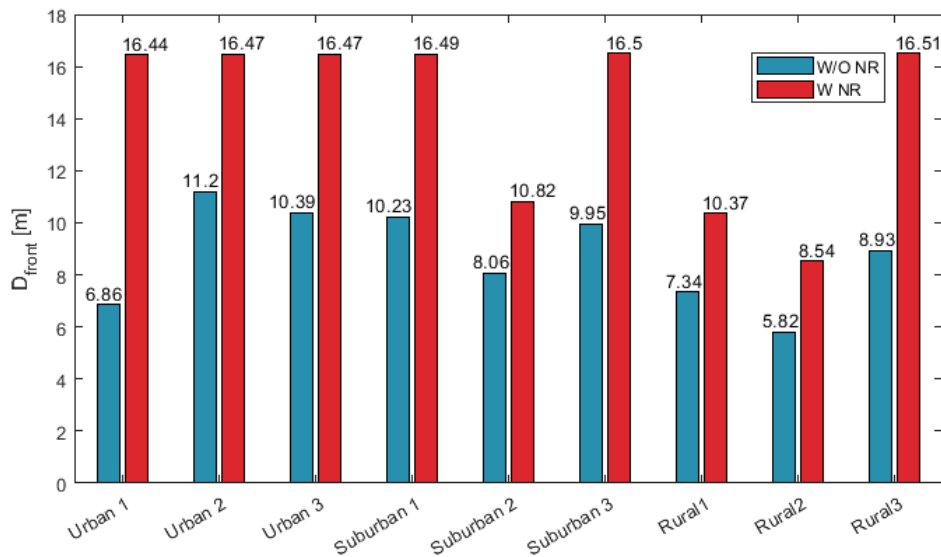


Figure 4.4. D_{front} for the carrier configuration 2/1 taking the actual transmit power/beam.

Taking into account 100% of the maximum transmit power per beam, it is possible to conclude that the increase in the compliance distance due to the installation of NR ranges from 92.4% to 314.4% (urban scenarios), from 17.3% to 191.8% (suburban scenarios) and from 16.4% to 234.2% (rural scenarios). However, when the actual percentage of the maximum transmit power per beam of each scenario is considered, it is possible to conclude that the increase in the compliance distance due to the installation of NR ranges from 24.3% to 170.4% (urban scenarios), from 16% to 78% (suburban scenarios) and from 16.4% to 104.1% (rural scenarios). The obtained results show a decrease in the compliance distance when considering actual maximum transmit powers instead of assuming the maximum values, as expected.

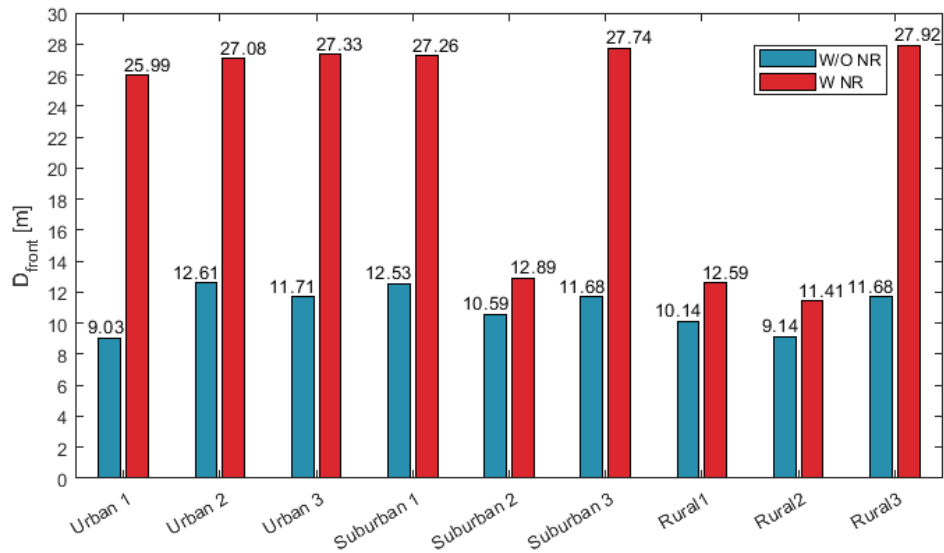


Figure 4.5. D_{front} for the carrier configuration 4/2 taking 100% of the maximum transmit power/beam.

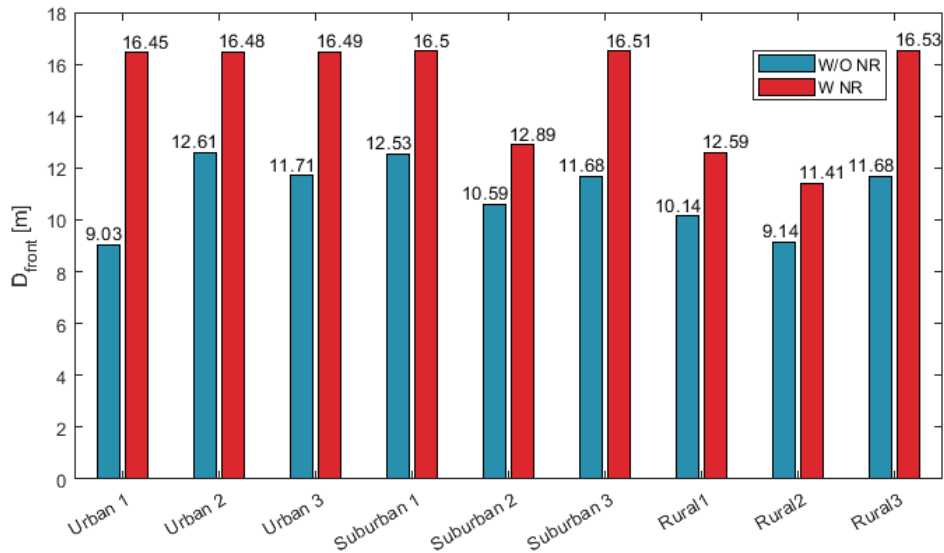


Figure 4.6. D_{front} for the carrier configuration 4/2 taking the actual transmit power/beam.

Regarding the carrier configuration 1/1, for urban scenarios, D_{front} W/O NR ranges from 6.08 m (Urban 1) to 10.66 m (Urban 2). The increase in compliance distance from Urban 1 to Urban 2 can be easily explained by the presence of LTE800 in Urban 2 and the higher gain of LTE2600 compared to LTE1800, as well as its higher transmitted power caused by a higher MIMO order.

For Urban 3, the compliance distance is higher than for Urban 1, as expected, since for this scenario both LTE1800 and LTE2600 are present. However, the compliance distance for Urban 3 is lower than the one computed for Urban 2, which may seem unexpected at first, since both scenarios have the same total transmitted power and gain. However, one should keep in mind that lower exposure limits are set for lower frequency systems (below 2 GHz) [ICNIRP]. Therefore, it is expected that scenarios working with lower bands produce higher compliance distances. After the installation of NR, D_{front} ranges from 16.44 m (Urban 1) to 16.47 m (Urban 3), which is not that meaningful.

Regarding the suburban scenarios, D_{front} W/O NR ranges from 7.08 m (Suburban 2) to 9.54 m

(Suburban 1). The lower compliance distance for Suburban 2 was expected due to the total reduction in transmitted power compared to the other scenarios. With the deployment of NR, it is possible to confirm the higher increase in compliance distance associated with the installation of AAs in the 3.6 GHz band. For Suburban 1 and Suburban 3, where NR3600 is active, D_{front} is 16.49 m and 16.50 m, respectively, being substantially higher than the compliance distance, when only NR700 is active, with a D_{front} equal to 10.02 m.

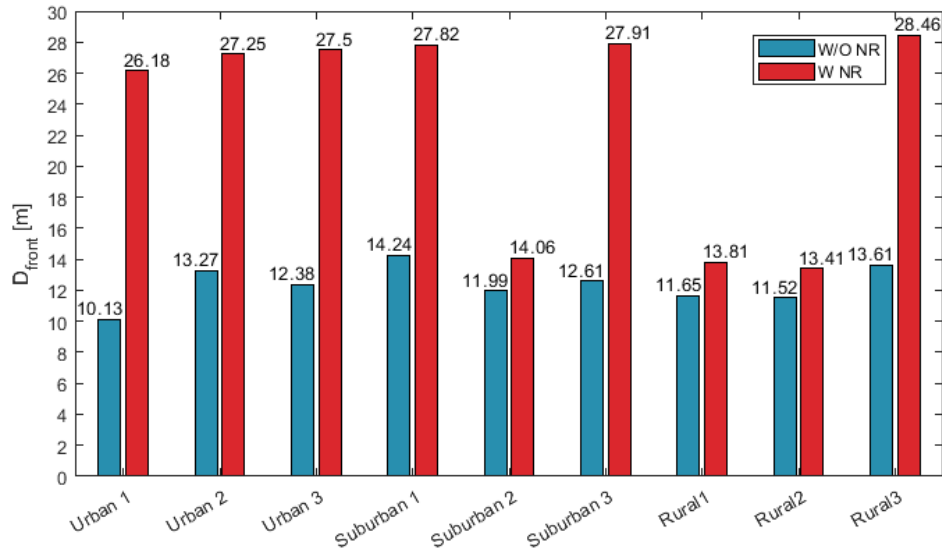


Figure 4.7. D_{front} for the carrier configuration 4/4 taking 100% of the maximum transmit power/beam.

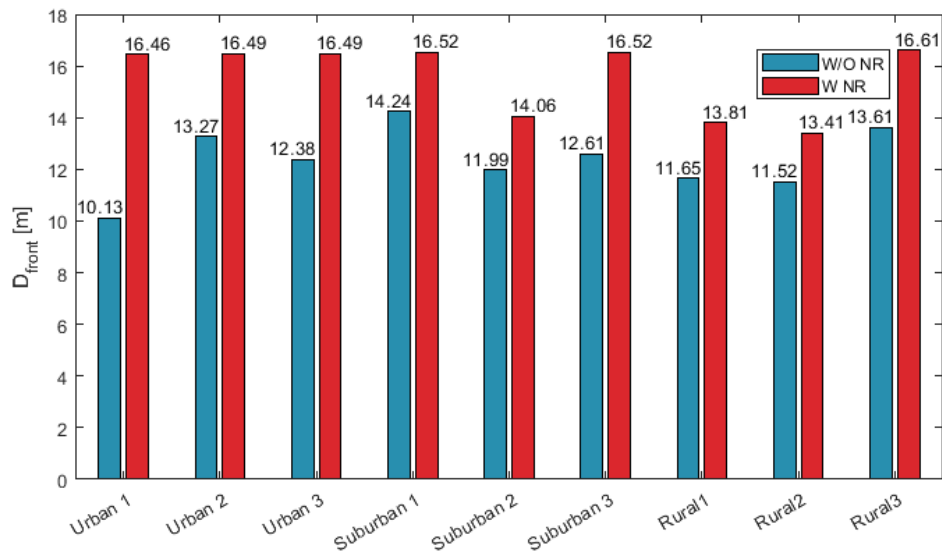


Figure 4.8. D_{front} for the carrier configuration 4/4 taking the actual transmit power/beam.

In the rural scenarios, D_{front} W/O NR ranges from 4.90 m to 8.09 m. These results can be explained by the total transmitting power for each scenario. D_{front} W NR ranges between 7.68 m (Rural 2) and 16.51 m (Rural 3). This quite high increase of the compliance distance for Rural 3 can be easily justified by the presence of NR300 in addition to NR700.

For the carrier configuration 2/1, D_{front} results are higher than the ones obtained for the 1/1 configuration, as expected, since every scenario includes GSM900 and its transmitted power doubles

in the 2/1 configuration.

Table 4.7. D_{front} variation due to NR installation for each scenario and carrier configuration.

Scenarios	$\Delta_{excl}[\%]$							
	100% of the maximum transmit power/beam				Actual percentage of the maximum transmit power/beam			
	$N_{c\text{ GSM900}}/N_{c\text{ UMTS}}$							
	1/1	2/1	4/2	4/4	1/1	2/1	4/2	4/4
Urban 1	314.4	270.7	187.8	158.4	170.4	139.7	82.2	62.5
Urban 2	147.3	137.2	114.8	105.4	54.4	47.1	30.7	24.3
Urban 3	168.6	158.2	133.4	122.1	66.2	58.5	40.8	33.2
Suburban 1	176.0	159.4	117.6	95.4	72.8	61.2	31.7	16.0
Suburban 2	41.5	34.2	21.7	17.3	41.5	34.2	21.7	17.3
Suburban 3	191.8	174.0	138.9	121.3	78.0	65.8	41.4	31.0
Rural 1	52.1	41.3	24.2	18.5	52.1	41.3	24.2	18.5
Rural 2	56.7	46.7	24.8	16.4	56.7	46.7	24.8	16.4
Rural 3	234.2	205.0	139.0	109.1	104.1	84.9	41.5	22.0

Table 4.8. NR contribution to D_{front} for each scenario and carrier configuration.

Scenarios	$\eta_{NR}[\%]$							
	100% of the maximum transmit power/beam				Actual percentage of the maximum transmit power/beam			
	$N_{c\text{ GSM900}}/N_{c\text{ UMTS}}$							
	1/1	2/1	4/2	4/4	1/1	2/1	4/2	4/4
Urban 1	75.9	73.0	65.3	61.3	63.0	58.3	45.1	38.5
Urban 2	59.6	57.8	53.4	51.3	35.2	32.0	23.5	19.5
Urban 3	62.8	61.3	57.2	55.0	39.8	36.9	29.0	24.9
Suburban 1	63.8	61.5	54.0	48.8	42.1	38.0	24.1	13.8
Suburban 2	29.3	25.5	17.8	14.7	29.3	25.5	17.8	14.7
Suburban 3	65.7	63.5	58.1	54.8	43.8	39.7	29.3	23.7
Rural 1	34.2	29.2	19.5	15.6	34.2	29.2	19.5	15.6
Rural 2	36.2	31.9	19.9	14.1	36.2	31.9	19.9	14.1
Rural 3	70.1	67.2	58.2	52.2	51.0	45.9	29.3	18.1

With the installation of NR, the compliance distance increases from 6.86 m to 16.44 m (Urban 1), from 11.20 m to 16.47 m (Urban 2) and from 10.39 m to 16.47 m (Urban 3). As expected, for the urban scenarios, D_{front} is higher for scenarios with GSM900, UMTS2100, LTE2600 and LTE1800, reaching the lowest value for the scenario where only GSM900, UMTS2100 and LTE1800 are active.

Regarding suburban and rural scenarios, D_{front} W/O NR ranges from 8.06 m to 10.23 m and from 5.82 m to 8.93 m, respectively. With the installation of NR, D_{front} ranges from 10.82 m to 16.50 m for

the suburban scenarios and from 8.54 m to 16.51 m for the rural scenarios.

Considering the carrier configuration 4/2, it is possible to conclude that the results follow the expected behaviour, since by doubling the number of transmitted carriers for both GSM900 and UMTS2100 in respect to the 2/1 carrier configuration, an increase in the compliance distance is expected.

Regarding the urban scenarios, D_{front} increases from 9.03 m W/O NR to 16.45 m W NR (Urban 1), from 12.61 m W/O NR to 16.48 m W NR (Urban 2) and from 11.71 m to 16.49 m (Urban 3). In the suburban scenarios, D_{front} increases from 12.53 m W/O NR to 16.50 m W NR (Suburban 1), from 10.59 m W/O NR to 12.89 m W NR (Suburban 2) and from 11.68 m to 16.51 m (Suburban 3). In the case of rural scenarios, D_{front} increases from 10.14 m W/O NR to 12.59 m W NR (Rural 1), from 9.14 m W/O NR to 11.41 m W NR (Rural 2) and from 11.68 m to 16.53 m (Rural 3).

In respect to the carrier configuration 4/4, for urban scenarios, D_{front} W/O NR ranges from 10.13 m to 13.27 m while D_{front} W NR ranges from 16.46 m to 16.49 m. For the suburban scenarios, D_{front} W/O NR ranges between 11.99 m and 14.24 m and D_{front} W NR ranges from 14.06 m to 16.52 m. One should note that, although Suburban 1 has a higher D_{front} W/O NR, Suburban 3 has both NR bands active, explaining the equal D_{front} W NR result for both scenarios. Finally, for rural scenarios, the D_{front} W/O NR ranges between 11.52 m and 13.6 m while D_{front} W NR ranges between 13.41 m and 16.61 m. The values for the compliance distance are higher for this configuration, since it is the one generating higher total transmitted powers.

As stated before, the scenarios with the highest total transmitted power are not always the ones producing the highest compliance distances. Another example of that behaviour happens in the 4/4 carrier configuration, where Rural 2 has a total transmitted power equal to 300 W and a D_{front} equal to 11.52 m, while Rural 1 has a total transmitted power of 240 W and a D_{front} equal to 11.65 m. Thus, although Rural 1 has a total transmitted power 60 W below the one from Rural 2, its compliance distance is 13 cm higher.

Because of the unaltered radio configuration of NR700 and NR3600 throughout the different scenarios, a lower D_{front} increase is expected when installing NR in BSs with a higher transmitting power from legacy systems, which happens in all scenarios, being in agreement with the first general analysis of results. Therefore, EMF influence of NR decreases as the influence of legacy systems increases.

It is possible to conclude that the contribution of NR3600 to D_{front} is significantly higher than the contribution of each legacy system individually. The lowest contribution of NR3600 is 13.8%, which corresponds to 86.2% of the total contribution distributed amongst the legacy systems.

Due to the high compliance distances obtained, some considerations should be taken into account regarding public exposure in urban scenarios. For scenarios where the antennas are installed close to the ground, such as the Ufaçade (3 m to 10 m) and Upole (3 m to 5 m) installations, presented in Table 2.11, physical barriers may need to be installed at street level. For suburban and rural scenarios, the typical BS height for these environments should be enough to ensure the safety of the population, avoiding the installation of physical barriers at ground level.

Another important aspect to take into account is the possible downtilt associated with the antenna installation. Depending on its value, this downtilt may increase the amount of exposure on the street. In addition, since NR active antennas have vertical beam sweeping, the exposure at street level increases because a higher antenna gain is maintained for lower angles. This scenario is represented in Figure 4.9.

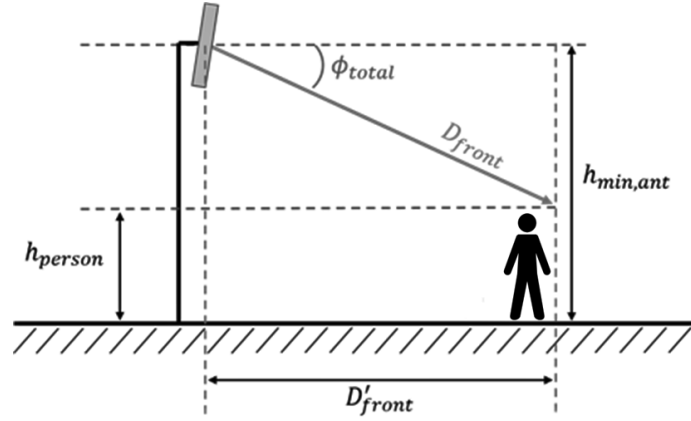


Figure 4.9. Downtilt influence on the exclusion region (adapted from [Antu12]).

The front border of the exclusion zone when a downtilt is applied can be given by, [Mour20]:

$$D'_{front} = D_{front} \cos(\phi_{total}) \quad (4.1)$$

where:

- ϕ_{total} : total inclination of the maximum antenna gain.

The direction of maximum radiation is assumed to be located at the centre of the vertical SR, thus half of the 3 dB beamwidth, θ_B , which is approximately 34° , is added to the downtilt angle resulting in the total inclination of the maximum antenna gain, ϕ_{total} . In a simplified approach, only mechanical downtilts are being considered, leaving out possible electrical ones in order to ensure that the radiation pattern remains unchanged, being only rotated by θ_{dt} .

The total inclination of the maximum antenna gain is given by:

$$\phi_{total} = \theta_{dt} + \frac{\theta_B}{2} \quad (4.2)$$

where:

- θ_{dt} : downtilt angle.

The minimum required antenna height, $h_{min,ant}$, in order not to install physical barriers is given by:

$$h_{min,ant} = h_{person} + (D_{front} \sin(\phi_{total})) \quad (4.3)$$

where:

- h_{person} : average height of a person.

If the height of the antenna is above $h_{min,ant}$ there is no need to install physical barriers, however, if it is below, the distance at which physical barriers must be installed is given by D'_{front} . The results for the urban scenarios are presented in Tables 4.9, 4.10 and 4.11 for Urban 1, Urban 2 and Urban 3,

respectively.

For the computation of these results, the worst cases were considered, i.e., 4/2 and 4/4 carrier configurations with a downtilt of 12°, which can be considered a high value for urban scenarios [Mour20]. For scenarios W/O NR, the vertical SR is 0° since only passive antennas are being used. The average height of a person was considered to be 1.80 m, which is higher than the one of a Portuguese adult [ELIF16]. As a result, there is no need for physical barriers to be installed at ground level in urban scenarios BSs for antennas taller than 9.79 m.

Table 4.9. Downtilt influence on the definition of physical barriers for the Urban 1 scenario.

Scenario	$N_c \text{ GSM900}/N_c \text{ UMTS}$		D_{Front} [m]	D'_{front} [m]	$h_{min,ant}$ [m]
Urban 1	4/2	W/O NR	9.03	8.83	3.68
		W NR	16.45	14.39	9.78
	4/4	W/O NR	10.13	9.91	3.91
		W NR	16.46	14.40	9.78

Table 4.10. Downtilt influence on the definition of physical barriers for the Urban 2 scenario.

Scenario	$N_c \text{ GSM900}/N_c \text{ UMTS}$		D_{Front} [m]	D'_{front} [m]	$h_{min,ant}$ [m]
Urban 2	4/2	W/O NR	12.61	12.33	4.42
		W NR	16.48	14.41	9.79
	4/4	W/O NR	13.27	12.98	4.56
		W NR	16.49	14.42	9.79

Table 4.11. Downtilt influence on the definition of physical barriers for the Urban 3 scenario.

Scenario	$N_c \text{ GSM900}/N_c \text{ UMTS}$		D_{Front} [m]	D'_{front} [m]	$h_{min,ant}$ [m]
Urban 3	4/2	W/O NR	11.71	11.45	4.23
		W NR	16.49	14.42	9.79
	4/4	W/O NR	12.38	12.11	4.32
		W NR	16.49	14.42	9.79

Uroof scenarios, presented in Table 2.11, may also generate overexposure if an antenna is installed on top of small buildings at less than 9.79 m above ground. However, this is not expected to happen often since, e.g., considering a small building with 3 floors, 3 m per floor and an antenna installed at 2 m from the roof floor, the total antenna height will be 11 m, which is above the determined minimum value [Corr20]. Also, for this type of installation, the type of cell is usually micro-cell, thus, requiring less power along with a lower downtilt to cover the desired area, decreasing the compliance distances.

Due to the high compliance distances obtained when considering a Uroof scenario, one should also take into account the impact of D_{front} on buildings in front of the BS, since, depending on the street width, their rooftops, top-floor balconies and top-floor indoor spaces may be inside the exclusion zone of that BS.

Assuming a sidewalk with a width of 2.25 m and a traffic lane of 3.5 m, for a street with 2 traffic lanes,

the width of the street is only 11.5 m, which is quite below 16.44 m (D_{front} obtained for the Urban 1 scenario with the 1/1 carrier configuration) [IMTT11]. Therefore, assuming buildings with identical heights, the top floor and the rooftop of the frontal building would be inside the exclusion zone of the BS. However, in order to obtain better coverage, the height of the BS is usually higher than that of the nearby buildings and the antenna may not be installed at the edge of the building, which will increase distance. In addition, the attenuation caused by the glass (12 dB to 34 dB) as well as the walls of the buildings (12 dB to 58 dB) may provide additional safety [HUAW19c].

4.3 Exclusion Zone for Other Directions

In order to obtain an exclusion zone as the one presented in Section 2.5.2, some other directions are analysed for the computation of the back, side, top and bottom borders of the exclusion zone. The angles corresponding to the established directions are presented in Table 4.12.

Table 4.12. Analysed directions for the back, side, top and bottom borders of the exclusion zone.

Back (H plane)	Side (H plane)	Top (V plane)	Bottom (V plane)
180°	90° and 270°	0°	180°

In order to compute the exclusion zone limit distances for those directions, the absolute value of the normalised gain for each direction is subtracted from the maximum antenna gain for each system. The respective normalised gains are presented in Table 4.13. The obtained results for the different directions are presented in Table 4.14.

Table 4.13. Normalised gains for the analysed directions for NR3600.

Normalised Gains [dB]			
Back	Side	Top	Bottom
-40.0	-3.0	-40.0	-40.0

The computed distances for other directions are lower than the distances obtained for the direction of maximum radiation, as expected. However, one should take these results carefully. For instance, the normalised gain used to obtain D_{back} rely on the assumption that the radiating lobe is pointing in the opposite direction to the main radiation direction, which is a conservative approach. In general, the use of the radiation patterns by itself generates conservative results since these patterns are determined in the far-field region.

From the observation of Figure 3.5, one can conclude that, while for the vertical beam scanning, the area corresponding to the maximum beam coverage scope agrees with the area of actual operation of an active antenna (60°), for the horizontal beam scanning the area of actual operation of the antenna is lower (120°), assuming the sectorisation of the BS. Therefore, out of this area, another sector becomes

active instead. This leads to a low significance of the obtained results. Thus, these results must be taken keeping in mind the conservative approaches behind their computation and the actual operating scope of the AA.

Table 4.14. D_{back} , D_{side} , D_{top} and D_{bottom} for Urban, Suburban and Rural scenarios with NR3600 as the only active system.

Scenario	T_{avg} [min]	D_{back} [m]	D_{side} [m]	D_{top} [m]	D_{bottom} [m]
Urban	1	3.97	15.69	3.97	3.97
	6	5.66	16.00	5.66	5.66
	30	8.61	16.28	8.61	8.61
Suburban	1	4.94	15.89	4.94	4.94
	6	6.77	16.13	6.77	6.77
	30	9.73	16.35	9.73	9.73
Rural	1	5.62	16.00	5.62	5.62
	6	7.50	16.20	7.50	7.50
	30	10.42	16.39	10.42	10.42

Due to the low significance of the values obtained for these directions, the analysis of the exclusion zone variation for other directions when all systems are active is left out of the scope of this thesis. The exclusion zone distances for other directions considering only the legacy systems can be seen in [Mour20], since this work takes into account very similar scenarios.

Chapter 5

Conclusions

This chapter ends the thesis, addressing its final conclusions. It summarises all the work developed, addressing some relevant future work.

The deployment density of 5G networks and the consequent reduction in the distance between users and antennas make the current methodology for determining EMF exposure insufficient, since it assumes that the transmitting antennas have predictable radiation patterns and that the BS is transmitting signals at its theoretical maximum power. Such assumptions should not be made when using mMIMO and beamforming. Therefore, there is a need to develop a model to compute EMF exposure in the vicinity of NR BSs antennas, i.e., in the near-field region. Thus, the main goal of this thesis was to develop a model to determine EMF exposure in the vicinity of BSs antennas with 3.6 GHz NR installed in order to compute the respective exclusion zone that would guarantee the general public safety and analyse the influence of AAs on EMF restrictions in 5G BSs deployment. The development of the model took the active behaviour of the 3.6 GHz NR antennas into account by considering realistic maximum power levels, leading to less overestimated results.

This thesis is composed of 5 chapters along with a set of annexes containing some additional information and complementary results. Chapter 1 provides an overview of the work, presenting the evolution and current situation of the mobile communication systems with the arrival of the NR. Concerns about the EMF exposure from NR installation in BSs are discussed along with an introduction to the exclusion zone concept and a brief description of the guidelines to guarantee the general public safety. The motivation and content structure are presented at the end of this chapter.

In Chapter 2, the fundamental concepts of mobile communication systems essential to the correct development of this thesis are presented, such as the radio interface and BS deployments. Types of antenna installations and fundamental concepts of coverage, capacity and interference are discussed. The new 5G active antennas are presented, addressing their main characteristics and the different radiating field regions are discussed, along with the distances between regions. 5G services, namely eMBB, mMTC and URLLC, are also presented and discussed, as are their respective applications. EMF safety guidelines for exposure to different averaging times and frequencies are discussed, along with the definition of exclusion zones and their importance. Finally, the main performance parameters for the model implementation are described, i.e., electric field strength, power density and averaging time, and a state of the art containing the most relevant works related to the topic under study is presented and analysed, addressing the main differences between those works and this thesis.

In Chapter 3, an overview of the general model is presented, containing its main goal, input and output parameters. The temporal variation of EMF exposure is investigated in order to determine its causes and effects on the outcomes. An analysis of the temporal variation of the reference levels set by ICNIRP guidelines is also addressed, in order to obtain the variation of the power density reference level over time. The beamforming behaviour of a planar array antenna is investigated in order to comprehend, along with the temporal variation, the contribution of active antenna behaviour to the increase in EMF exposure.

Still in Chapter 3, the design and simulation of the antenna under study using the CST Studio Suite simulation software is addressed. The software is presented, along with an explanation of its main features and operation. The antenna unit, a half-wavelength dipole, is dimensioned, designed and simulated. A simulation of the full array was then performed, taking into consideration some non-periodic

effects, such as the edge effects and other physical realities. Far-field results are presented in order to assess the correct design and simulation because of its well-known behaviour. Near-field results are then presented, in order to determine the electric field decay with distance along the radiating near- and far-field regions. The limit distance between the reactive near-field and the radiating near-field was determined to be approximately 1.62 m, while the Fraunhofer distance was approximately 16.54 m. The expected decay for the near-field region is confirmed and adjusted for the fit coefficients.

An exclusion zone evaluation model based on the obtained field decay and temporal variation contribution is presented, along with its assessment. One should notice that, due to time constraints, the computation and analysis of the magnetic field decay by simulation was not possible. Thus, it was not possible to assess the exact relationship between the magnetic and electric fields. Because the study focuses more on the transition between the radiating near- and far-field regions, an approximation was made, considering that electric and magnetic fields are directly interrelated by the characteristic impedance (approximation commonly used in the far-field region). A model to assess multi-band exposure, developed in [Mour20], was used and adapted in order to compute exclusion zones considering the exposure from all communication systems.

To assess the exclusion zone evaluation model, a set of empirical tests were performed. By increasing the input power and the gain of the antenna, the electric field strength and the exclusion zone front distance increased. When increasing the power density reference level, a decrease in the exclusion zone front distance happens. All performed tests had the expected results, concluding the assessment of the model.

The decay of the electric field with the distance was exclusively determined based on the simulation of an active antenna with 96 active elements, for the direction of maximum radiation. Hence, the computed decay is based on large antennas with high gains and input powers, leading to an inevitable overestimation of the results, since subarrays and other beam directions are not being taken into account. In the developed model, power, gain and other parameters, such as the ones defining the different scenarios, lie inside a fourth root, which condemns the variations of these parameters to be quite attenuated. Therefore, the developed model is only valid within the previously established distances, not being very sensitive to variations in power and gain.

Since the simulation for other directions, for the antenna under study with 96 active elements, was not possible due to the requirement of higher machine-level capabilities, the radiation patterns of the antennas were used instead, in order to define a somewhat more accurate exclusion zone compared to the one that would be obtained by considering the maximum radiation distance for all directions. However, since radiation patterns are determined based on far-field distances and the maximum beam coverage scope is being considered, an overestimation of the results is inevitable.

Experimental EMF measurements to help evaluate the model by giving the deviation between these values and the ones resulting from the model were conducted in operational BSs. However, a comparison between the theoretical results and the measurements was not possible due to the physical conditions of the rooftops, since they contained a reasonable amount of reflective objects, leading to meaningless and insufficient results, which prevent proper conclusions.

In Chapter 4, an analysis of the results obtained from the model is presented. First, the computation of the exclusion zone considering the NR3600 as the only active system is done. Then, the exclusion zone W/O NR and W NR is determined. Three different appropriate scenarios were considered for each environment (urban, suburban and rural). Contrary to [Mour20], NR3600 was considered to be active not only in urban and suburban environments but also in rural ones, while NR700 was considered to be present in an urban scenario, since this is a real future possibility. Furthermore, LTE800 was considered to be active in an urban scenario, because it will be in charge of Voice over Internet Protocol (VoIP) services. In order to obtain a wide variety of results, four different carrier configurations for GSM and UMTS were analysed: 1/1 ($N_{c\text{ GSM900}}/N_{c\text{ UMTS}}$), 2/1, 4/2, and 4/4. However, one should note that GSM deployments do not usually consider just one carrier.

The first analysis was performed on the variation of D_{front} . The results for the computation of the D_{front} when only NR3600 is active were determined for the Urban_a, Suburban_a and Rural_a scenarios, considering a system usage of 50% and 1 min, 6 min and 30 min as the averaging times. D_{front} ranges from 16.12 m (urban scenario) to 16.48 m (rural scenario), being higher in rural scenarios, as expected. Results for the Urban_b, Suburban_b, and Rural_b scenarios, as well as for other system usages and averaging times, were determined. However, since the compliance distance is proved to be not very sensitive to variations in scenarios and respective parameters, only a representative sample of the results is shown.

An analysis was performed for the variation of D_{front} considering the defined multi-band scenarios. Results taking into account both 100% of the maximum transmit power per beam and the actual percentage of the maximum transmit power per beam of each scenario are presented for each carrier configuration. In order to facilitate a direct comparison with the results from [Mour20], the computation of the exclusion zone was made for an averaging time of 30 min and a system usage of 50%.

Taking 100% of the maximum transmit power per beam, it is possible to conclude that the increase in the compliance distance due to the installation of NR ranges from 92.4% to 314.4% (urban scenarios), from 17.3% to 191.8% (suburban scenarios) and from 16.4% to 234.2% (rural scenarios). However, when the actual percentage of the maximum transmit power per beam of each scenario is considered, the increase in compliance distance due to the installation of NR ranges from 24.3% to 170.4% (urban scenarios), from 16% to 78% (suburban scenarios) and from 16.4% to 104.1% (rural scenarios). The obtained results show a decrease in the compliance distance when considering actual maximum transmit powers. This difference is more noticeable when using an averaging time of 30 min, since it is the averaging time with the lowest power density reference level. In this case, when taking 100% of the maximum transmit power per beam, the compliance distance is no longer within the near-field region but in the far-field one, which explains the increase in the exclusion zone front boarder.

Although the model is somewhat conservative and not very sensitive to changes in scenario parameters, the results obtained for the exclusion zone W NR are quite lower than those obtained in [Mour20], where the increase in the compliance distance due to the installation of NR ranges from 92.3% to 248.7% (urban scenarios), from 17.3% to 131.6% (suburban scenarios) and from 14.3% to 56.4% (rural scenarios). This reduction in the exclusion zone can be explained by the use of the actual maximum

transmitted power, instead of considering the worst-case scenario by using the maximum transmitted power.

One should also notice the fact that the compliance distance, when multi-band exposure with all active systems is taken, is almost the same as the one obtained when considering NR3600 as the only active system. This happens because, at the computed distance, legacy systems do not have such an impact because of their lower gains and input powers in comparison with the ones from NR3600 and the fact that almost every system is within the near-field region, excluding LTE1800, UMTS2100, and LTE2100, which causes the field to decay much faster with distance than it would in the far-field region. Because of the unchanged radio configuration of NR700 and NR3600 throughout the different scenarios, it is expected a lower D_{front} increase when installing NR in BSs with a higher transmitting power from legacy systems, which is confirmed by results. Therefore, the EMF influence of NR decreases as the influence of the legacy systems increases. The increase in D_{front} is overall lower for the scenarios that only consider the deployment of NR700, as opposed to the environments where NR3600 is installed, since NR700 works with passive antennas, having transmitted powers and antenna gains significantly lower than the ones used in NR3600.

Due to the high compliance distances obtained, some considerations should be taken into account regarding public exposure in urban scenarios. For scenarios where antennas are installed close to the ground, physical barriers may need to be installed at street level. For suburban and rural scenarios, the typical BS height for these environments should be enough to ensure the safety of population. The total inclination of the maximum antenna gain was determined for a downtilt of 12° in order to compute the minimum required antenna height, showing that physical barriers at ground level are not required in urban scenarios BSs for antennas with a height greater than 9.79 m. Uroof scenarios may also generate overexposure if an antenna is installed on top of small buildings less than 9.79 m above ground. However, this is not expected to happen often, since, considering a conservative example, the total antenna height would be 11 m, which is above the determined minimum value [Corr20]. Also, for this type of installation, the type of cell is usually micro-cell, thus, requiring less power along with a lower downtilt to cover the desired area, decreasing the compliance distances.

Due to the obtained high compliance distances, one should also take into account the impact of D_{front} on the buildings in front of the BS, since, depending on the street width, their rooftops, top-floor balconies and top-floor indoor spaces may be inside the exclusion zone of that BS. Assuming a common sidewalk, the width of the street would be only 11.5 m, which is quite below the 16.44 m obtained for the Urban 1 scenario with the 1/1 carrier configuration. Therefore, assuming buildings with identical heights, the top floor and rooftop of the frontal building would be inside the exclusion zone of the considered BS. However, in order to obtain a better coverage, the height of the BS is usually higher than that of the nearby buildings, and the antenna may not be installed at the edge of the building, which will increase the distance. In addition, the attenuation caused by the glass (12 dB to 34 dB) as well as the walls of the buildings (12 dB to 58 dB) may provide additional safety.

In order to obtain a complete exclusion zone, other directions were analysed, such as the back, side, top and bottom. The distances for other directions are lower than the ones obtained for the direction of

maximum radiation, as expected. However, one should take these results carefully. For instance, the use of radiation patterns for the computation of the exclusion zone leads to overestimated results, since these patterns are determined in the far-field region. In addition, the normalised gains used to obtain D_{Back} rely on the assumption that the radiating lobe is pointing in the opposite direction to the main radiation direction, which is a conservative approach. Thus, results obtained for these directions can be accepted, keeping in mind the conservative approaches behind the computation of results and the actual operating scope of an active antenna. Considering the vertical and horizontal areas of actual operation of the active antenna (60° and 120° , respectively), the results obtained for these directions have a low significance. Thus, the analysis of the exclusion zone variation for other directions when all systems are active was left out of the scope of this thesis.

The high values obtained for the exclusion zones are quite concerning regarding the general public safety. Although these results should be seen only as an approximation, the installation of antennas should be very well studied. Contrary to what usually happens with installation of antennas with legacy systems (with much lower exclusion zones), a poorly controlled installation of antennas can have consequences for the health of population. In addition, one must take into account the future BS sharing between operators, where the same infrastructure will be shared by several operators, thus increasing EMF exposure.

For future work, it would be interesting to take advantage of the beamforming properties of AAs by simulating several different configurations of subarrays as these configurations would certainly make use of lower antenna input powers and gains, resulting in lower exposure levels and exclusion zone distances. Since these subarrays would lead to lower far-field distances, lower calculation domains would be generated, allowing for the study of the exposure levels for other directions without requiring more advanced computer specifications. The analysis of different antenna configurations would allow one to draw important conclusions in order to develop a more general, accurate and sensitive model. In [Eric21], several subarray configurations are suggested, according to each environment. A study on the influence of BS sharing between operators would also be quite interesting in order to understand its impact on EMF exposure.

Annex A

Antennas Description

Annex A

This annexe presents the main technical characteristics of the different antennas used in this work.

The specifications of the AAUxxxxw Huawei active antenna are presented in Table A.1.

Table A.1. AAUxxxxw technical specifications (based on [HUAW21b]).

Technical Specifications	
Frequency Band [MHz]	3600
Frequency Range [MHz]	3450 to 3700
Polarisation Mode [°]	+45 and –45
NR TDD Gain [dBi]	25
NR TDD Horizontal Beam Sweeping Range [°]	–60 to +60
NR TDD Vertical Beam Sweeping Range [°]	–15 to +15
LTE TDD Traffic Beam Gain [dBi]	25
LTE TDD Broadcast Beam Gain [dBi] ^a	18
Horizontal Half-power Beamwidth of the LTE TDD Broadcast Beam [°]	65±5
Vertical Half-power Beamwidth of the LTE TDD Broadcast Beam [°]	≥5.5
Number of Antenna Elements	192 (96 dual-polarised elements)
TX/RX Mode ^b	64T64R
Array Size	8 × 12
Dimensions of the Antenna (Height × Width × Depth) [mm ³]	730 × 395 × 160
Maximum Output Value [W]	240
a: The gain is obtained in macro coverage scenarios with the horizontal beamwidth of 65°.	
b: ATBR in the TX/RX indicates that the RF module uses A transmit channels and B receive channels.	

In order to perform a comparison between the results in this thesis and the ones in [Mour20], the technical aspects of both antennas, AAUxxxxw and AAUxxx3, are presented side by side in Table A.2.

Table A.2. AAUxxxxw and AAUxxx3 technical comparison (based on [HUAW21b] and [HUAW19b]).

Technical Specifications	Antenna	
	AAUxxxxw	AAUxxx3
Frequency Band [MHz]	3600	
Frequency Range [MHz]	3400-3800	3450-3700
Polarisation Mode [°]	+45 and –45 (Cross-polarisation)	
Gain [dBi]	25	
Horizontal Beam Sweeping Range [°]	–60 to +60	
Vertical Beam Sweeping Range [°]	–15 to +15	
Number of Antenna Elements	192 (96 dual-polarised elements)	
Dimensions (Height × Width × Depth) [mm ³]	730 × 395 × 160	795 × 395 × 220

The main technical characteristics of the ASIxxxxxxx6 passive antenna used in this thesis for the transmission of GSM, UMTS, LTE, and NR700 are presented in Table A.3.

Table A.3. Technical characteristics of the passive antenna (extracted from [HUAW19d]).

Technical Specifications	Frequency Bands [MHz]					
	690-803	790-862	880-960	1695-1990	1920-2200	2490-2690
Polarisation [°]	+45 and -45 (Cross-polarisation)					
Electrical Downtilt [°]	0-10			2-12		
Gain [dBi]	14.9	15.5	16.0	15.5	15.9	16.7
Horizontal HPBW [°]	68±4	63±3	60±3	63±5	62±5	60±6
Vertical HPBW [°]	10.5±0.9	9.5±0.8	8.5±0.7	10.4±0.6	9.4±0.5	7.4±0.3
FTBR (±30°) [dB]	> 22	> 25	> 24	> 25		
Impedance [Ω]	50					
Dimensions (Height × Width × Depth) [mm ³]	1999/429/196					

Annexe B

Measurements Description and BS Characteristics

This annexe presents the layout and characteristics of the different BSs where measurements were performed.

B.1 Measurements Description

B.1.1 General Description

In this subsection, a description of the measurements performed for both BS1 and BS2 is presented.

The measurements were conducted using a scanner by Rohde & Schwarz-TSME6 with the software Genex Probe 5 and a probe antenna, allowing for the determination of the different Received Signal Strength Indication (RSSI) values for each frequency band. The measurements were carried out within the frequency range [3639.99,3699.99] MHz with both traffic and no traffic introduced with an input power, P_{in} , equal to 237 W a maximum gain, G_M , equal to 25 dBi and a maximum number of 162 RBs, which corresponds to a SCS equal to 30 kHz (using the 60 MHz band) [iTec21].

The results were then stored in two separate excel files, one with the frequencies and another with the respective RSSI value files which were later connected through a key and analysed in order to obtain the average RSSI value for each frequency, taking into account the frequencies of interest, i.e., the pilot frequency of each sector of the two BSs under study. The characteristics of the BSs where the measurements were performed are presented in Table B.1.

Table B.1. Characteristics of the BSs where the measurements were conducted.

BS	Sector	Environment	Active Systems	Access Type	Measurement Directions
BS1	2	Urban	NR3600	Restricted Terrace	-45°, 0°, 30°, 60° and 90°
BS2	3				0°, 30°, 60°, 90°

As can be observed, the measurements were conducted in 2 sectors, 1 for each BS. Ideally, the measurement method used in each sector should be such that the sets of measurement points are offset 90° from each other, forming a cross-like pattern in order to allow the analysis of the power behaviour for the front, sides and back of the antennas. Due to constraints in the access and layout of the BSs, the angles were chosen in order to obtain the best possible results given the physical limitations. The measurement points were not equally spaced for that same reasons. The measured values were recorded for 1 minute for each point. Taking into account that the compliance reference levels correspond to exposures with a duration equal or higher than 6 min and according to [OSLA08], a 1-minute measurement window is enough to obtain accurate results, with an associate error lower than 10%.

B.1.2 BS1

BS1 is installed on the rooftop of a building in Lisbon. Taking into account the physical constraints of the rooftop, the measurements in BS1 were taken for sector 2, since it is the sector with the largest area free of objects that could interfere with the measurements. A photograph of the sector as well as a vertical and horizontal plane sketch of sector 2 of the BS are presented in Figures B.1, B.2 and B.3, respectively.



Figure B.1. View to sector 2 of the BS1.

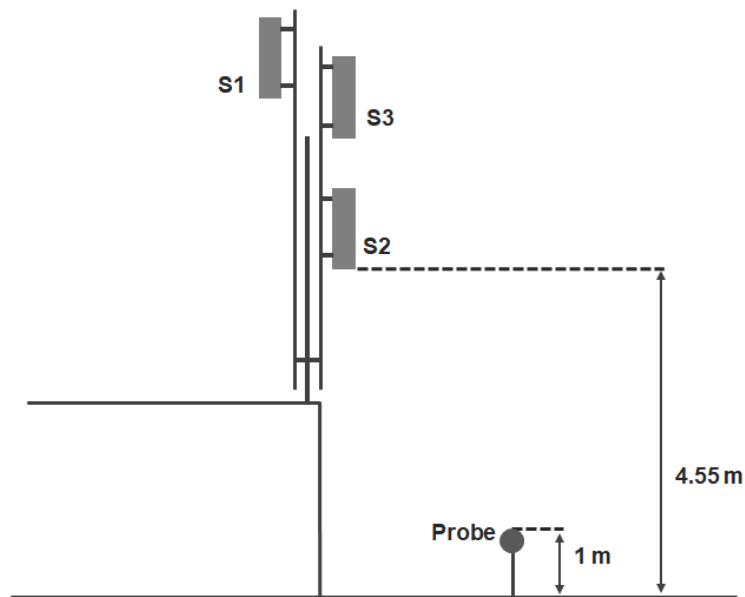


Figure B.2. Vertical plane sketch of sector 2 of the BS1.

Considering the pilot frequency of the sector used for the measurements, 3670 MHz, the measurement results of sector 2 can be seen in Table B.2 and its graphic representation is presented in Figure B.4. One should note that “nt” means “no traffic”, i.e., the measurements were taken with no traffic introduced and that f_{P1} , f_{P2} , f_{P3} are the frequency pilots of the different sectors.

By analysing Figure B.4, it is possible to conclude that most of the measurements do not follow the expected behaviour (power decreasing with the distance) and that the ones that do follow the expected behaviour are not enough to draw conclusions, since in order to define a curve it is required to have at

least 3 points. As stated before, these measures can be explained by the several reflective objects present on the terrace. In Figures B.5, B.6 and B.7, one can observe the terrace environment.

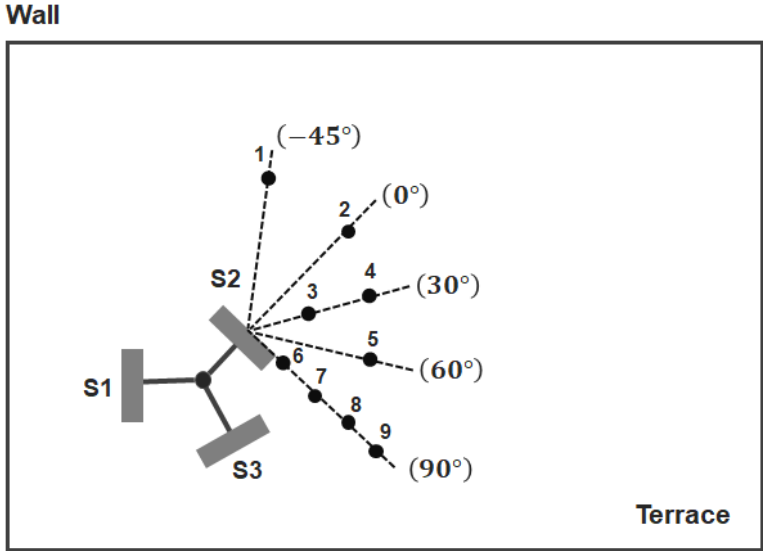


Figure B.3. Horizontal plane sketch of sector 2 of the BS1.

Table B.2. Measurement results for sector 2 of the BS1.

Observation Point	Azimuth angle [°]	Distance [m]	$RSSI_{measure,avg}$ [dBm]
1_nt	-45	13.10	-84.24
2_nt	0	10.80	-87.58
3_nt	30	3.5	-84.84
4_nt		7.10	-90.17
5_nt	60	7.10	-81.55
6_nt	90	3	-91.29
7_nt		5	-87.86
8_nt		7	-87.62
9_nt		9	-84.06

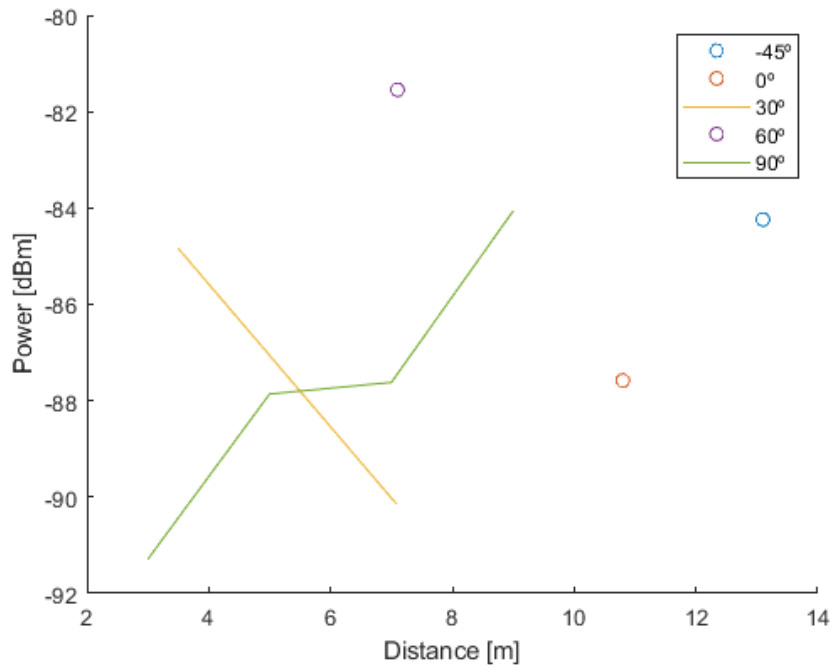


Figure B.4. Measurement results for sector 2 of the BS1.



Figure B.5. View of the terrace where BS1 is installed.

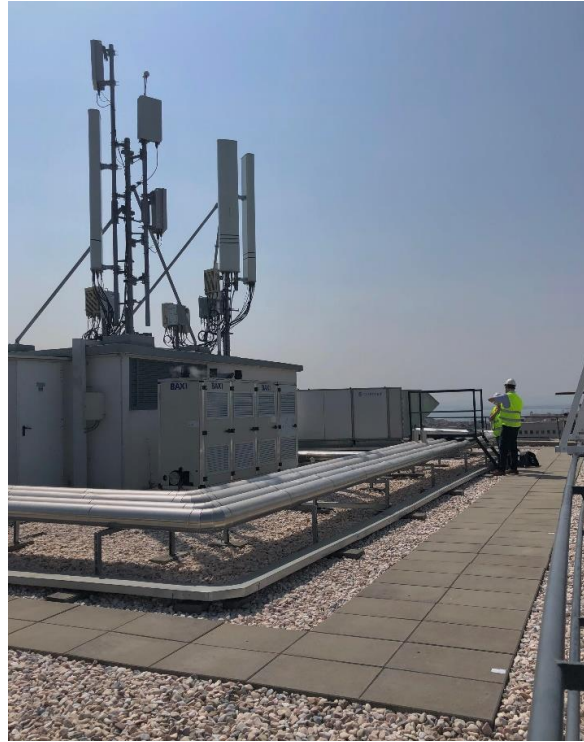


Figure B.6. View of the terrace where BS1 is installed.

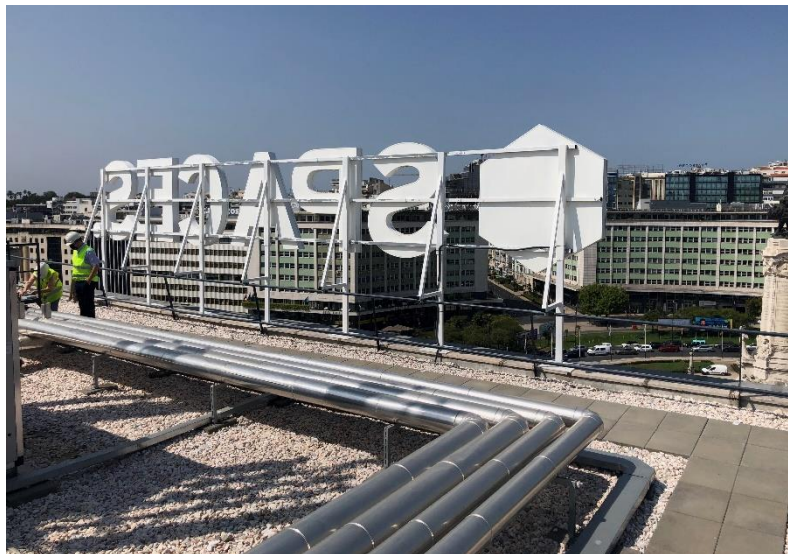


Figure B.7. View of the terrace where BS1 is installed.

B.1.3 BS2

BS2 is installed on the rooftop of another building in Lisbon. Taking into account the physical constraints of the rooftop, the measurements in BS2 were taken for sector 3, since it is the sector with the largest area free of objects that could interfere with the measurements. A photograph of the sector as well as a vertical and horizontal plane sketch of sector 3 of the BS2 are presented in Figures B.8, B.9 and B.10, respectively. Table B.2 contains the measurement results of sector 2 of the BS2.



Figure B.8. View of sector 3 of the BS2.

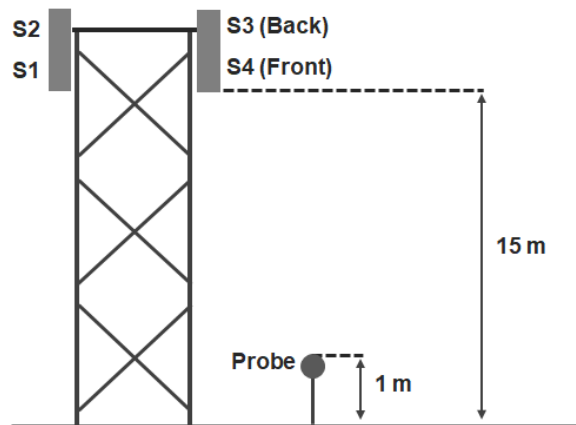


Figure B.9. Vertical plane sketch of sector 3 of the BS2.

Considering the pilot frequency of the sector used for the measurements, 3670 MHz, the measurement results of sector 3 of the BS2 with no traffic introduced and also with traffic introduced, can be seen in Table B.3 and its graphic representation is presented in Figure B.8 and Figure B.9, respectively. One should note that “wt” means “with traffic”, i.e., the measurements were taken with traffic introduced (large file downloaded).

In Figure B.11 and B.12, the same conclusions as the ones described for Figure B.4 can be extracted and justified by the presence of several reflective objects as well, as can be seen in Figure B.13.

Wall

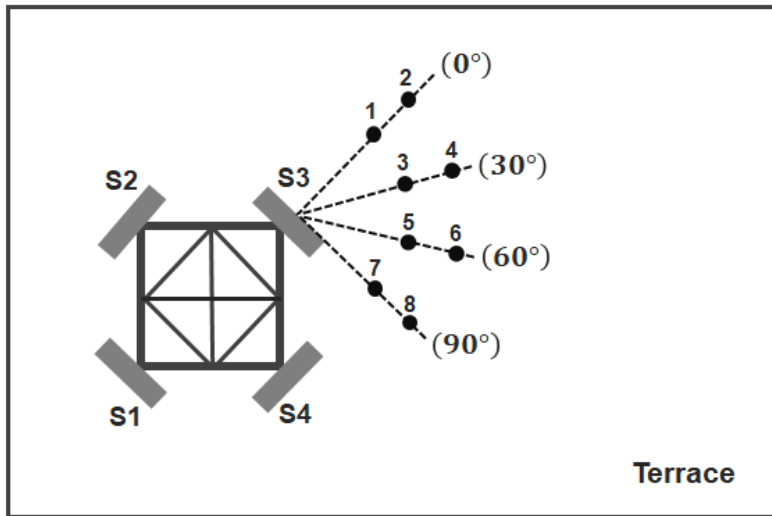


Figure B.10. Horizontal plane sketch of sector 3 of the BS2.

Table B.3. Measurement results for sector 3 of the BS2.

Observation Point	Azimuth angle [°]	Distance [m]	$RSSI_{measure,avg}$ [dBm]
1_nt	0	5	-83.79
2_nt		7	-92.82
3_nt	30	5	-97.22
4_nt		7	-99.08
5_nt	60	5	-84.50
6_nt		7	-94.38
7_nt	90	5	-94.49
8_nt		7	-86.27
1_wt	0	5	-48.95
2_wt		7	-44.14
3_wt	30	5	-46.15
4_wt		7	-42.42
5_wt	60	5	-45.19
6_wt		7	-42.55
7_wt	90	5	-49.79
8_wt		7	-42.20

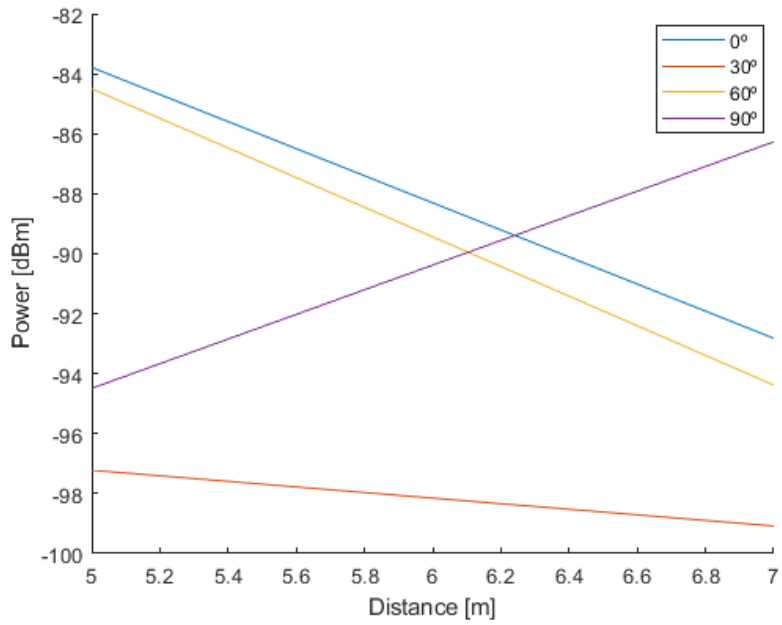


Figure B.11. Measurement results of sector 3 of the BS2 with no traffic induced.

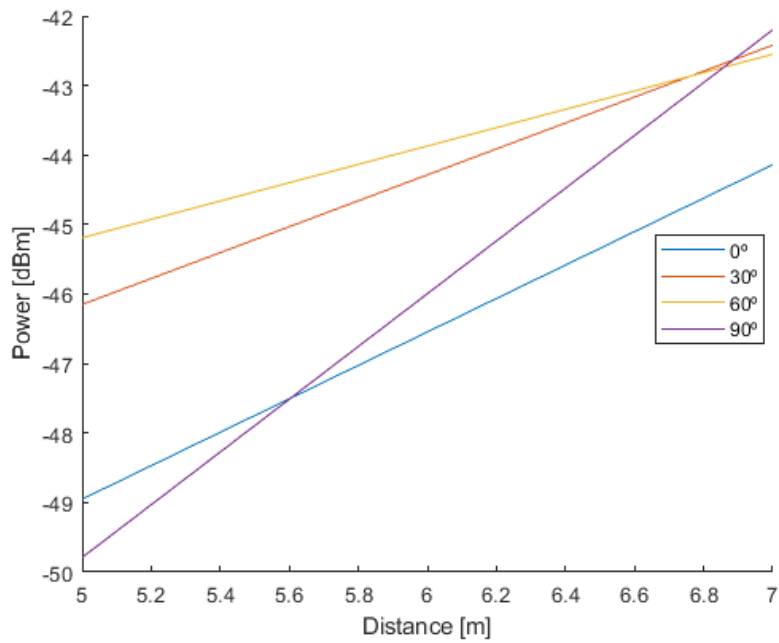


Figure B.12. Measurement results of sector 3 of the BS2 with traffic induced.



Figure B.13. View of the terrace where BS2 is installed.

Annexe C

Multi-band Exposure Computation

This annexe presents the equations and parameters considered for the computation of the multi-band exposure.

In this section, the model developed in [Mour20], used to determine the exposure of the power density in the near and far-field regions for communications systems using passive antennas, is presented, along with the parameters for the computation of the exclusion zone, taking into account the multi-band exposure. Therefore, the power density for the passive antennas is given by [Mour20]:

$$S_{pass_ant}(d, \theta, \phi)_{[W/m^2]} = \frac{P_{in} G_M f_{\theta\phi}(\theta, \phi)}{4\pi} \times \begin{cases} S_{nf}^{norm}(d), & R_{rnf} \leq d < R_{ff} \\ \frac{1}{d^2}, & d > R_{ff} \end{cases} \quad (C.1)$$

where:

- $S_{nf}^{norm}(d)$: power density function for the near-field of the passive antennas, normalised to the input power and antenna gain.

$S_{nf}^{norm}(d)$, in turn, is given by:

$$S_{nf}^{norm}(d) = \begin{cases} \frac{1}{(a_0 + a_1 d + a_2 d^2)}, & N_{el}, N_{V,el} < 8 \\ \frac{1}{(a_0 + a_1 d + a_2 d^2 + a_3 d^3)}, & N_{el}, N_{V,el} \geq 8 \end{cases} \quad (C.2)$$

where:

- a_0, a_1, a_2, a_3 : fit coefficients for the passive antennas.

The reactive near-field region boundary for this model is considered to be equal to 3λ [Mour20].

As one can conclude from observing the normalised power density function for the near-field, there is a distinction between the decay of the power density of an antenna with less than 8 elements and an antenna with 8 or more elements. In order to take a conservative approach, antennas with 8 elements spaced by an element spacing factor, Δ_{ele} , equal to 1 are simulated.

For the computation of the multi-band exposure, a sampling interval must be established, being given by:

$$\Delta_d = \frac{d_{max} - d_{min}}{N_{samp}} \quad (C.3)$$

where:

- d_{max} : maximum limit for the definition of the sampling interval;
- d_{min} : minimum limit for the definition of the sampling interval.

d_{min} should be equal to the highest of the two R_{rnf} values from the two models and d_{max} should be greater than the maximum far-field distance, $d_{max} = \max\left\{\frac{2D_i^2}{\lambda_i} : i = 1, \dots, N_{sys}\right\} + 20$. In order to guarantee an acceptable accuracy of the model, a number of samples equal to 100 000 is chosen.

Taking into account that, in the current thesis, the exclusion zone distance considering multi-band exposure is determined only for the direction of maximum radiation, the normalised three-dimensional antenna radiation pattern, $f_{\theta\phi}(\theta, \phi)$, for the passive antennas is considered to be equal to 1. Therefore, the main input parameters of the MATLAB program are the frequency, P_{in} , G_M , Δ_{es} , N_{el} , antenna dimensions, N_{samp} , d_{max} and d_{min} .

The normalised coefficients and far-field distances for the passive antennas with 8 active elements are presented in Table C.1.

Table C.1. S_{nf}^{norm} coefficients and far-field distances for the different systems, considering the passive antennas with 8 elements (extracted from [Mour20]).

System	$S_{nf}^{norm}(d)$ Coefficients				R_{ff} [m]
	a_0 [m ²]	a_1 [m]	a_2	a_3 [m ⁻¹]	
NR700	1.2753	16.9713	-0.6188	0.0418	20.35
LTE800	0.8111	16.0732	-0.6551	0.0460	21.76
GSM/UMTS900	2.0898	12.2407	-0.3458	0.0384	25.15
LTE1800	0.4650	6.4919	-0.4062	0.0780	12.23
UMTS/LTE2100	0.5797	4.8327	-0.1404	0.0666	14.25
LTE2600	0.3720	3.7171	-0.1297	0.0850	17.73

References

- [ANAC20] ANACOM, <https://www.anacom.pt/render.jsp?categoryId=382989>, Oct. 2020.
- [Antu12] M.G.C. Antunes, *Estimation of exclusion regions in LTE base stations collocated with GSM/UMTS*, M.Sc. Thesis, Instituto Superior Técnico, University of Lisbon, Lisbon, Portugal, Oct. 2012.
- [Bala16] C.A. Balanis, *Antenna Theory: Analysis and Design*, Fourth Edition, John Wiley & Sons, New Jersey, USA, 2016.
- [BELC18] I.A.R. Belchior, *Evaluation of 5G cellular network implementation over an existing LTE one*, M.Sc. Thesis, Instituto Superior Técnico, University of Lisbon, Lisbon, Portugal, Nov. 2018.
- [BWWG18] P. Baracca, A. Weber, T. Wild and C. Grangeat, "A statistical approach for RF exposure compliance boundary assessment in massive MIMO systems", in *Proc. 22nd Int. ITG Workshop Smart Antennas*, Bochum, Germany, Mar. 2018.
- [CCMF18] L. Chiaraviglio, A.S. Cacciapuoti, G. Martino, M. Fiore, M. Montesano, D. Trucchi and N.B. Melazzi, "Planning 5G Networks Under EMF Constraints: State of the Art and Vision", *IEEE Access*, Vol. 6, Sep. 2018, pp. 51021-51037.
- [CJPT19] D. Colombi, P. Joshi, R. Pereira, D. Thomas, D. Shleifman, B. Tootoonchi, B. Xu and C. Törnevik, "Assessment of Actual Maximum RF EMF Exposure from Radio Base Stations with Massive MIMO Antennas", in *2019 Photonics & Electromagnetics Research Symposium*, Rome, Italy, June 2019.
- [CJXG20] D. Colombi, P. Joshi, B. Xu, F. Ghasemifard, V. Narasaraju and C. Törnevik, "Analysis of the Actual Power and EMF Exposure from Base Stations in a Commercial 5G Network", *Applied sciences*, Vol. 10, No.15, July 2020, pp. 5280.
- [COMM21] COMMESCOPE, <https://www.commscope.com/globalassets/digizuite/542044-Beamformer-Explained-WP-114491-EN.pdf>, Mar. 2021.
- [Corr20] L.M. Correia, *Mobile Communication Systems*, Lecture Notes, Instituto Superior Técnico, University of Lisbon, Lisbon, Portugal, Feb. 2020.
- [CoTT15] D. Colombi, B. Thors and C. Törnevik, "Implications of EMF Exposure Limits on Output Power Levels for 5G Devices Above 6 GHz", *IEEE Antennas and Wireless Propagation*

Letters, Vol. 14, Feb. 2015, pp. 1247-1249.

- [Dass10] Dassault Systèmes, *Understanding Time Domain Meshing in CST Microwave Studio*, Manual guide, Deutschland, 2010 (<https://www.researchgate.net/file.PostFileLoader.html?id=578c450ceeeae3937441b63a1&assetKey=AS%3A385033333428224%401468810508239>).
- [Dass19] Dassault Systèmes, *CST Studio Suite High Frequency Simulation*, Manual guide, Deutschland, 2019 ([file:///C:/Program%20Files%20\(x86\)/CST%20Studio%20Suite%202020/Online%20Help/cst_studio_suite_help.htm#general/welcome_de.htm](file:///C:/Program%20Files%20(x86)/CST%20Studio%20Suite%202020/Online%20Help/cst_studio_suite_help.htm#general/welcome_de.htm)).
- [Dass21a] Dassault Systèmes, 2021 (<https://www.3ds.com/products-services/simulia/products/cst-studio-suite/>).
- [Dass21b] Dassault Systèmes, *CST Studio Suite 2020 Help*, 2021 ([file:///C:/Program%20Files%20\(x86\)/CST%20Studio%20Suite%202020/Online%20Help/cst_studio_suite_help.htm#general/welcome_de.htm](file:///C:/Program%20Files%20(x86)/CST%20Studio%20Suite%202020/Online%20Help/cst_studio_suite_help.htm#general/welcome_de.htm)).
- [ELIF16] eLIFE, *A Century of Trends in Adult Human Height*, Research Article, McGill University, Canada, 2016 (<https://elifesciences.org/articles/13410#metrics>).
- [Eric21] Ericson, <https://www.ericsson.com/en/reports-and-papers/white-papers/advanced-antenna-systems-for-5g-networks>, Oct. 2021.
- [Euro20a] Euronews, <https://www.euronews.com/2020/05/15/what-is-the-truth-behind-the-5g-coronavirus-conspiracy-theory-culture-clash>, Oct. 2020.
- [Euro20b] European Commission, https://ec.europa.eu/info/live-work-travel-eu/coronavirus-response/fighting-disinformation_en, Oct. 2020.
- [Even21] EventHelix, https://www.eventhelix.com/RealtimeMantra/CongestionControl/m_m_1_queue.htm, Feb. 2021.
- [Goog21] Google Maps, <https://www.google.pt/maps/>, July 2021.
- [HUAW19a] Huawei, *New 5G, New Antenna*, White Paper, Huawei Technologies, Shenzhen, China, 2019 (<https://carrier.huawei.com/~/-/media/CNBGV2/download/products/antenna/New-5G-New-Antenna-5G-Antenna-White-Paper-v2.pdf>).
- [HUAW19b] Huawei, *AAUxxx3 Technical Specifications*, Antenna datasheet, Shenzhen, China, Mar. 2019.
- [HUAW19c] Huawei, *Huawei 5G Wireless Network Planning Solution*, White Paper, Shenzhen, China, 2019 (https://www-file.huawei.com/-/media/corporate/pdf/white%20paper/2018/5g_wireless_network_planing_solution_en_v2.pdf?la=en).

- [HUAW19d] Huawei, *ASLxxxxxxx6 Technical Specifications*, Antenna datasheet, Shenzhen, China, Dec. 2019.
- [HUAW21a] Huawei, <https://www.huawei.com/en/>, September 2021.
- [HUAW21b] Huawei, *AAUxxxxw Technical Specifications*, Antenna datasheet, Shenzhen, China, Mar. 2021.
- [ICNI20] ICNIRP, “Guidelines for Limiting Exposure to Electromagnetic Fields (100 kHz to 300 GHz)”, *Health Physics*, Vol. 118, No. 5, Mar. 2020, pp. 483-524.
- [iTec21] iTecTec, <https://itectec.com/spec/5g-nr-bs-channel-bandwidth/>, Aug. 2021.
- [ITUR17] ITU Radiocommunication Sector, *Guidelines for evaluation of radio interface technologies for IMT-2020*, ITU-Recommendation M.2412, Geneva, Switzerland, 2017 (https://www.itu.int/dms_pub/itu-r/opb/rep/R-REP-M.2412-2017-PDF-E.pdf).
- [IMTT11] IMTT, *Road Network - Planning and Design Principles* (in Portuguese), Instituto da Mobilidade e dos Transportes Terrestres, Mar. 2011 (<http://www.imt-ip.pt/sites/IMTT/Portugues/Planeamento/DocumentosdeReferencia/PacotedaMobilidade/Paginas/QuadrodeReferenciaparaPlanosdeMobilidadeAcessibilidadeeTransportes.aspx>).
- [InTU20a] International Telecommunication Union, *Expert Meeting on Electromagnetic Field Level and 5G Roll-out*, <https://www.itu.int/en/ITU-D/RegionalPresence/Europe/Pages/Events/2017/EMF/Electromagnetic-Field-Level-and-5G-Roll-out-.aspx>, Nov. 2020
- [InTU20b] International Telecommunication Union, *Workshop on 5G, EMF & Health*, <https://www.itu.int/en/ITU-T/Workshops-and-Seminars/20171205/Pages/default.aspx>, Nov. 2020
- [InTU19] International Telecommunication Union, *5G technology and human exposure to radio-frequency electromagnetic fields*, Recommendations document, Telecommunication standardisation sector of ITU, Geneva, Switzerland, 2019 (<https://www.itu.int/en/Pages/default.aspx>).
- [Jevr20] V. Jevremovic, *EMF Radiation in Mobile Networks: A Closer Look at Emission Limits & Safe Distances*, PhD White Paper, iBwave, 2020, (<https://www.ibwave.com/storage/app/media/pdf/white-papers/EMF-radiation-in-mobile-wireless-networks-pt1.pdf>).
- [JTCT16] P. Joshi, B. Thors, D. Colombi, C. Törnevik, and L.E. Larsson, “Realistic output power levels of multi-technology radio base stations and the implication on RF EMF exposure compliance assessment” in *Joint Annual Meeting of the Bioelectromagnetics Society and the European BioElectromagnetics Association*, Ghent, Belgium, June 2016.

- [Laak15] I. Laakso, *Introduction to the FDTD method*, Department of Electrical Engineering and Automation, Power Point Presentation, 2015 (https://mycourses.aalto.fi/pluginfile.php/153433/mod_resource/content/3/Introduction%20to%20FDTD.pdf).
- [LRCE16] S. Liu, R. Raad, K. Chin and F. EM. Tubbal, "Dipole antenna array cluster for CubeSats," in *Proc. of 10th International Conference on Signal Processing and Communication Systems*, Gold Coast, Australia, Dec. 2016.
- [KDRS15] K.A. Kapalo, A.R. Dewar, M.A. Rupp and J.L. Szalma, "Individual Differences in Video Gaming: Defining Hardcore Video Gamers", in *Proc. of the Human Factors and Ergonomics Society 59th Annual Meeting*, Los Angeles, California, USA, Oct. 2015.
- [Camp17] J. Campos, *Understanding the 5G NR Physical Layer*, Presentation, Keysight Technologies, 2017 (https://www.keysight.com/upload/cmc_upload/All/Understanding_the_5G_NR_Physical_Layer.pdf).
- [Mand19] A. Mandhyan, *4G and 5G Capacity solutions*, Comparative study, CommScope, 2019 (<https://www.commscope.com/globalassets/digizuite/2154-capacity-solutions-comparative-study-wp-113400-en.pdf?r=1>).
- [Mour20] F.C.R.M Moura, *Analysis of the Impact of EMF Restrictions on 5G Base Stations Deployment in Existing Networks*, M.Sc. Thesis, Instituto Superior Técnico, University of Lisbon, Lisbon, Portugal, 2020.
- [Nasi19] I. Nasim, *Analysis of Human EMF Exposure in 5G Cellular Systems*, M.Sc. Thesis, Georgia Southern University, Statesboro, GA, USA, 2019.
- [OFRC05] C. Oliveira, C.C. Fernandes, C. Reis, G. Carpinteiro, L. Ferreira, L.M. Correia and D. Sebastião, *Definition of Exclusion Zones around typical Installations of Base Station Antennas*, monIT Project report, Telecommunications Institute, Lisbon, Portugal, Feb. 2005.
- [PaKŻ19] R. Pawlak, P. Krawiec, J. Żurek, "On Measuring Electromagnetic Fields in 5G Technology", *IEEE Access*, Vol. 7, Mar. 2019, pp. 29826-29835.
- [REMC19] REMCOM, *Beamforming for an 8x8 Planar Phased Patch Antenna Array for 5G at 28 GHz*, State College, USA, 2019 (<https://www.everythingrf.com/whitepapers/details/3264-beamforming-for-an-8x8-planar-phased-patch-antenna-array-for-5g-at-28-ghz>).
- [Ribe18] A.G. Ribeiro, *Analysis of Antennas' Locations on Trains for Mobile Communications*, M.Sc. Thesis, Instituto Superior Técnico, University of Lisbon, Lisbon, Portugal, Oct. 2018.

- [Silv20] M.G. Silveirinha, *Antennas*, Lecture Notes, Instituto Superior Técnico, Lisbon, Portugal, 2020.
- [Simi21] Similarweb, <https://www.similarweb.com/corp/blog/research/market-research/session-duration/>, July 2021.
- [Skol90] M.I. Skolnik, *Radar Handbook*, McGraw-Hill, New York, New York, USA, 1990.
- [Skyp21] Skype, <https://www.skype.com/pt/>, July 2021.
- [Stat21] Statista, <https://www.statista.com/statistics/910910/us-most-popular-us-video-streaming-services-session-duration/>, July 2021.
- [TCYB16] B. Thors, D. Colombi, Z. Ying, T. Bolin and C. Törnevik, "Exposure to RF EMF From Array Antennas in 5G Mobile Communication Equipment", *IEEE Access*, Vol. 4, Aug. 2016, pp. 7469-7478.
- [TFCT17] B. Thors, A. Furuskär, D. Colombi and C. Törnevik, "Time-averaged realistic maximum power levels for the assessment of radio frequency exposure for 5G radio base stations using massive MIMO", *IEEE Access*, Vol. 5, Sep. 2017, pp. 19711-19719.
- [Thal20] Thales, <https://www.thalesgroup.com/en/markets/digital-identity-and-security/mobile/inspired/5G>, Oct. 2020.
- [TWGH20] C. Törnevik, T. Wigren, S. Guo and K. Huisman, "Time Averaged Power Control of a 4G or a 5G Radio Base Station for RF EMF Compliance", *IEEE Access*, Vol. 8, Nov. 2020, pp. 211937-211950.
- [XZTC17] B. Xu, K. Zhao, B. Thors, D. Colombi, O. Lundberg, Z. Ying and S. He, "Power density measurements at 15 GHz for RF EMF compliance assessments of 5G user equipment", *IEEE Trans. Antennas Propag.*, Vol. 65, No. 12, Dec. 2017, pp. 6584-6595.
- [XZYS19] B. Xu, K. Zhao, Z. Ying, D. Sjöberg and S. He, "Analysis of Impacts of Expected RF EMF Exposure Restrictions on Peak EIRP of 5G User Equipment at 28 GHz and 39 GHz Bands", *IEEE Access*, Vol.7, Feb. 2019, pp. 20996-21005.
- [WINN07] P. Kyösti, J. Meinilä, L. Hentila, X. Zhao, T. Jämsä, C. Schneider, M. Narandzic, M. Milojević, A. Hong, J. Ylitalo, V. Holappa, M. Alatossava, R. Bultitude, Y. Jong and T. Rautiainen, "WINNER II Channel Models - Part I Channel Models", *Research Gate*, V1.2, Feb. 2008.
- [Worl20] World Health Organisation, https://www.who.int/peh-emf/project/EMF_Project/en/, Nov. 2020.
- [XGSZ18] B. Xu, M. Gustafsson, S. Shi, K. Zhao, Z. Ying and S. He, "Radio frequency exposure

- compliance of multiple antennas for cellular equipment based on semidefinite relaxation”, *IEEE Trans. Electromagnet. Compat.*, Vol. 61, June 2018, pp. 327-336.
- [ZGLZ17] K. Zhao, C. Gustafson, Q. Liao, S. Zhang, T. Bolin, Z. Ying and S. He, “Channel characteristics and user body effects in an outdoor urban scenario at 15 and 28 GHz”, *IEEE Trans. Antennas Propag.*, Vol. 65, No. 12, Dec. 2017, pp. 6534-6548.
- [XGSY18] B. Xu, M. Gustafsson, S. Shi, Z. Yingz and S. He, “Upper Bound Study of 5G RF EMF Exposure”, in *2018 IEEE International Symposium on Antennas and Propagation & USNC/URSI National Radio Science Meeting*, Boston, MA, USA, July 2018.
- [ZhTC15] X. Zhao, J. Tak, J. Choi, “Worst-Case Estimate of Envelope Correlation Coefficient for Small MIMO Mobile Antennas Below 1 GHz”, *Journal of Electromagnetic Engineering and Science*, Vol. 15, No. 1, Jan. 2015, pp. 44–52.
- [Zoom21] Zoom, <https://zoom.us/pt-pt/meetings.html>, July 2021.